# Geochemical characteristics of volcanogenic massive sulfide mineralizations on Bømlo and Stord islands, Sunnhordaland, SW Norway

Master of science thesis

Trond Fjellet


Department of Earth Science
University of Bergen
August 2021

# Abstract

The results from the present study have brought forward new knowledge about geochemical, mineralogical, stable isotope and trace element data for volcanogenic massive sulfide deposits hosted within Early Ordovician Ophiolitic terrane of south western Norway. The geology of the Sunnhordaland region is comprised of rocks native to the Baltic continent and exotic rocks that formed adjacent to the Laurentian margin in the Iapetus Ocean hosting numerous deposits in the Hardanger Cu-Zn-Au Province. Though numerous, the geochemical characteristics of volcanogenic massive sulfide deposits in the region are poorly constrained. The investigated deposits are located on the islands of Bømlo and Stord and are associated with ophiolitic, island-arc and volcano-sedimentary successions.

Hosted within the Lykling Ophiolite Complex the epigenetic Cu-rich Alvsvågen mineralization is spatially associated with four SW-NW trending shear zones that intersect the high-level gabbroic portion of the ophiolite complex. The Cu-rich mineral assemblage, hydrothermal alteration characteristics and the magmatic origin of sulfur suggest that the Alvsvågen mineralization was deposited within deep fluid conduits of a volcanogenic massive sulfide system.

The Lindøya and Litlabø deposits feature mineral assemblages predominantly composed of Fe-sulfides with minor amounts of base metal sulfides. Both deposits are interpreted as results of exhalative venting, although vastly different depositional mechanisms have been recognized. The basalt hosted Lindøya deposit is composed of a massive layered sulfide ore body associated with sulfides hosted as veinlets and disseminations in basalt. Textural characteristics, close spatial association with the basalt and the sulfur isotopic signature indicating thermochemical reduction of seawater sulfate, suggest a proximal deposition from hydrothermal fluids. In contrast, the Litlabø mineralization is hosted by a volcano-sedimentary sequence predominantly composed of organic-rich shale, jasper and siliciclastic sediments. The mineralization is characterized by an enrichment in a suit of redox sensitive elements, including V, Mn, Mo and U, and by a strong depletion in $^{34}S$ indicating bacterial reduction of seawater sulfate. Textural, mineralogical and stable isotope features suggest that the Litlabø mineralization was deposited under anoxic/euxinic conditions in a restricted ocean basin.

# Acknowledgements

Firstly, I would like to thank my supervisors Sabina Strmić Palinkaš and Rolf Birger Pedersen for giving me the opportunity to work with this interesting project. Especially, I would like to thank Sabina for all the help with the fieldwork, advice on the lab work and constructive comments during the writing process which greatly improved the quality of this thesis. Without you this thesis would not be possible. I would also like to than my co-supervisor Håvard H. Stubseid for helping out with all the practicalities during lab and fieldwork.

A lot of lab work was included in this thesis and I would like to thank everyone that contributed in this regard. I would like to thank Ida Marie Gabrielsen for helping with the sample preparation for trace and major element analyses. Also, I would like to than Andreas Viken for preparing the numerous thin and thick-sections. Many hours were spent at the electron microscopy laboratory, and I am grateful to Leif E. Ryland and Irene Heggstad for all the assistance during this work.

In addition to those already mentioned, I would like to especially thank Frida, Matz and Simen for being inexplicable field companions during the field work. I am also grateful towards Ingvild Aarrestad that provided invaluable feedback on the writing of this thesis. I would also like to thank Øystein and the rest of the people at the "Black Smoker" for all the fond memories over the last two years. To the rest of the guys, all our trips to Hectors will not be forgotten. Finally, I would like to thank my family for the invaluable support during the writing of this thesis.

This study has been founded by the EIT Raw Materials project "MinExTarget" (Grant agreement number 19217)

Bergen 26.08.2021
Trond Fjellet

# Table of contents

# 1 Introduction

The Sunnhordaland area in south western Norway has been a site of several minor and larger mining operations (Figure 1). It hosts over 100 mineral deposits with various commodities, including base and precious metals (Wulff, 1996). The deposits in the area are hosted by the Lower Ordovician ophiolitic terrane, which are composed of several ophiolite complexes, island-arc complexes and metasedimentary sequences. All these lithologies belong to the Upper Allochthon of the Scandinavian Caledonides (Figure 1), a tectonostratigraphic unit whose metallogeny is marked by presence of numerous economically important volcanogenic massive sulfide (VMS) deposits (Figure 2; Grenne et al. 1999; Raaness et al. 2020).

Despite numerous VMS deposits in the Sunnhordaland region, geochemical characteristics of the mineralization have been poorly constrained for this area (Grenne et al., 1999). The first investigations into deposits in the Sunnhordaland region date back to late 19$^{th}$ and early 20$^{th}$ century (Helland, 1871; Reusch, 1888; Foslie, 1926), but no proper large-scale studies had been performed before an extensive investigation by Wulff (1993; 1996) brought forward new knowledge about the Cu-Zn-Au deposits in the Hardangerfjord region. From this investigation several distinct deposit hosting areas was separated. On the island of Bømlo, deposits are hosted in the Lykling Ophiolite Complex and the immature island-arc Geitung Unit (Wulff, 1993), while on Stord the deposits are hosted within the volcano-sedimentary Langevåg Group.

This study aims to bring forward new knowledge about VMS mineralizations on the islands of Bømlo and Stord in the Sunnhordaland region by studying mineral, geochemical and stable isotope characteristics of three selected deposits that were deposited under different ore-forming conditions.

## Purpose of the study

The main purpose of this study is to bring forward new geochemical, mineralogical, stable isotope and trace element data for three different types of the VMS mineralization in the Sunnhordaland region. The focus was given to the mineralizations hosted by the Lykling Ophiolite Complex and the volcano-sedimentary Langevåg Group (Figure 3, 4). The selected study localities include the Alvsvågen, Lindøya and Litlabø deposits on the Bømlo and Stord islands (Figure 5). The study combines microscopic investigations, scanning electron microscopy coupled with an energy dispersive system (SEM-EDS), trace and minor element characterization of main sulfide phases and sulfur isotopic studies. The study also brings new major and trace element data for the host lithologies with an aim to identify the geodynamic setting of the Sunnhordaland VMS deposits.

# 2 Regional geology

## 2.1 Tectonic setting

The evolution of the Caledonian orogen started with the formation of the Iapetus Ocean between the two continents of Laurentia and Baltica at the Vendian-Cambrian transition (Roberts, 2003). The onset of extension and formation is marked by a marine transgression and carbonatite-alkaline intrusions which intruded 590-565 Ma on both continents (Roberts et al., 1985). Oblique collision of the two major continents during the Caledonian orogeny led to subduction of Baltica beneath Laurentia, resulting in allochthonous tectonic units being accreted onto the Baltic continent (Roberts, 2003). As a result, Fossen (1992) divided the southern part of the Norwegian Caledonides into three main stratigraphic tectonic units: a Precambrian basement (the Baltic Shield), a décollement zone and an orogenic wedge of nappes. The allochthonous thrust sheets are separated into Lower, Middle, Upper and Uppermost Allochthons with the latter two containing elements exotic to the Baltic margin (Roberts, 2003) (Figure 1). The Sunnhordaland region in south western Norway is comprised mainly of Precambrian basement rocks and overriding allochthonous units separated by the Hardangerfjord Shear Zone. Volcanogenic Massive sulfide (VMS) deposits are almost exclusively hosted within the Upper Allochthons in the Sunnhordaland region (Figure 2).

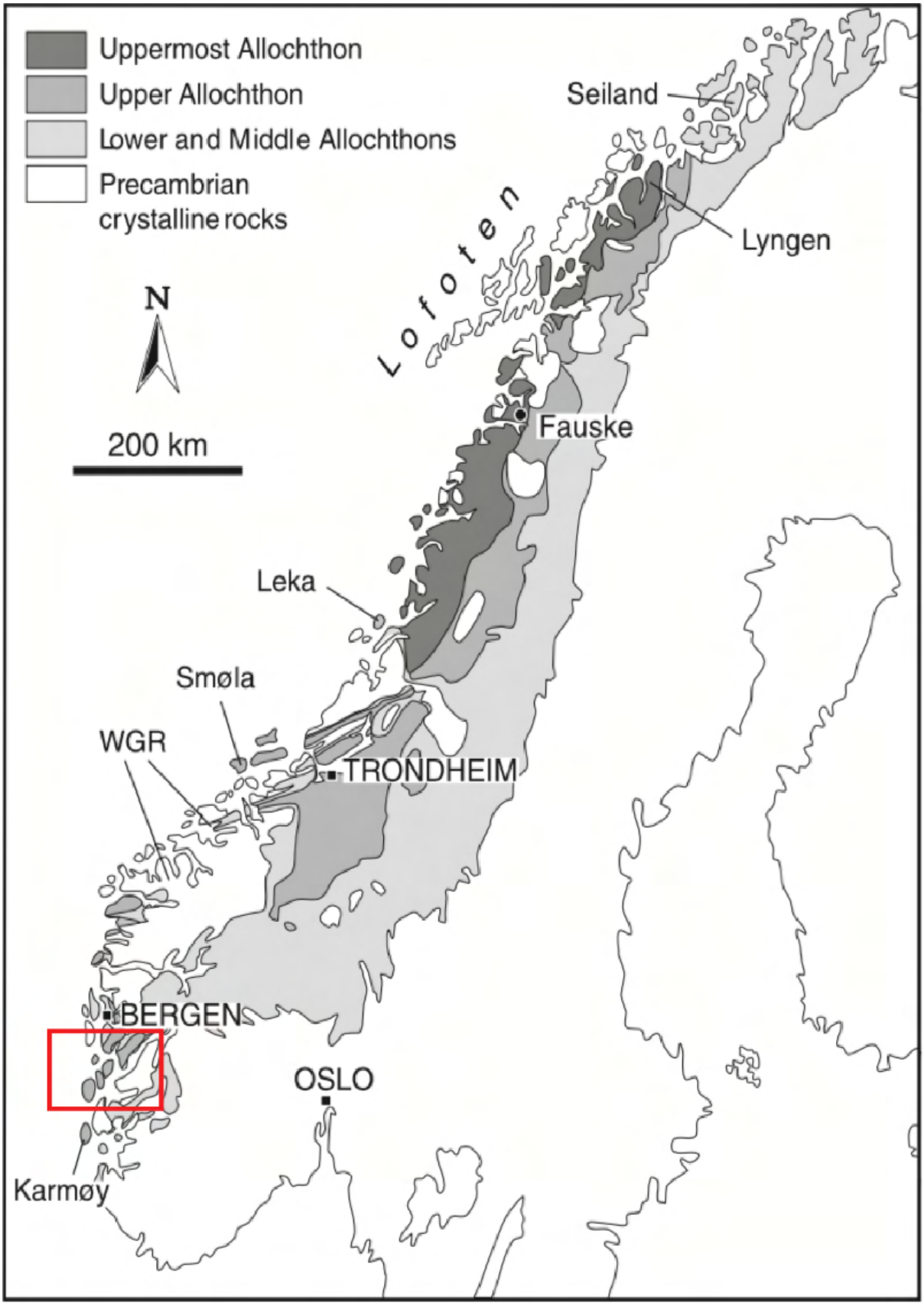


Figure 1: Geological map of Norway showing the extent of the main tectonic nappes of the Scandinavian Caledonides with the Sunnhordaland region marked by the red square. Slightly modified after Roberts (2003).

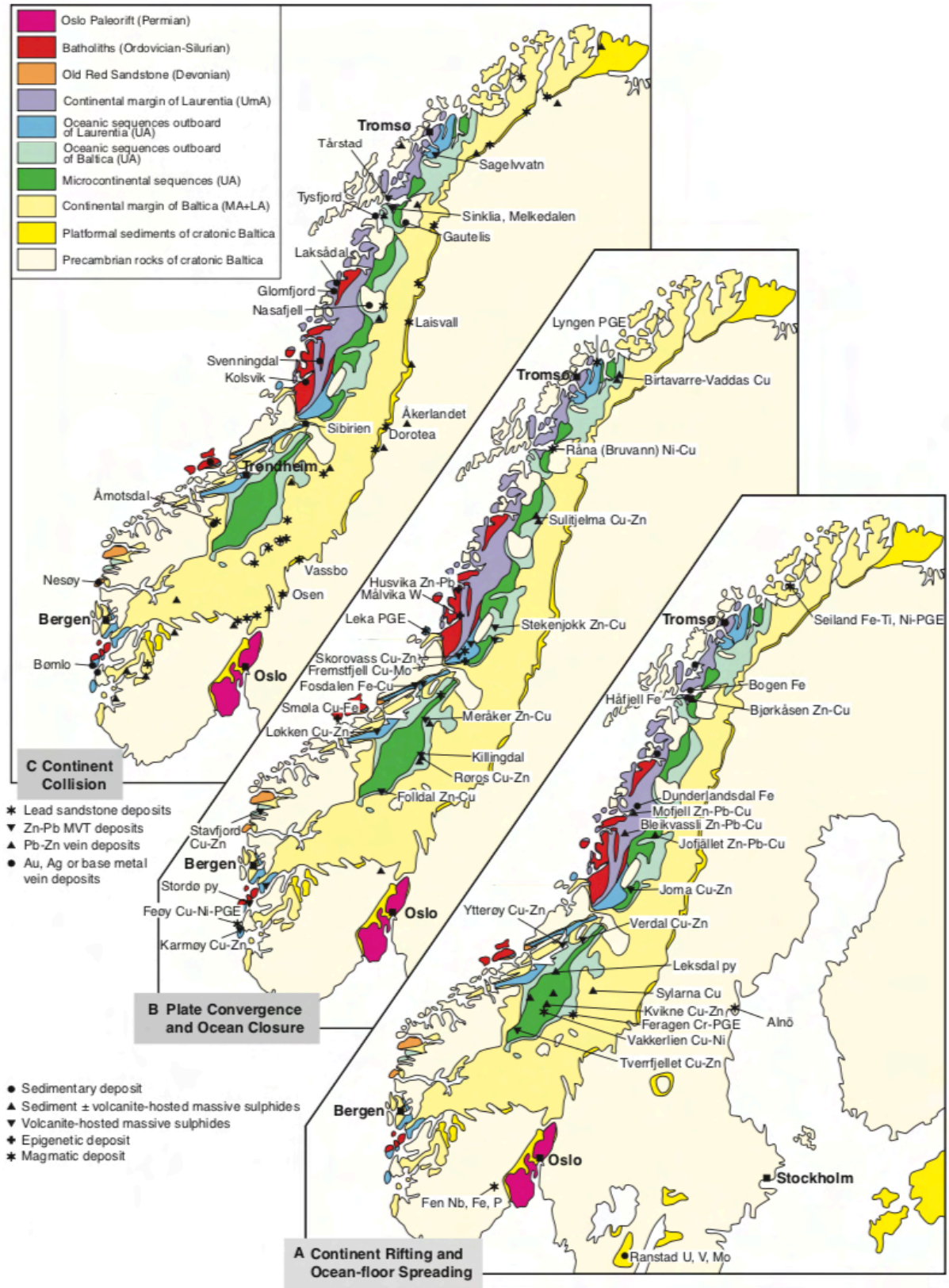


Figure 2: Geological map of the Scandinavian Caledonides showing distribution of various type of mineral deposits from the plate tectonic perspective. From Grenne et al. (1999).

## 2.2 Tectonics of the Hardangerfjord area

In the aftermath of the Caledonian orogeny, orogenic collapse led to an extensional tectonic regime in the Devonian with related deformation being traceable for 200 km, from the foreland to the western coast of Norway (Fossen and Rykkelid, 1992). Low angle extensional detachment faults are believed to have reactivated the Caledonian basal thrusts, sliding back on the décollement zone (Fossen and Rykkelid, 1992). The Hardangerfjord Shear Zone (HSZ) constitutes one of these major tectonic features in the Sunnhordaland region and formed along an already existing Proterozoic shear zone (Fossen and Hurich, 2005). The displacement is approximated to 10-12 km (Fossen and Hurich, 2005) separating the Ordovician outboard terrane from the Precambrian basement (Figure 3). This divide between the tectonic units is marked by Bømlafjorden/Hardangerfjorden in Sunnhordaland, with the exceptions of the Lower and Middle Allochthons, forming a monoclinal structure which crops out on the other side of the fjord (Fossen and Hurich, 2005). Another major tectonic feature is the Sunnhordaland Fault following approximately the same orientation as the HSZ (Andersen and Jansen, 1987a), and the fault separates the igneous, island-arc and ophiolitic lithologies from the Langevåg Group. The extent of VMS deposits in the region are defined by the HSZ and are exclusively hosted within the outboard terrane west of the fjord (Figure 3). The HSZ along with the Sunnhordaland Fault acts as limiting factors for the potential area in which deposits can occur in the region of which is further detailed in section 2.5.

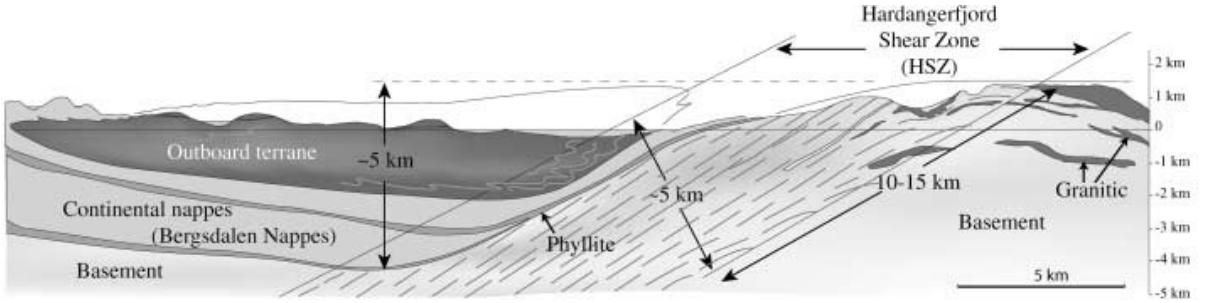


Figure 3: Cross section describing the tectonic relations related to the Hardangerfjord Shear Zone. VMS deposits in the region are exclusively hosted within the ophiolitic outboard terrane with their extent defined by the shear zone. From Fossen and Hurich (2005).

## 2.2 The ophiolitic outboard terrane in south western Norway

The southwestern part of Norway contains elements of ophiolites, igneous and island-arc complexes with several related sedimentary basins (Figure 3). Ophiolite complexes are separated into Early Ordovician ophiolites that are present between Bergen and Stavanger (Gullfjellet, Lykling, Karmøy) (Figure 3), and the younger Late Ordovician Solund-Stavfjord Ophiolite Complex located in the Ytre Sogn and Sunnfjord districts to the north. The first generation of ophiolites formed in an intra-oceanic arc environment around 490 Ma, and later

the Solund-Stavfjord ophiolite developed around 445 Ma in a back-arc basin prior to the final collision between Laurentia and Baltica (Pedersen et al., 1988).

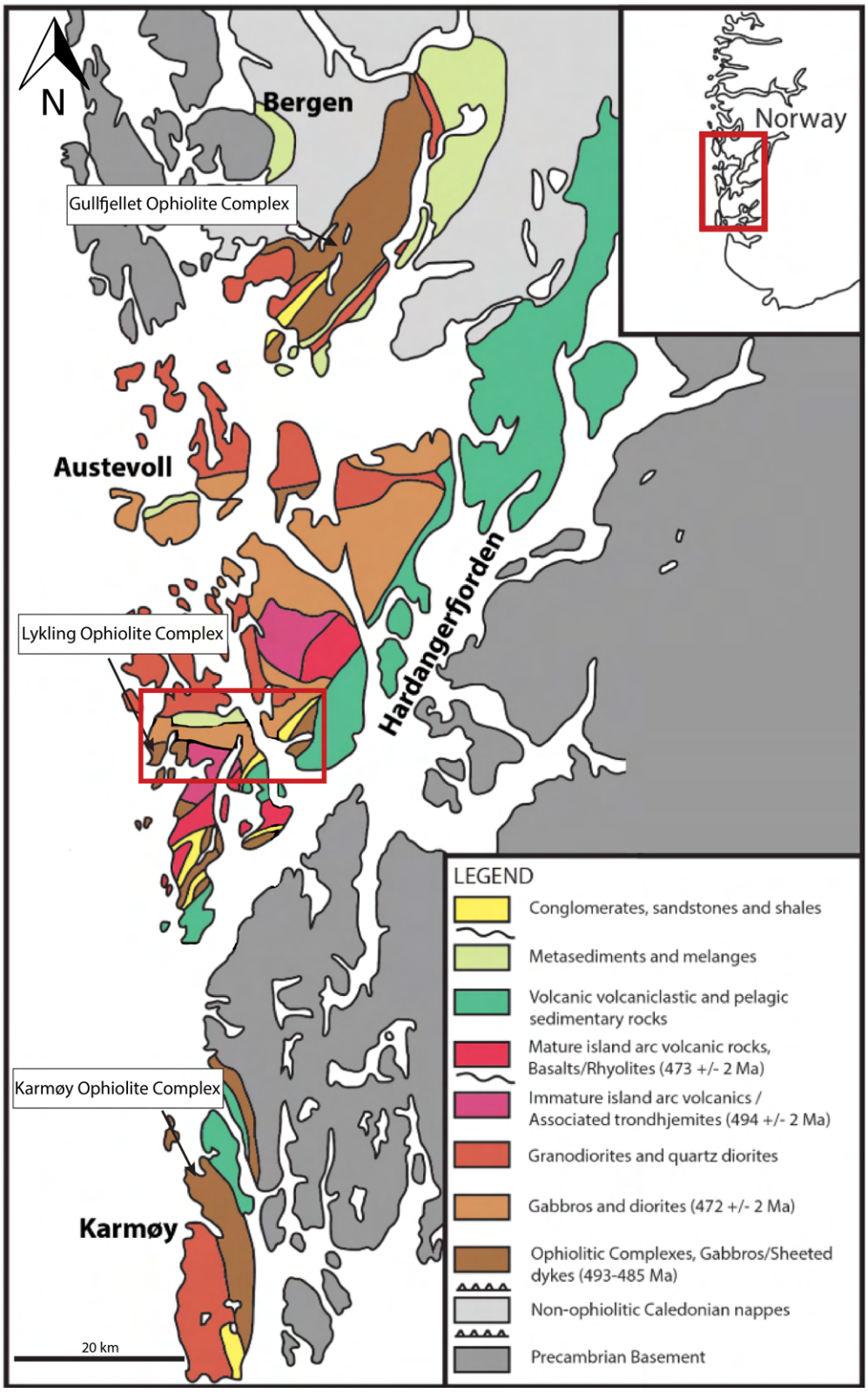


Figure 4: Geological map of the ophiolitic outboard terrane in southwestern Norway. The ophiolite complexes are marked on the map with arrows. The red square marks the area covered by Figure 5. Modified after Pedersen and Dunning (1997) by Viken (2017).

## 2.3 The geology of Bømlo and relevant parts of Stord

The geology of the study area is composed of five main lithostratigraphic units: The Lykling Ophiolite Complex, the Geitung Unit, the Langevåg Group, the Siggjo Complex, and the Vikafjord Group (Figure 5-6) (Brekke et al., 1984). All units and complexes are described in chronological order from oldest to youngest with emphasis on tectonic environment and relevance to VMS deposits. Figure 5 summarizes/illustrates the following description of the various units with locations of studied deposits marked on the map for reference. Figure 6 illustrates the tectonic relations of the units.

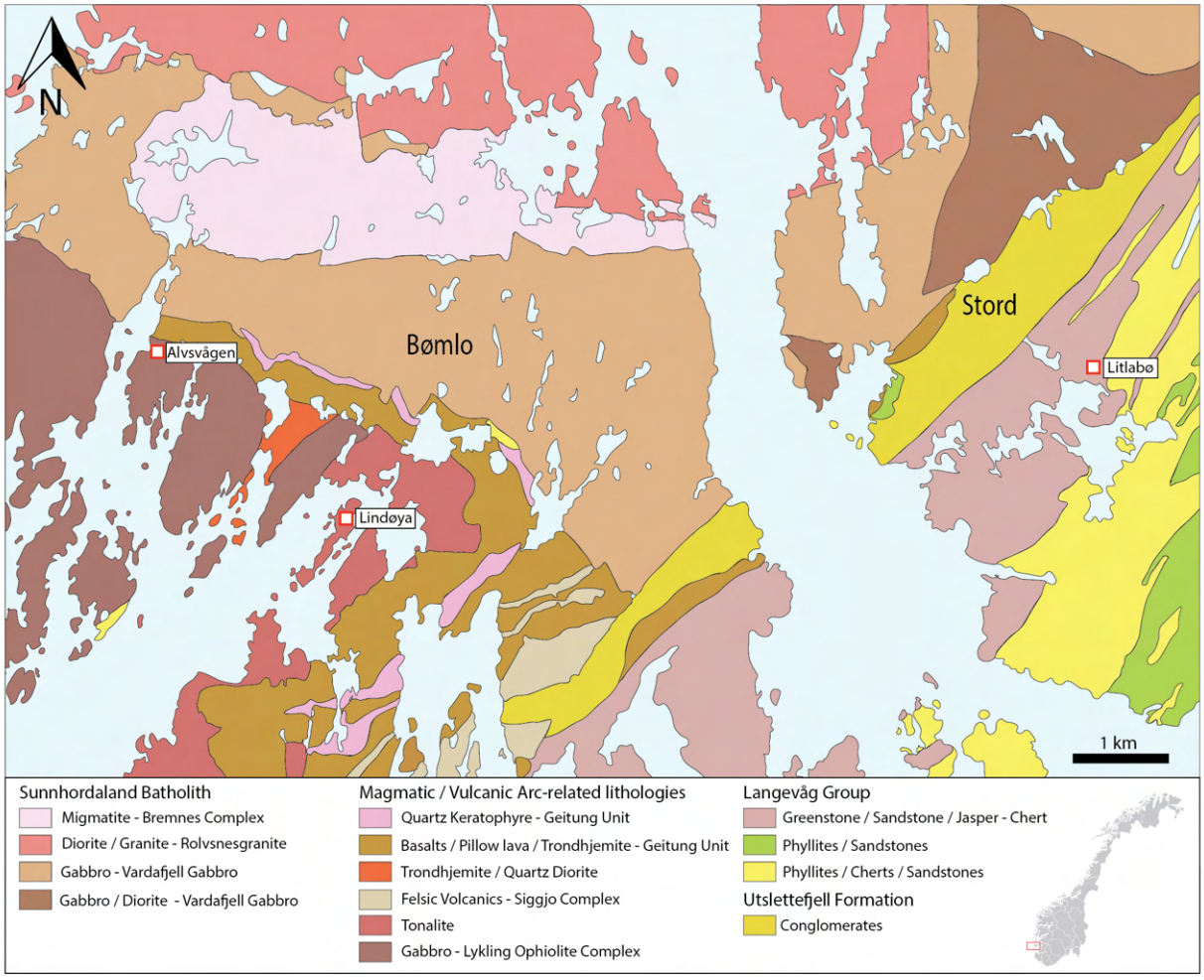


Figure 5: Geological map of the Bømlo and Stord areas with the marked locations of the studied VMS deposits (Litlabø, Lindøya and Alvsvågen). Redrawn geological map with structural data (1:250000) from NGU, 20.05.2021 (https://geo.ngu.no/kart/bergrunn_mobil/)

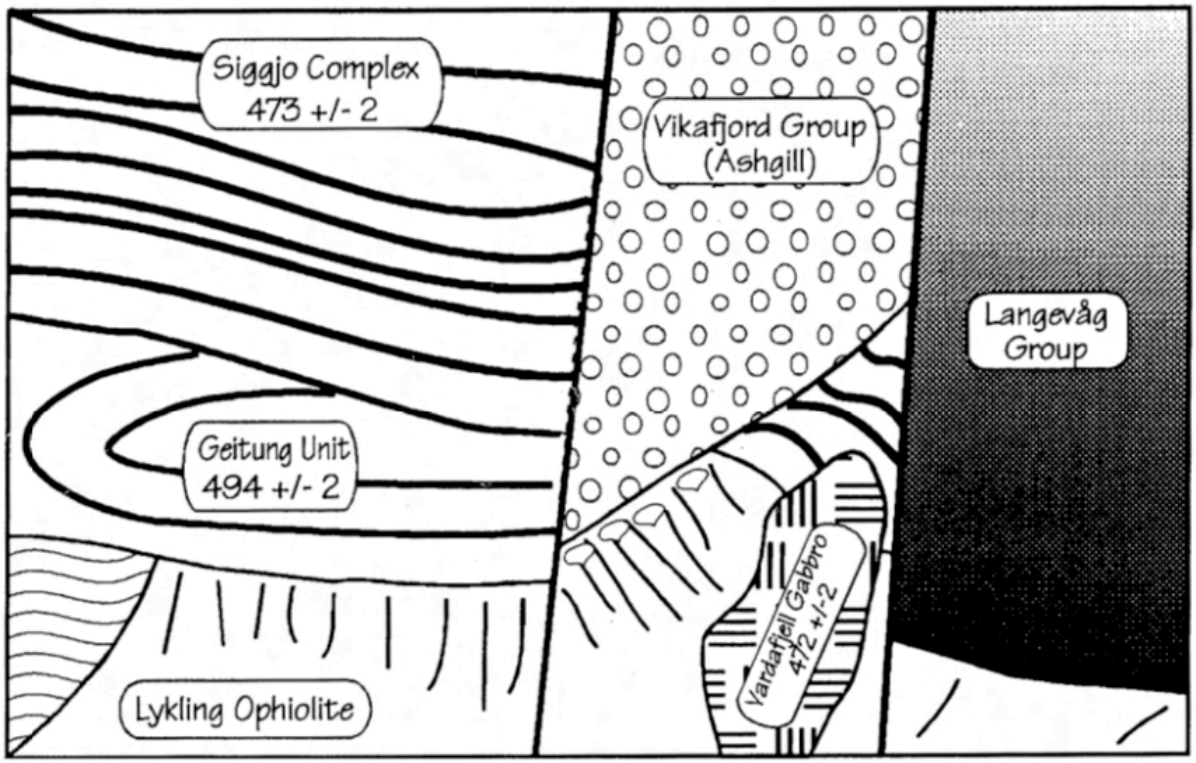


Figure 6: Illustration of the stratigraphic and tectonic relations between the stratigraphic units on Bømlo. From Pedersen and Dunning (1997).

### 2.3.1 The Lykling Ophiolite Complex and Geitung Unit

The stratigraphically lowermost unit on Bømlo island is the Lykling Ophiolite Complex which is comprised of an almost complete succession of oceanic crust (Figure 5-6) (Nordås et al., 1985). The ophiolite is composed of serpentinite, layered and massive gabbros, sheeted dykes and pillow lavas (Brekke et al., 1984). Nordås et al. (1985) describes the lithostratigraphy with the lowermost parts containing lenses of chromite-bearing serpentinite stratigraphically overlain by occasionally layered gabbro with the higher parts of the succession consisting of greenstones, dykes-swarms and pillow lavas. The absolute age of the ophiolite complex is unknown. However, a Late Cambrian - Early Ordovician age is suggested as the ophiolite is similar to other ophiolites hosted within the outboard terrane (Gullfjellet, Karmøy) (Pedersen et al., 1988). Structural observations by Brekke et al. (1984) support a similar age due to the ophiolite being the stratigraphically lowermost unit on Bømlo. Based on the ophiolite having the structure of an oceanic crust, a tholeiitic geochemical signature and a subduction-related trace element composition, the ophiolite is proposed to have formed in a spreading center situated above a subduction zone (Pedersen and Dunning, 1997).

Immature island-arc lithologies of the Geitung Unit unconformably overlay the Lykling Ophiolite Complex (Figure 6) (Brekke et al., 1984; Nordås et al., 1985). Trace element

signatures for the unit with Nb and Ta depletions are comparable to that of modern island arc tholeiitic volcanics (Brekke et al., 1984; Pedersen and Dunning, 1997). The rocks of the Geitung Unit are a mixture of extrusive and sedimentary rocks comprised of greenstones, dacites and volcanoclastic breccias with interbedded sediments (Brekke et al., 1984). The greenstones consist of hyaloclastites, pillow lavas and micro-pillow lavas with both massive and autobrecciated submarine lavas interbedded (Brekke et al., 1984). Basaltic-andesites from the Geitung Unit are dated to 494 ± 2 Ma (Pedersen and Dunning, 1997). Bodies of tonalite, trondhjemite and dacitic dykes have intruded both the Lykling Ophiolite Complex and the Geitung Unit (Nordås et al., 1985). Saltvedt (in prep.) dated the trondhjemite to 484 ± 6 Ma.

### 2.3.2 The Langevåg Group

The Langevåg Group represents a volcano-sedimentary complex cropping out in the southern parts of Bømlo and Stord (Figure 5). The Langevåg Group is composed of six formations that make up the 1250 m thick succession (Figure 7). The lowermost Krekjebær Formation consists of subaerial, mainly mafic, volcaniclastic breccia and lavas (Nordås et al., 1985). The overlying Kyrkjetuft Formation is predominantly composed of radiolarian cherts, volcaniclastic debris flows, turbidites, tuff, and possible submarine pyroclastic flows. The Vorland Formation consists of green phyllites and sandstones interbedded with pillowed and massive, often vesicular, greenstones with some radiolarian cherts interbedded (Brekke et al., 1984; Nordås et al., 1985). The thickest chert unit belongs to the Hesthaugen Formation with a thickness of over 100 m. Overlaying is the Stavaneset Formation exhibiting similar characteristics as the Vorland Formation. Uppermost in the Langevåg Group, the Vespestad Formation consist of black phyllites and quartz-rich turbidities (Nordås et al., 1985). The Litlabø VMS deposit is hosted within the Kyrkjetuft Formation and is interbedded within pillowed and massive basalts, black shale, cherts and jaspers (Grenne and Slack, 2019) and is overlain by the Vorland Formation. According to Nordås et al. (1985), the Langevåg Group reflects a formation and progressive deepening of a marine back-arc basin. The Langevåg Group has previously been described as the youngest unit on the island of Bømlo (Nordås et al., 1985) because the unit is overlain by limestones containing fossils of the Ashgillian age (Brekke, 1983). The Langevåg Group also shows tectonic contact with the Ashgillian age rocks of the Vikafjord Group and the Siggjo Complex (Nordås et al., 1985) together with a primary unconformable contact with the Lykling Ophiolite Complex (Figure 6). On Karmøy (Figure 4), the Torvastad Group shows geochemical

and lithostratigraphic similarities to the Langevåg Group which would indicate an Early Ordovician age.

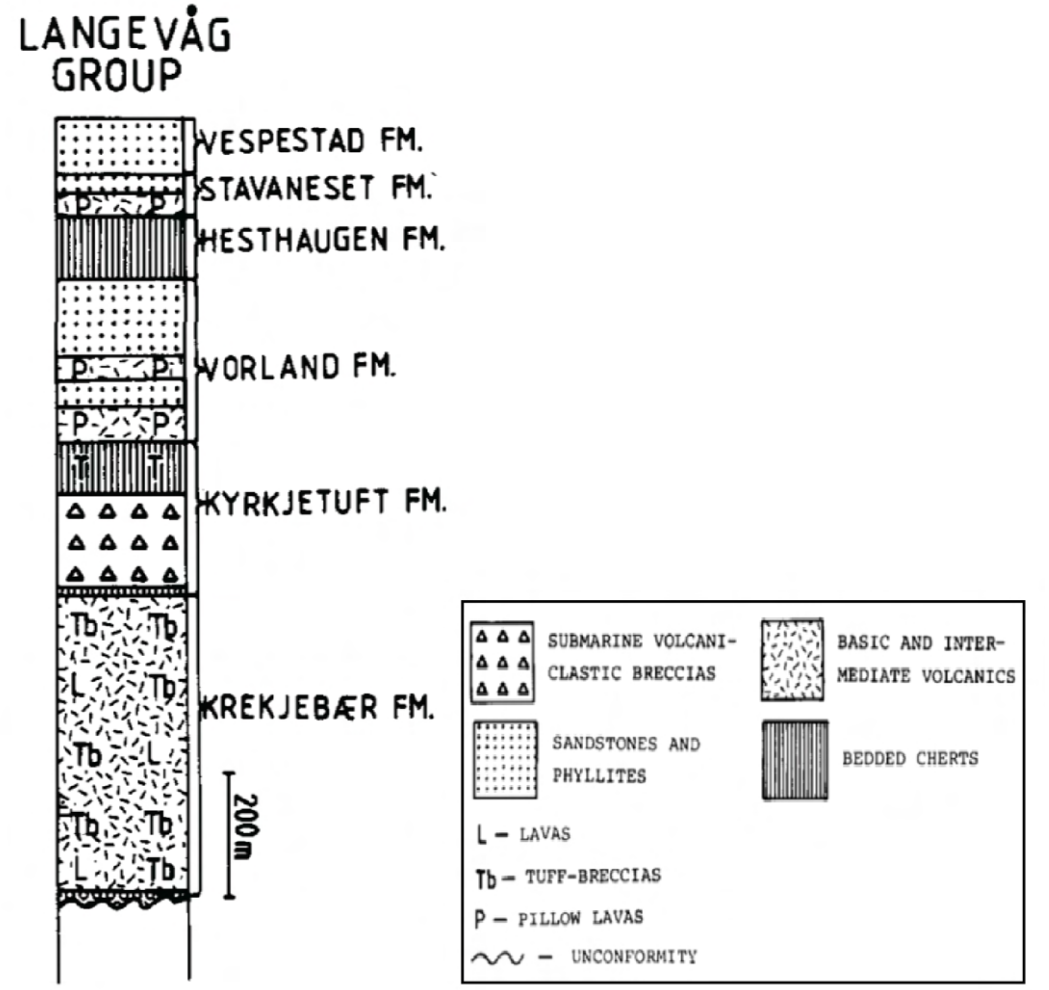


Figure 7: Illustration showing the stratigraphy of the volcano-sedimentary Langevåg Group. Modified after Brekke et al. (1984).

### 2.3.3 The Siggjo Complex

The Siggjo Complex is composed of subaerial basalts, andesites and rhyolites of calc-alkaline composition (Nordås et al., 1985). The complex unconformably overlay both the Lykling Ophiolite Complex and the Geitung Unit (Brekke et al., 1984). Andesite from the Siggjo Complex is dated to 473 ± 2 Ma (Pedersen and Dunning, 1997).

### 2.3.4 The Vikafjord Group

The Vikafjord Group is exposed in the core of major synclines as a result of erosion with the northern limb overlaying the Siggjo Complex and the southern limb overlaying rocks correlated with the Lykling Ophiolite Complex (Nordås et al., 1985). At the base of the group, polymict alluvial debris flows make out the lowermost Roaldsfjord Conglomerate (Brekke et al., 1984).

The overlaying Bergesvatn Formation indicates a marine transgression characterized by intercalation of fossiliferous limestones and calcareous phyllites. A coarsening upwards sequence of turbidites follows and is superseded by sub-arkosic plane parallel laminated sandstone, indicating coastline progradation that forms the base of the Sagvatn Formation (Nordås et al., 1985). On top of the Vikafjord Group the Eriksvatn Formation consists of subaerial mafic lavas (Brekke et al., 1984)

### 2.3.5 The Sunnhordaland Batholith

The Sunnhordaland Batholith is an intrusive magmatic body that covers an area of approximately 1000 $km^2$ (Figure 4-5) (Andersen and Jansen, 1987b). The batholith covers parts of Tysnesøy, Reksteren and the northern parts of Bømlo and Stord (Figure 5) and intrudes both the Lykling Ophiolite Complex and the Geitung Unit (Figure 6). The batholith is composed of gabbros, migmatites, meta-diorites and granodiorites (Andersen and Jansen, 1987b). Dating of the Vardafjell Gabbro gave an age of 472 ± 2 Ma (Pedersen and Dunning, 1997), with the younger Krossnes Granite giving an age of 468 ± 3 Ma (Scheiber et al., 2016). The absolute ages of the batholith are similar to the age of the Siggjo Complex (Pedersen and Dunning, 1997).

## 2.4 The evolution of the ophiolitic outboard terrane

The formation of the ophiolitic outboard terrane that is exposed in the south western part of Norway (Figure 4) is complex and formed from several tectonic and crust forming processes. In the following section a model for the evolution of the terrane will be detailed based on previous work in the Bømlo, Stord and associated geological areas in the south western parts of Norway.

### 2.4.1 Formation of an arc-ophiolite complex

The formation of oceanic crust related to subduction zone magmatism in the Iapetus Ocean most probably occurred over a period of 20 million years during the Late Cambrian and Early Ordovician (Pedersen et al., 1988). Of the ophiolite complexes that are preserved in south western Norway (Figure 4) two have been dated (Karmøy Ophiolite Complex - 493 +7/-4 Ma / Gullfjellet Ophiolite Complex - 489 ± 3 Ma) (Pedersen et al., 1988). The Lykling Ophiolite Complex on Bømlo is believed to have formed during the same time period (Pedersen et al., 1988). The extrusion of shallow marine and subaerial magmatism over an supra-subduction

zone mark the formation of the immature island-arc lithologies preserved in the Geitung Unit (Pedersen and Dunning, 1997). Large bodies of trondhjemite and plagiogranite later intruded both the Lykling Ophiolite Complex and the Geitung Unit and are dated to 484 ± 6 Ma (Saltvedt, in prep.) indicating ongoing magmatism prior to the Taconian collision and accretion. In a related deepening back-arc basin, the Langevåg Group was deposited, and it is either directly or spatially associated with many of the known VMS deposits in the Stord area. The evolution of the island-arc and related magmatism in the Iapetus Ocean ended with accretion of the ophiolite, island-arc and metasedimentary lithologies upon the Laurentian margin during the Taconian orogeny (Roberts, 2003) and commencement of a period of orogenesis.

### 2.4.2 Arc continental collision, orogenic collapse, related extension and renewed magmatism

The period of orogenesis during the Taconian phase was short lived and orogenic collapse led was followed by a extensional regime and thinning off the crust resulting in renewed magmatism (Pedersen 2021, personal communication). This younger generation of magmatism and volcanism in the Bømlo and Stord areas exhibits evolved calc-alkaline characteristics similar to magmatism found on Karmøy (Pedersen and Dunning, 1997). The Sunnhordaland Batholith exhibits a magmatic evolution from gabbroic to granitic and represent underplating as a result of the thinning crust together with the mature volcanics off the Siggjo Complex representing the extrusive part of the system (Pedersen 2021, personal communication). The Sunnhordaland Batholith and Siggjo Complex are linked in time exhibiting similar age relations with the batholith forming around 472 ± 2 Ma and the Siggjo Complex 473 ± 2 Ma (Pedersen and Dunning, 1997). Migmatites in the Sunnhordaland Batholith also features inherited zircons of Precambrian age which are too old to be inherited from Baltica (Viken, 2017; Pedersen et al., 1997; Slotnes, in prep.). Together with fossil evidence (Pedersen et al., 1992) an affinity of the mentioned units to the Laurentian margin is most likely. In a deepening basin forming as a result of the orogenic collapse and extension, the Vikafjord Group was deposited. Possibly, these extensional basins can be linked to the formation the younger Solund-Stavfjord Ophiolite Complex (Pedersen 2021, Personal communication).

### 2.4.3 Continental collision and the emplacement off nappes onto the Baltic margin

The closure of the Iapetus Ocean separating the two major continents Laurentia and Baltica occurred in Late Silurian and Early Devonian (Roberts, 2003). Later orogenic collapse led to

extensional tectonics along the HSZ in the Sunnhordaland region which is described in detail within subchapter 2.1.2.

## 2.5 Volcanogenic massive sulfide deposits in Sunnhordaland

The Sunnhordaland region hosts more than 100 ore occurrences varying from gold deposits hosted in quartz veins to various VMS type deposits (Figure 3; Wulf, 1996). Almost all occurrences are hosted by the Upper Allochthon in similar tectonic settings as known Norwegian sulfide districts with examples like Løkken, Folldal and Grong (Figure 2) (Raaness et al., 2020). The deposits of the Sunnhordaland region belong to the Hardanger Cu-Zn-Au Province that extends from Bømlo and Stord in the south west to Storhidleren in the north east (Poulsen, 2012; Raaness et al. 2020) (Figure 8).

The Alvsvågen and Lindøya VMS deposits are the largest deposits in the Bømlo area. The lithologies hosting VMS deposits on Bømlo is the Lykling Ophiolite and the Geitung Unit (Figure 8). Several minor occurrences similar to the Lindøya deposit is hosted in close relation with several of them being the subject of minor mining activities throughout the years (Wulff, 1993). Most of these minor occurrences contain low amounts of base metals and are referred to as “Vasskis”, with some exceptions containing some minor enrichments in base metals (Wulff, 1993). All deposits hosted within the Geitung Unit have been classified as exhalative VMS deposits (Wulff, 1993).

On Stord, the Litlabø VMS deposit is hosted by the Langevåg Group is the largest VMS deposit in the Sunnhordaland region and have historically been mined for 9 Mt of primarily iron rich sulfides with minor amounts of zinc (Raaness et al., 2020). Several minor economically insignificant Cu-Zn VMS occurrences are also located further north west of the fjord (Figure 8) and are hosted within the greenstones of the Varaldsøy-Ølve Complex (Dietrichson and Foslie, 1955), and have historically been mined with a total production of 0.5-1 Mt ore (Raaness et al., 2020). The deposits have been prospected anew in more recent times, however no reports of these investigations are available (Raaness et al., 2020).

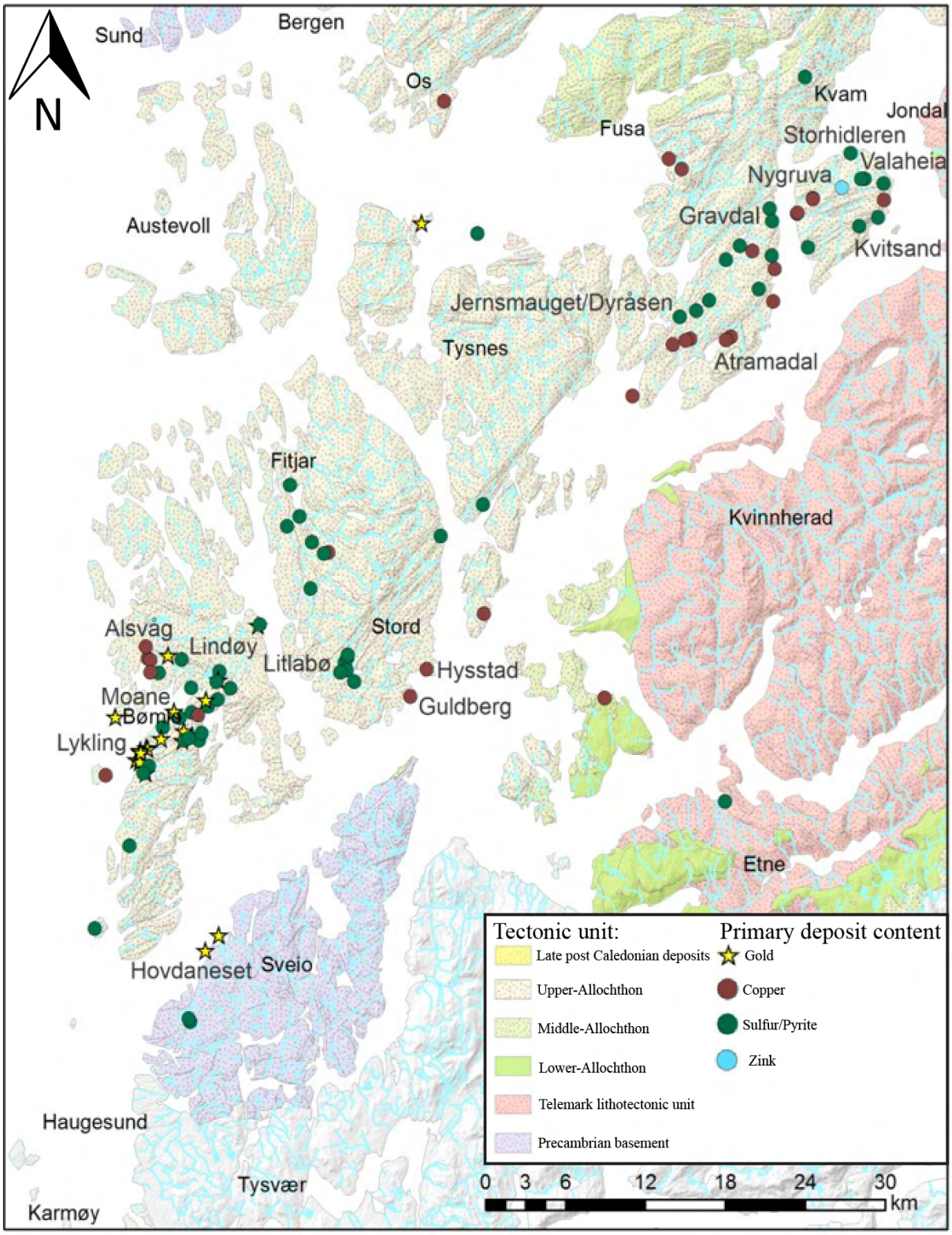


Figure 8: Geological map of the mineral occurrences in the Hardanger Cu-Zn-Au Province grouped by their main commodities. Slightly modified after Raaness et al. (2020).

# 3 Study areas

## 3.1 The Alvsvågen area

The Alvsvågen deposit, on the Bømlo island, is hosted by the Lykling Ophiolite Complex that is overlaid by the Geitung Unit greenstones in the north. Further north and to the north west the Vardafjell Gabbro of the Sunnhordaland Batholith has intruded both the Lykling Ophiolite Complex and the Geitung Unit (Figure 9). The Alsvågen deposit was mined for Cu over 3 two-year periods (1865-1867, 1882-1884, 1905-1907; Wulff, 1993).

Layered and isotropic gabbro of the Lykling Ophiolite Complex dominate the southern part of the Alvsvågen area. Further north, i.e. closer to the mineralization, the layered gabbro becomes scarcer and replaced by a mixture of both coarse- and micro-gabbroic lithologies with sharp contacts between these two types of lithologies. These features indicate a high-level gabbroic zone with micro-gabbroic dykes cutting a coarser more isotropic gabbroic lithology. Another generation of minor basaltic dikes cuts into the area with an east-west orientation and are randomly distributed over the area and are separated from the ophiolitic dykes by appearance and orientation together with minor felsic intrusions likely originating from the batholith. The area has been affected by regional metamorphism during both the Taconian and Caledonian orogeneses and greenschist facies is suggested by Amaliksen (1983).

The Alsvågen area hosts 4 NW-SE trending shear zones (Figure 9). Two shear zones are partly exposed on the surface (Figure 10A, B, C) but historical mining activities have removed large parts of the hosted mineralization. In the field the shear zones appear to have similar orientations as the layered gabbro and features a dip of 40-60 degrees (Figure 10B) together with a strong foliation (Figure 10D). From a geophysical survey the length of the main shear zone was determined to be 250 meters with a depth of 100-200 meters (Dalsegg, 1980). The geophysical survey also identified two unexposed shear zones of which one was possibly ore bearing (Dalsegg, 1980). The sulfide mineralization in the Alsvågen area occurs in a form of disseminations and veinlets hosted by coarse- and micro-gabbroic lithologies and as more massive mineralization along the NW-SE oriented shear zones.

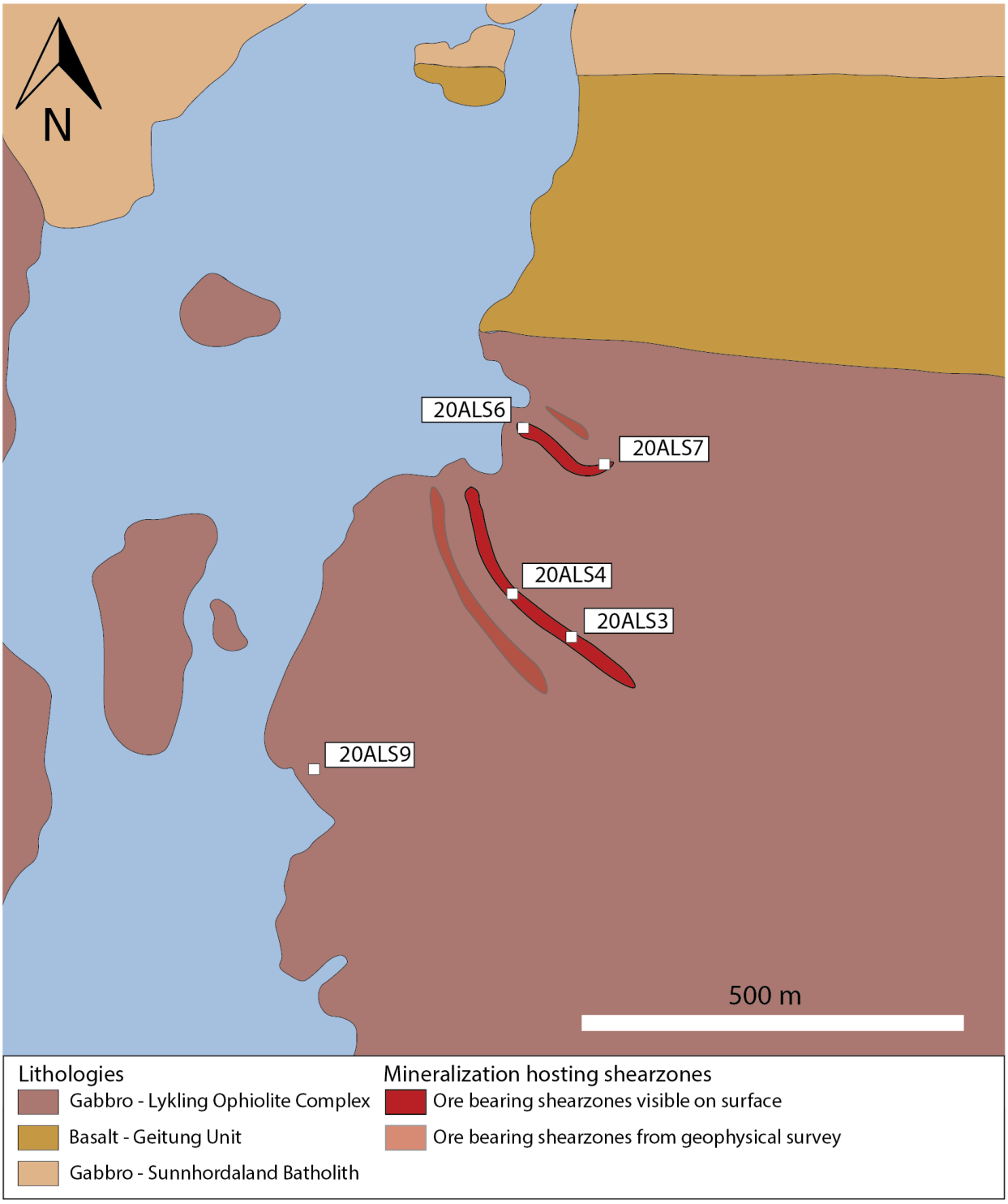


Figure 9: Geological map of the Alvsvågen area. Ore bearing shear zones are shown in red. Sampling location of the samples are also marked. Redrawn geological map with structural data (1:250000) from NGU, 20.05.2021 (https://geo.ngu.no/kart/bergrunn_mobil/)

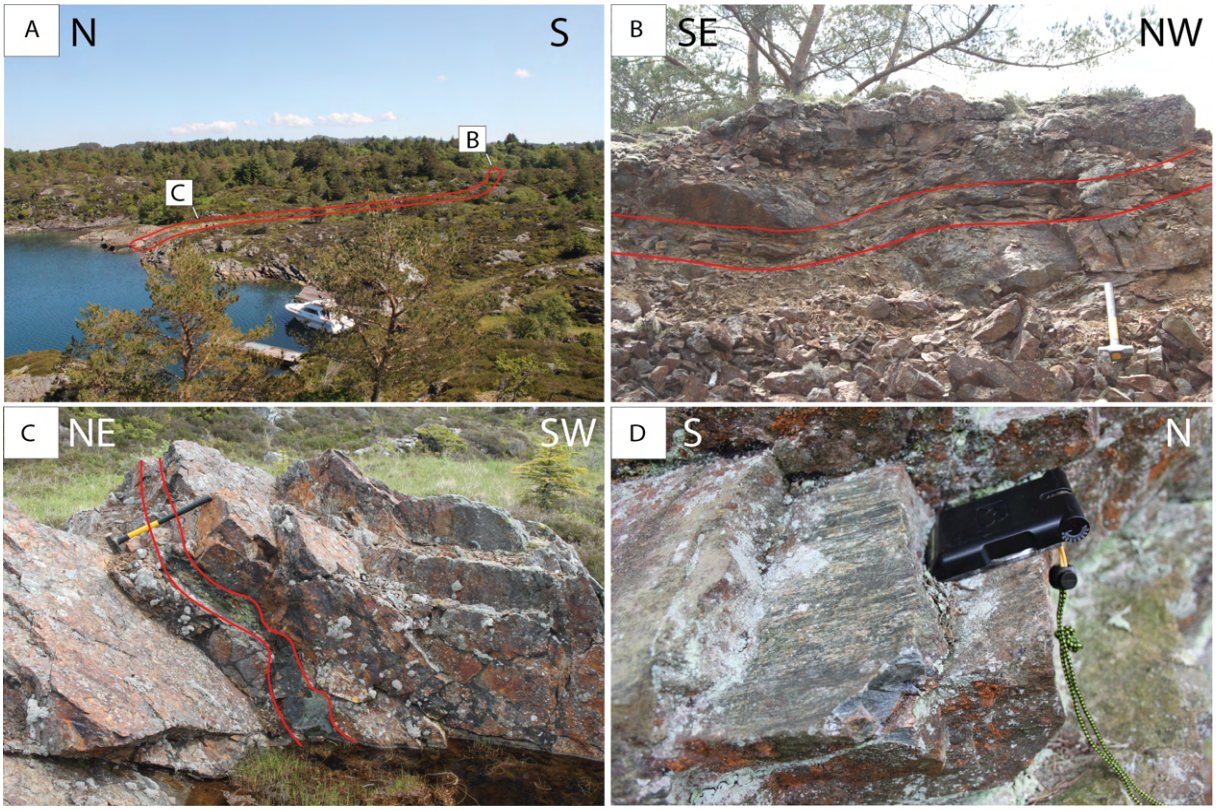


Figure 10: A) Overview over the northern shear zone (exaggerated) at Alvsvågen with the two shear zones exposures and mining sites marked. (B) Shear zone exposed close to one of the minor mines. Sledgehammer for scale. C) Shear zone exposure were one can clearly recognize the width and dip. Sledgehammer for scale. C) Shear zone foliation with compass for scale.

## 3.2 The Lindøya area

The Lindøya island is mostly composed of trondhjemite which has intruded the Geitung Unit and the Lykling Ophiolite Complex (Figure 11). Micro-gabbro and basalt are exposed along the central part of the island but their extend is still unknown. Another generation of basaltic dykes cuts into the trondhjemite and possibly the micro-gabbro/basaltic lithologies and are related to the Siggjo volcanics (Viken, 2017). Within the micro-gabbro/basaltic lithologies there are four open pits that were mined for a short period (~1865-75; Wulff, 1993). The main ore body is recognized in association with the mafic lithologies and the main ore body consist of a bedded massive sulfide mineralization. This ore is exposed over 250 meters with a thickness of upwards of eight meters (Wulff, 1993). Spatially associated there are also recognized basalt-hosted sulfide mineralization which appears as veins and disseminations. Associated with the mineralization are also chert-like lithology to which extent varies.

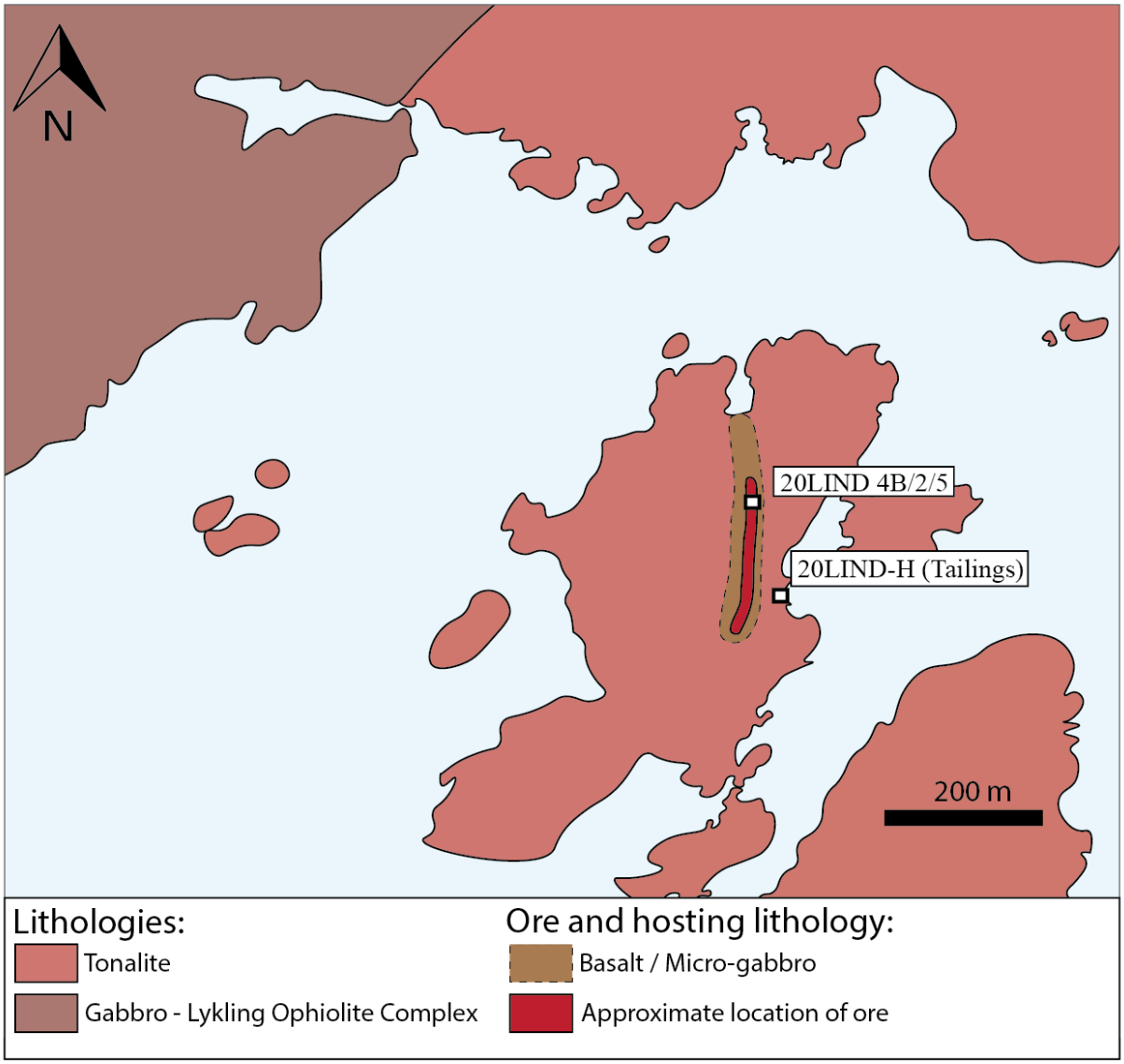


Figure 11: Geological map of the Lindøya area with the approximate location of the ore body after Wulff (1993). The extent of the micro-gabbro and basalts are not well defined and the borders to the surrounding trondhjemite are uncertain as well as relation to the mineralization are uncertain. Redrawn geological map with structural data (1:250000) from NGU, 20.05.2021 (https://geo.ngu.no/kart/bergrunn_mobil/)

## 3.3 The Litlabø area

The Litlabø mine is located at the island of Stord and is the largest out of the three deposit studied in this thesis, with an historical production of 9 Mt (Raaness et al., 2020). The deposit is hosted by the volcano-sedimentary complex of the Langevåg Group (Figure 12), which is interpreted by Nordås et al. (1984) to be formed in a deepening back arc basin setting. Around the ore body, organic rich black shale is abundant with visible sulfides disseminations on some occasions (Figure 13A). In close proximity to the shale, massive red jaspers appears in contact with thin layers of a grey silt-like lithology as well as a layered siliciclastic rock containing lenses of magnetite (Figure 13B). The jaspers also appear as a thicker more massive beds without banding on most occasions with minor amounts of banded jaspers found in contact with

a fine-grained sandstone. Minor amounts of greenstones are exposed in the area and are observed in contact with the bedded green radiolarian cherts (Figure 13C).

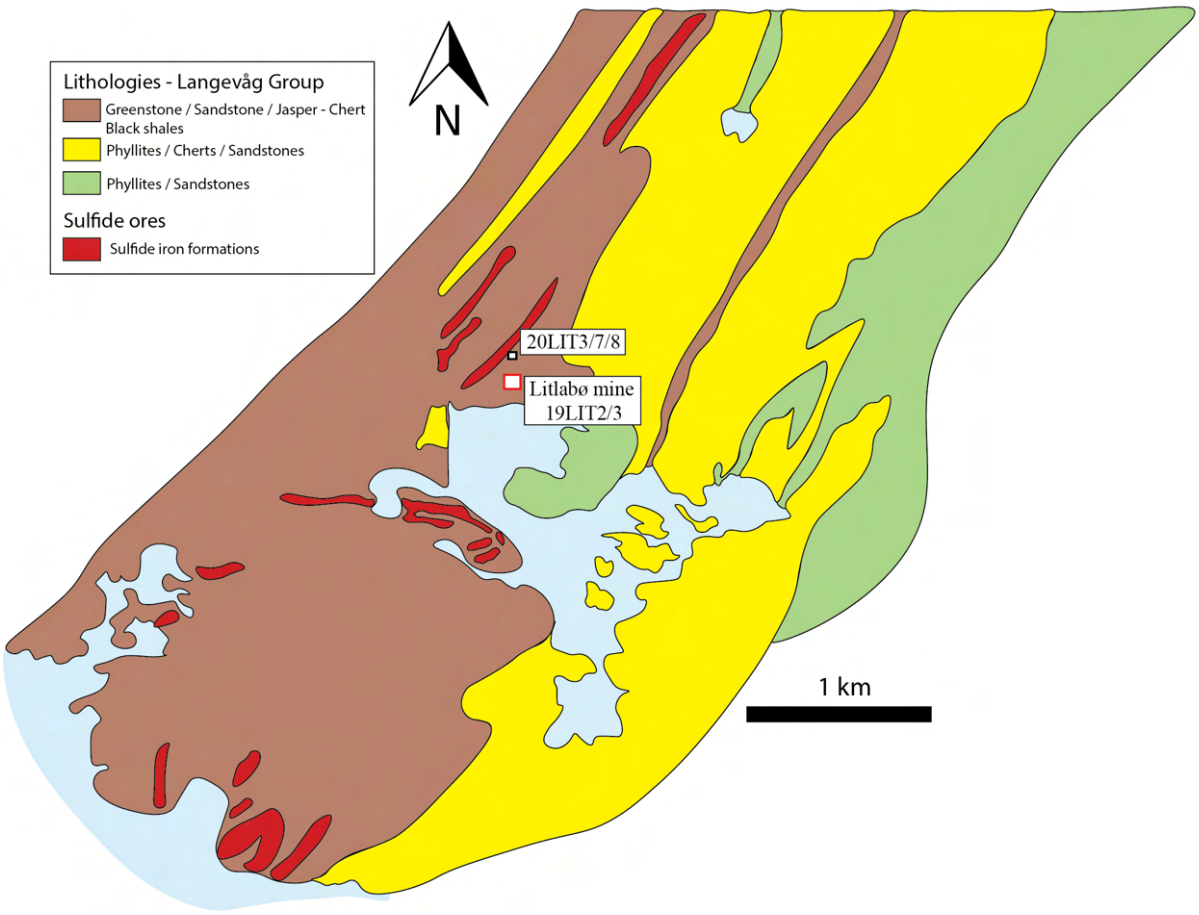


Figure 12: Geological map over the Litlabø area with sulfide ores marked together with sample locations. 19LIT2/3 were sampled from within the mine itself. Redrawn after Grenne and Slack (2019).

The sulfide iron formations primarily consist of pyrite and pyrrhotite with a low content of base metals. The ore bodies are between 50-150 meters thick (Wulff, 1993) and have almost a vertical dip clearly visible in the underground mine. The sulfide mineralization is poorly exposed on the surface as it have mostly been removed by the mining operation. Anyhow, its original extent can be recognized from the excavated areas within the mine. The sulfide mineralization in the Litlabø area can be subdivided into two main subtypes: 1) Semi-massive pyrite mineralization associated with organic rich fine-grained sediments often contains pyrite veinlets that cross-cut the primary bedding (Figure 13E) and 2) massive layered sulfide mineralization composed of pyrite and pyrrhotite (Figure 13F).

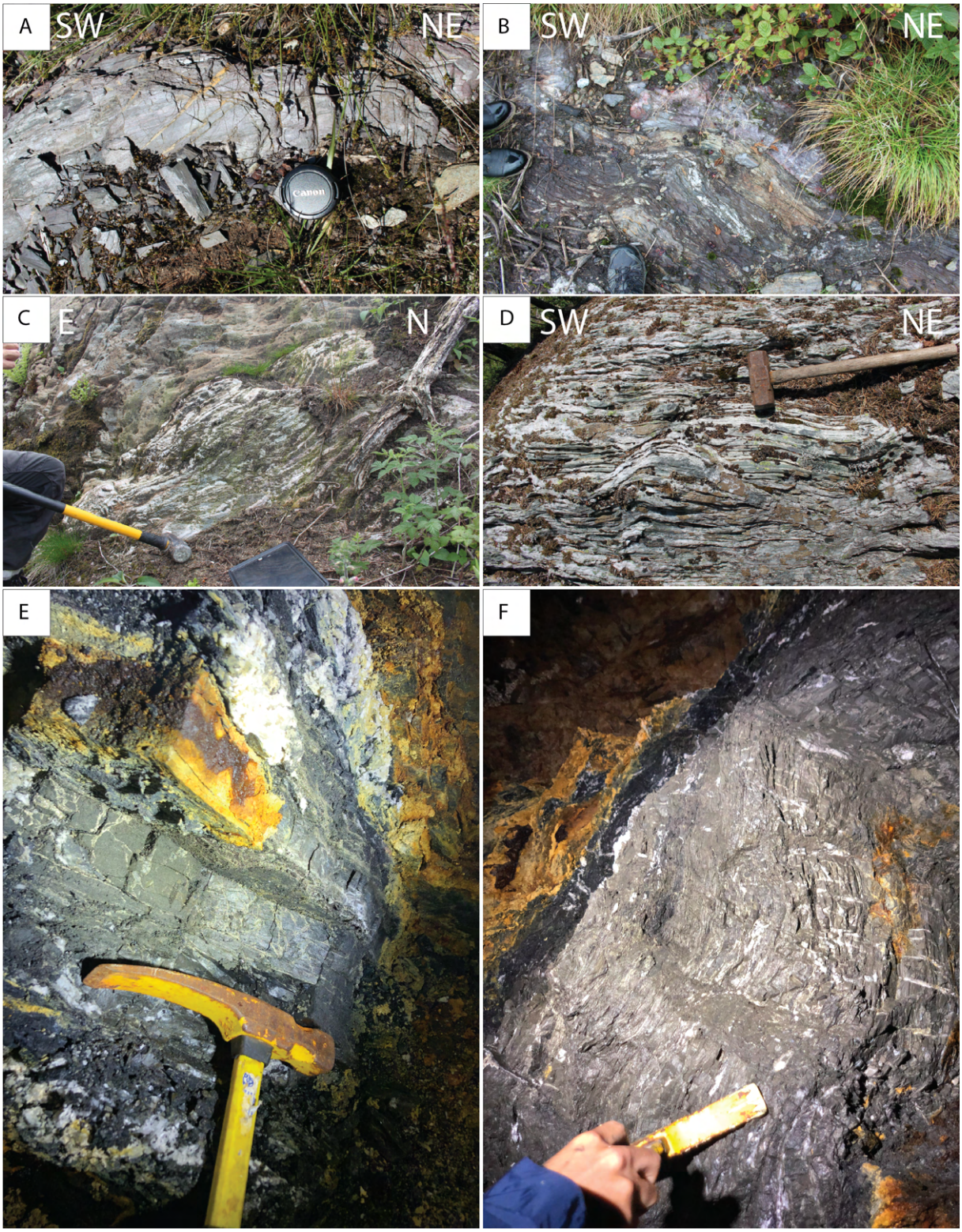


Figure 13: A) Organic rich black shale with camera lens for scale. B) Jasper, siltstone and magnetite/hematite rich layering in close proximity to the organic rich dark shale. Shoes for scale. C) Radiolarian bedded chert in contact with basalt. Sledgehammer for scale. D) Bedded radiolarian cherts with sledgehammer for scale. E) Organic rich sediments with pyrite veins disseminated. Hammer for scale. F) Massive deformed mineralization with minor white veins cross cutting. Hammer for scale.

# 4 Theoretical background

## 4.1. Volcanogenic Sulfide Deposits

Volcanogenic massive sulfide (VMS) deposits are volcanic, volcanic associated or volcano-sedimentary hosted deposits that typically have a stratiform character and consist of polymetallic massive to semi-massive sulfides (Galley et al., 2007). The deposits host many important economical commodities, primarily base metals (copper, zinc and lead) along with precious metals (gold and silver) and other byproducts, like cobalt, indium, gallium etc. (Singer, 1995). The source of metals is the crust in which the fluids circulate as a result of proximity to a magmatic heat source driving the hydrothermal circulation. Extensional tectonics forms conduits in which the fluids are contributed to the lower parts of the crust. There the fluids reach the reaction zone and is enriched in metals leached from the crust and sulfur with the latter being derived from the seawater as well as from primary magmatic sulfur (Seal, 2006). The fluids then rise through the crust and are either vented on to the seafloor as exhalatives or deposited in the main massive body by replacement features (Piercey et al., 2015).

VMS deposits do not appear as a homogenous group of deposits and can encompass a spectrum of compositions, sizes and morphologies being hosted in a variety of geotectonic settings (Barrie and Hannington, 1999; Galley et al, 1996). In an idealized example of a VMS deposit (Figure 14), there is a mound shaped strata-bound body consisting of massive sulfides on or close to the ocean floor (Galley et al., 2007). In addition to the sulfides other minerals phases such as oxides, phyllosilicates and iron oxides occur together with altered silicate wall rock (Galley et al., 2007). Underlying the massive sulfide mound is an extensive network of discordant to semi-concordant stockworks, veins and disseminated sulfides. Associated with these are haloes of hydrothermally altered host rock (Galley et al., 2007; Gibson et al., 2007)

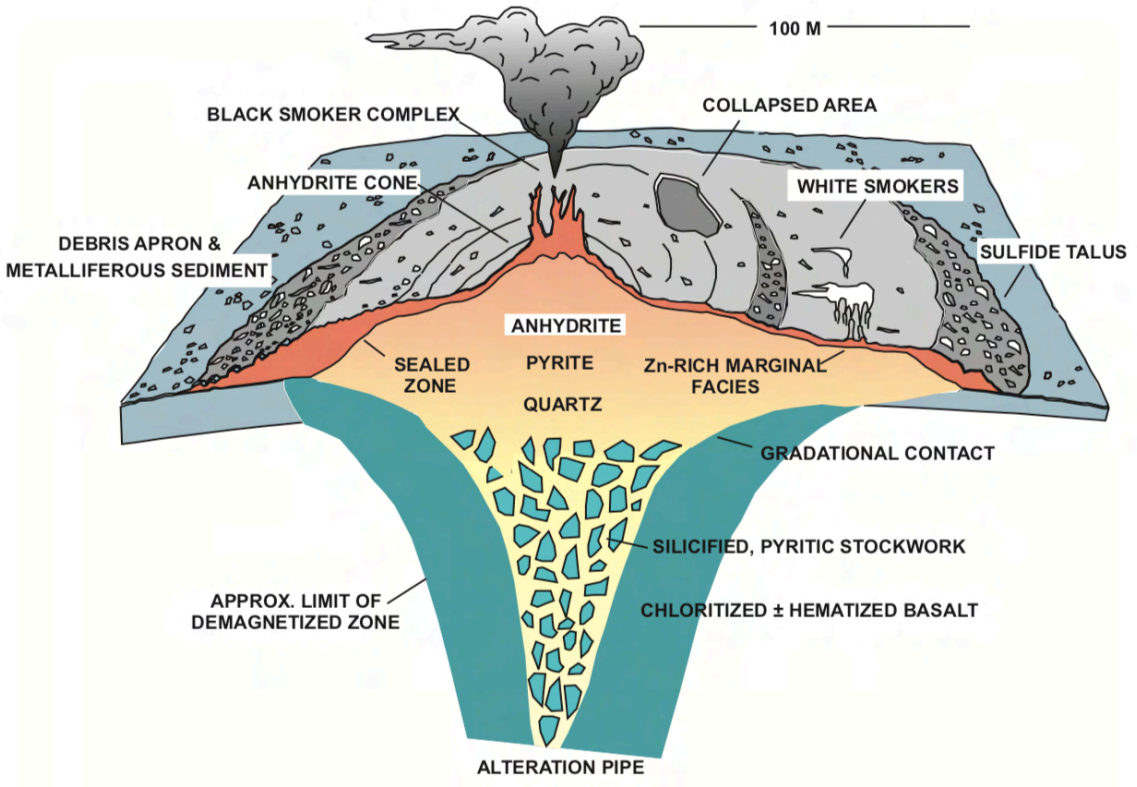


Figure 14: Idealized illustration off the TAG VMS system showing the separate parts off the deposit detailed. From Galley et al. (2007).

### 4.1.1 Classification and depositional environments

As previously mentioned, VMS deposits can be formed in a variety of submarine settings associated with extensional tectonics and magmatic activity. Several classification schemes have been proposed. One such classification is established on the base metal content and their relative abundance (Cu-Zn/Pb-Zn/Zn-Pb-Cu) by Franklin et al. (1981) and refined by Large (1992). Other classifications is based upon the gold content relative to base metals in the deposits (Poulsen and Hannington, 1995) or a specific type of deposits which are well characterized by a type locality. The latter type of classification mainly feature the Cyprus, Kuroko and Besshi type deposits (Taylor et al., 1995). The Cyprus type is usually hosted in an ophiolitic sequence associated with basaltic flows while the Kuroko type features an intermediate to felsic composition and the Besshi type represents the volcano-sedimentary hosted deposits (Taylor et al., 1995). Barrie and Hannington (1999) proposed a more detailed classification based on the geotectonic environment and the resulting host rock composition. This led to a classification scheme with five types of deposits evolving from a primitive to more evolved geochemical and geotectonic setting together with an evolution from less effusive to more volcanoclastic dominated environment combined with an increasing content of felsic

rocks (Figure 15). The five types of deposits are the mafic, bimodal-mafic, mafic siliciclastic, bimodal-felsic and bimodal siliciclastic (Barrie and Hannington, 1999).

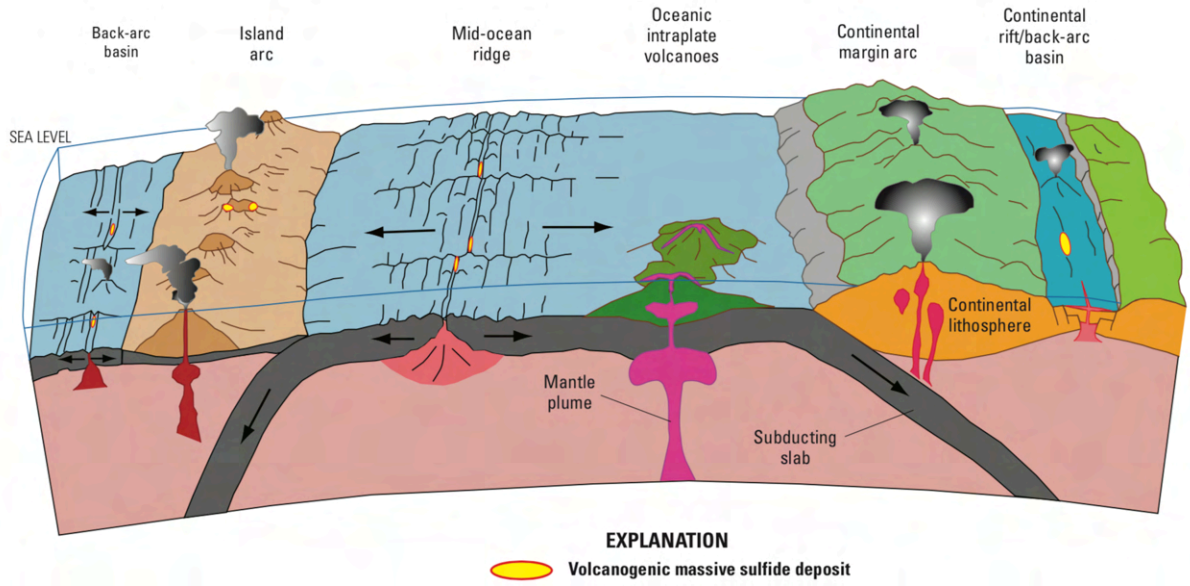


Figure 15: Model summarizing different tectonic settings for the formation of VMS deposits. From Barrie (2012), modified after Schmincke (2004) and Galley et al. (2007).

The following description regarding the different types of VMS deposits is based on the previously described classification by Barrie and Hannington (1999). The average tonnages and base metal contents are listed in Figure 16.

*Mafic type* VMS deposits are hosted by mafic rocks (>75 %) (Figure 16) and usually encompass the ophiolitic setting. Typically, the deposits are small to medium in size showing enrichment in Cu and depletion in Pb (Taylor et al., 1995). Ancient analogs are found in the Upper Allochthon in Norway with the Løkken deposit being one of the largest known ophiolite hosted VMS deposits (Grenne and Slack, 2005). Other known ophiolite hosted VMS deposits are hosted in the Troodos ophiolite (Cyprus type) and the Ordovician Bay of Islands ophiolite in Newfoundland (Galley et al., 2007). *Bimodal-mafic* (Cu-Zn) type deposits have a lower component of mafic rocks (<50 %) and varying amounts of felsic and siliciclastic rocks (Figure 16) (Barrie and Hannington, 1999). Geochemically the mafic rocks typically have a tholeiitic composition, but calc-alkaline compositions can also occur. From host rock compositions, the deposits are thought to form in immature island-arc and rifted primitive volcanic arc geotectonic environments (Barrie and Hannington, 1999). Well known examples of bimodal-mafic type deposits is the Flin Flon deposit (Syme and Bailes, 1993) and the deposits of the Noranda

district in Canada (Gibson and Watkinson, 1990). Off all the types of VMS deposits within this classification, the bimodal-mafic is the most common in the geological record (Barrie and Hannington, 1999). *Mafic-siliciclastic* type deposits are stratiform sheets of massive sulfides (Peter and Scott, 1999) hosted in mafic intrusive or volcanic rocks in association with turbiditic siliciclastic rocks (Barrie and Hannington, 1999). These are typically enriched in Cu with minor amounts of Zn and rare Pb (Peter and Scott, 1999). Well known deposits are the Windy Craggy and Besshi deposits (Barrie and Hannington, 1999), and the type can form in a variety of geotectonic settings (back-arc basins, rifted continental margins, intracontinental rifts, fore-arc and sedimented spreading ridges in proximity to continental margins) (Peter and Scott, 1999). *Bimodal-felsic* type deposits are similar to the previously mentioned bimodal-mafic type but with felsic calc-alkaline volcanic rocks as the dominant lithology (>50 %) (Barrie and Hannington, 1999). Mafic volcanic/intrusive and siliciclastic rocks occur in smaller quantities. The base metal content show variation over geological time with the older deposits containing Zn and the younger showing a relatively higher enrichment in Cu and Pb (Barrie and Hannington, 1999). The Miocene Huroko district in Japan (Horikoshi, 1990) host well-known examples of this type of deposits. The last type of deposit is the *Bimodal siliciclastic* which host similar proportions of volcanic and siliciclastic rocks (Barrie and Hannington, 1999). The deposits can feature both calc-alkaline felsic and tholeiitic mafic rocks with the former often being more abundant. Continental arc or rifted continental arc settings are often attributed as geotectonic environments, and well-known examples are the deposits of the Bathurst mining district and the Iberian pyrite belt (Barrie and Hannington, 1999). Bimodal siliciclastic type deposits host the lowest quantities of Cu of all the deposit types but do feature the highest Pb contents combined with the highest combined total tonnages (Barrie and Hannington, 1999)

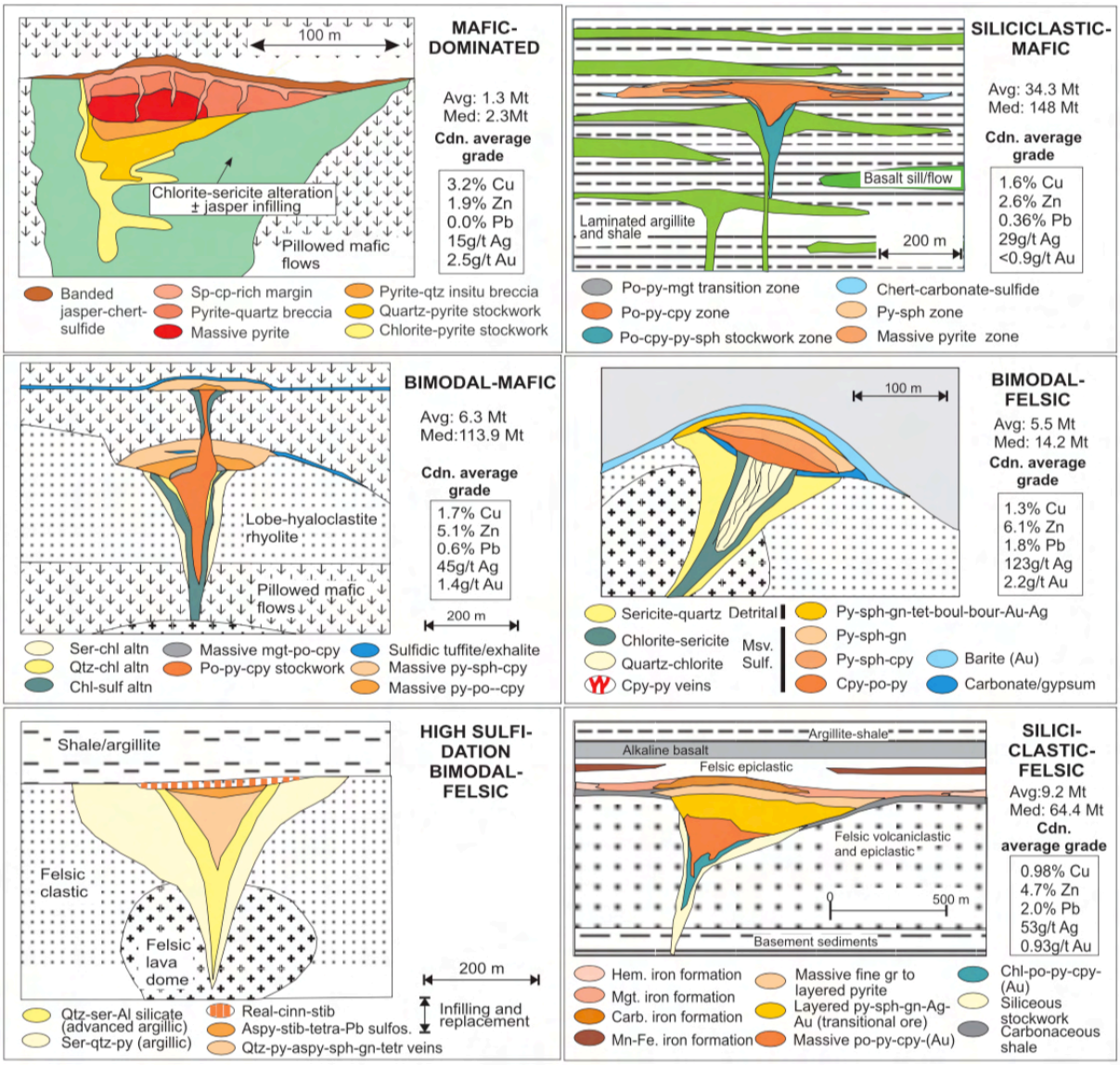


Figure 16: Visualization of the different types of VMS deposits based on the classification scheme proposed by Barrie and Hannington (1999) with the addition of "High sulfidation bimodal felsic". Figure from Galley et al. (2007).

### 4.1.3 Hydrothermal fluids and associated mineral assemblages

Ore-bearing fluids in the VMS system are predominantly composed of evolved seawater occasionally mixed with small amounts of volatiles of magmatic origin (Hannington et al., 2005). Fluid composition will vary between the different volcanic and tectonic settings and can involve several generations and pathways over the evolution of the system (Hannington et al., 2005). The driver of the hydrothermal circulation is the geothermal gradient that promotes subseafloor circulation of seawater (Galley et al., 2007). Sulfur derived from seawater is the main contributor of reduced sulfur to the system as magmatic $SO_4$ and $H_2S$ are thought to only be minor components (Shanks III et al., 1981). Bischoff and Dickson (1975) also showed that when the fluids reach the reaction zone, Mg is removed, producing an acidic solution which are enriched in metal leaching from the host rocks while in some deposits metals can also be

attributed from a magmatic source (Franklin et al., 2005). According to Franklin et al. (2005) metal content in VMS deposits is controlled by several factors including temperature, pH of fluids in the reaction zone, adiabatic cooling during the ascent of fluids, sub-seafloor mixing and zone refining. Fluids eventually rise towards the ocean floor where the metals are precipitated either within the stringer zone/stockworks, mound/chimney or as exhalative metalliferous sediments.

As a result of the fluid/rock interaction, VMS deposits are often associated with haloes of hydrothermally altered rocks (Figure 16A), and vertically below the deposit the alteration can extend several hundred meters along the stockworks and veins (Galley et al., 2007). The extent of the alteration in the low temperature (<50-180 °C) (Patten et al., 2016) section of the deposit is controlled by the intensity of the alteration, morphology and the distribution of fractures and breccias (Patten et al., 2016). In the hydrothermal domain, plutonic rocks and sheeted dykes are altered by high-temperature reduced fluids (Alt et al., 2010). The mineral assemblages in the hydrothermal domain resembles greenschist facies conditions are typically composed of chlorite, actinolite, albite, titanite and pyrite (Alt et al., 2010). Alteration zonation is recognized in proximity to the sulfide mound and is detailed by Galley et al. (2007) and visualized in Figure 16A: The stock-works commonly host an alteration assemblage of Fe-chlorite - quartz - sulfide ± sericite ± talc (Figure16A, Zone 2) that becomes gradually enriched in quartz and sulfides (Zone 1) towards the massive sulfide mound. Further out from the stockworks is a wider zone (Zone 3) of Fe-Mg-chlorite, sericite and phengite. Outermost (Zone 4) sericite, phengite, Mg-chlorite ± albite ± carbonate and ± barite makes out the alteration assemblage. As a result investigations into hydrothermal alternation related to ore deposits can be useful as a tool for mineral exploration both to determine the proximity to the deposit as well as the mineralization type (Mathieu, 2018).

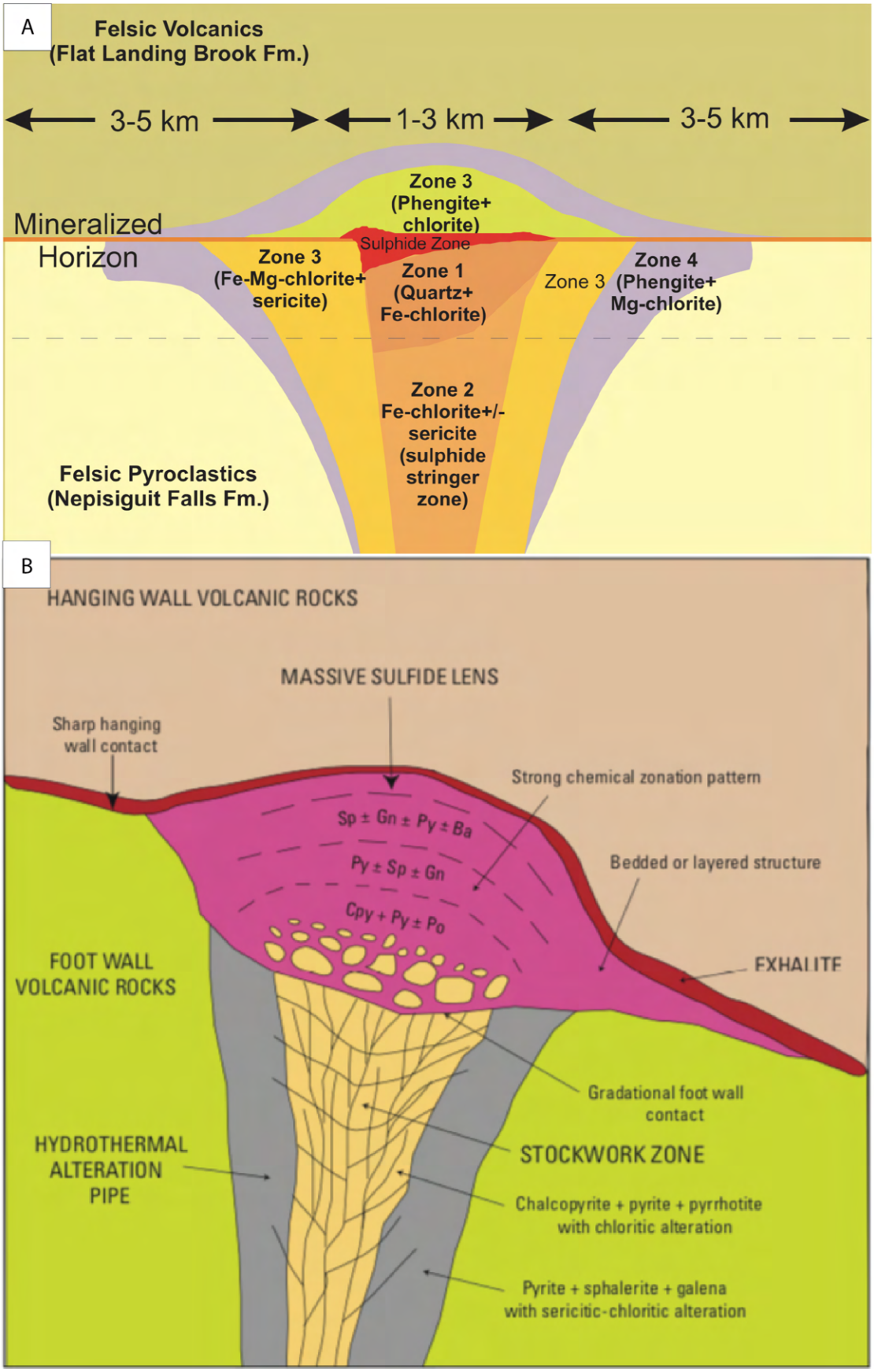


Figure 16: A) A section through a proximal VMS alteration system based the Bathurst mining camp metamorphosed to greenschist facies. From Goodfellow et al. (2003) B) Illustration of an idealized base metal zonation in VMS deposits. From Koski (2012), modified after Lydon (1994)

The most common sulfide minerals in VMS deposits are the iron sulfides pyrite ($FeS_2$) and pyrrhotite ($Fe_{(1-x)}S$) together with less abundant chalcopyrite ($CuFeS_2$) and sphalerite ((Zn,Fe)S). The latter two occur in varying amounts and in some deposits concentrations exceeds that of the iron sulfides (Koski, 2012). Other ore and gangue minerals are also present together with Au, Ag and variable amounts of incorporated trace elements (Hannington et al., 1991). Metals precipitating out of solution at lower temperatures may be remobilized as a result of changes in the chemical composition and temperature of the fluid. This process can form a zonation of the different metals in the deposit (Koski, 2012). The zonation model proposes a copper-iron rich core of chalcopyrite and pyrrhotite and an iron-lead-zinc rich outer zone off galena and sphalerite (Figure 16B). Also, to be noted is that this represents the ideal zonation of the VMS system and that the real-world application to deposits can vary as metal composition can be affected by supergene or metamorphic processes (Galley et al., 2007). Often found in association with the sulfide mound or deposited distally is the exhalative sediments. These are derived from the hydrothermal plume and deposited on the seafloor both proximal and distally to the chimney (Spry et al., 2000). Exhalatives can encompass a variety of compositions with the more common being Fe-silicates (jasper) and pyrite/pyrrhotite rich massive layered sulfides (Vasskis) (Spry et al., 2000).

### 4.1.2 Modern seafloor massive sulfide (SMS) systems and their importance for understanding ancient VMS deposits

The relatively recent discovery of active seafloor hydrothermal systems has advanced the understanding of ancient land based deposits (Barrie and Hannington, 1999). Modern systems are located along mid-ocean ridges (65%), back-arc basins (22%), volcanic-arcs (12%) and intraplate volcanoes (1%) (Baker and German, 2004; Hannington et al., 2011). However, these estimations are based on currently available data and are constantly evolving with new discoveries of active vent fields (Hannington et al., 2005). Although mid-ocean ridges appear to host the majority of modern systems, they are not as commonly represented in the geological record as the ocean floor is constantly recycled through subduction of the oceanic crust (Hannington et al., 2011). However, modern systems functions well as analogs for ancient deposits which are mainly hosted in associations with ophiolite fragments formed in back-arc basin environments in association to supra-subduction zones (Hannington et al., 2005). Using modern systems as analogs to the previously discussed classification by Barrie and Hannington the mafic type ophiolite hosted deposits resembles the modern black smoker along mid-ocean ridges with examples like the TAG mound and the Loki`s Castle. The deposits with more

evolved host rock composition (bimodal-mafic and bimodal-felsic) are similar to the deposits forming in back-arc rifts and within the calderas of submarine arc volcanoes. An example of this setting is the Tonga-Kermadec arc off New Zealand (de Ronde et al., 2001). Modern analogs for mafic siliciclastic type deposits can be found in the Atlantis II deep in the Red Sea and in the Guaymas Basin of the Gulf of California (Barrie and Hannington, 1999).

## 4.2 Sulfur isotope systematics in hydrothermal ore deposits

### 4.2.1 Isotope geochemistry

Isotopes are atoms with the same number of protons but different numbers of neutrons in their nuclei. Isotopes can be stable (stable isotopes) or they can decay over time (radioactive isotopes). Both types of isotopes have a broad application in different types of geological studies. In general, radioactive isotopes can be applied in geochronology, provenance studies and chemical stratigraphy (Banner, 2004). Stable isotopes does not decay over time, and fractionation of heavy and light isotopes of same element can be used to trace different types of physical and chemical processes (O'Neil, 1986). Stable isotope compositions are reported as the (δ) notation in parts per mill (‰) (Seal, 2006), expressing enrichment or depletion of the heavy isotope relative to the relevant standard.

### 4.2.3 Isotopic fractionation

Different isotopes of an element have different mass and as a result exhibit slightly different physical and chemical behavior which can lead to relative portioning of light and heavy isotopes. This process is separated into equilibrium and kinetically controlled fractionation (Seal, 2006). Kinetic fractionation is irreversible and unidirectional and is affected by processes such as evaporation, diffusion and dissociation. Evaporation and diffusion causes fractionation as a result of different mass between the isotopes (O'Neil, 1986) while dissociation is dependent on that heavier isotopes have bonds that are harder to break than lighter isotopes (O'Neil, 1986). This will lead to an enrichment of the heavier isotope relative to the lighter counterpart. Equilibrium fractionation is on the other hand reversible and fractionates due to mass dependent fractionation as heavier isotopes are more stable (Seal, 2006). Fractionation is given as a fractionation factor which is defined by the light and heavy isotopes and their relative abundance against a given standard which are further detailed in the following section.

### 4.2.2 The sulfur isotopic system

Sulfur is the 14th most abundant element in the Earth's crust (Seal, 2006). Five sulfur isotopes occur naturally ($^{32}S$, $^{33}S$, $^{34}S$, $^{35}S$ and $^{36}S$) with four being stable isotopes and one radiogenic. The radioactive $^{35}S$ undergoes beta-decay with a half-life of 87 days, making it unsuitable for use in tracing geological processes (Seal, 2006). The four stable isotopes have set abundances within the bulk earth at $^{32}S$ (95.02%), $^{33}S$ (0.75%), $^{34}S$ (4.21%) and $^{36}S$ (0.02%) (Macnamara and Thode, 1950). In geochemistry and terrestrial studies, the most common ratio between isotopes used is $^{34}S/^{32}S$ as it is the two most abundant sulfur isotopes and as mass governs their relative mass towards each other. As an example, this will make the fractionation between $^{34}S/^{32}S$ twice as large as $^{33}S/^{32}S$ (Seal, 2006). The standard used as a reference for sulfur isotopes is the Vienna Canyon Diablo Troilite (VCDT) representing a isotopic value of $\delta^{34}S = 0.0‰$ (Krouse and Coplen, 1997). For fractionation of a given sample the delta (δ) notation for $^{34}S/^{32}S$ is expressed in ‰ and defined as (Seal, 2006):

$$\delta^{34}S = \left( \frac{\left(^{34}S/^{32}S\right)_{sample} - \left(^{34}S/^{32}S\right)_{reference}}{\left(^{34}S/^{32}S\right)_{reference}} \right) \times 1000$$

### 4.2.4 Sulfur stable isotopes in VMS deposits

Sulfur isotopes can be an effective tool for determination of the sulfur origin in ore deposits (Seal, 2006), and VMS deposits can have a wide range of values. As an example magmatic sulfur is assumed to represent $\delta^{34}S$ values of 0 to +2 ‰, while bacterial reduction of seawater sulfate generates profoundly negative values (Seal, 2006). The sulfur can originate from several sources with seawater, host rocks and leaching from bacterial sulfur reduction being considered as the main reservoirs (Seal, 2006). Seawater $\delta^{34}S$ values have evolved in the ocean over geological time adding complexity to ancient VMS systems along with possible anoxic bottom waters (Seal, 2006). As a result, $\delta^{34}S$ values for the Archean hydrothermal deposits are relatively uniform (−2 to +2‰) as the sea was not differentiated at this point. However, during and after the Proterozoic the ocean departs from these values exhibiting greater variation (Sharman et al., 2015). Currently the oceans display a $\delta^{34}S$ value of dissolved sulfate at +21.0 ± 0.2‰ (Rees et al., 1978). This is important as the most abundant source of sulfur in seafloor hydrothermal systems is seawater sulfate through equilibrium thermochemical reduction of

seawater. When the fluids temperatures reach 150 °C (Sleep, 1991) anhydrite will start to precipitate, and as a result of retrograde solubility and higher calcium levels most of sulfate is removed from the original seawater. As the heavier $^{34}S$ isotope prefers the sulfate this will lower the $\delta^{34}S$ values of the remaining fluids from the original seawater (Shanks III, 2001). The fluids then enter the high temperature reaction zone, and close to the heat source sulfate is reduced and gets mixed with $H_2S$ hydrolyzed from hydrothermal reactions with ferrous minerals and sulfides (Shanks III, 2001). As the seafloor hydrothermal systems are often heterogeneous, sulfur can also be added from other sources which can affect the $\delta^{34}S$ values (Seal, 2006). Examples of other sources of sulfur is magmatic sulfur or sediment covers that have been reworked by sulfur reducing bacteria (Shanks III, 2001). Variations in $f_{o2}$ and pH in hydrothermal fluids can impact fractionation together with temperature and sulfur isotopic composition (Ohmoto, 1972). As an example, Ohmoto and Lasaga (1982) recognized that the kinetic exchange between aqueous sulfate and sulfide are important at elevated temperatures. The pH affects the exchange between dissolved $SO_4$ and $H_2S$, with increasing rates below 3 pH, constant rates between 4-7 pH and decreasing rates with higher pH (Ohmoto and Lasaga, 1982).

## 4.3 Mineral chemistry of ore minerals as a tool in exploration geochemistry

As undiscovered mineral deposits are often partly or completely buried within rocks, discovering new deposits with traditional exploration methods have become more difficult. This comes as a consequence of that most deposits visible on the surface have already been discovered. However, at several locations sediments and vegetation might hide unknown deposits of economic value. Therefore, using trace and minor element signatures within ore minerals deposited in sediments can be a new way of discovering areas of interest. Making this possible is the often internal systematic element variations within a mineral deposit system (Cook et al., 2016). By using LA-ICP-MS as a tool for analyzing trace and minor elements concentration distributed in minerals the variations can become markers for different parts of the mineral depositing systems (Cook et al., 2016). As an example, Dehnavi et al. (2018) used pyrite originating from VMS deposits to detail the internal variations in mobile element distribution both due to micro- and nano-scale and substitution of elements. This can possibly be used as an indicator combined with traditional exploration tools to locate specific environments in deposits with related alternation haloes (Dehnavi et al., 2018). The method has also been considered on deposit scale by Makvandi et al. (2016), using magnetite to separate between deposits, as well as defining in which environment the magnetite formed. Along with

the previously mentioned applications, Duran et al. (2019) determines the possible presence and difference in ore genesis by using sulfide minerals within tills. Using LA-ICP-MS trace element data from the sulfides and comparing known values for magmatic and hydrothermal deposits and comparing the results to glacial movement they have been able to make out target areas for exploration. This is based on fluid mobile trace elements in chalcopyrite and pyrite. These elements are chosen on the basis of their abundance in the Earth's crust, using ternary diagrams to separate between elements enriched or depleted in the various systems (Duran et al., 2019). This collection of data regarding trace element composition determines not only where the mineral might originate from within the system, but also which deposit types might be expected in a given area.

# 5 Samples and analytical methods

## 5.1 Field work and sample collection

The sampling campaign was conducted on the islands of Bømlo, Lindøya and Stord (Figure 4. 5) in the summer of 2020. In total, 21 hand specimens were selected for further analyses (Table 1).

### 5.1.2 Sample locations and investigative methods

All locations of the sampled rocks are listed within Table 1 together with analytical methods performed on each sample. Transmission light microscopy (TLM) was applied for determination of textural and mineralogical characteristics of selected host rock samples. Main and trace element compositions of the host rock samples were used for their geotectonic classification. Mineralogy and textures of ore samples have been studied by a combination of TLM, reflected light microscopy (RLM) and scanning electron microscopy (SEM). Sulfur isotope composition of sulfides give an insight into the origin of sulfur in the studied deposits. Trace element analyses of individual sulfide minerals are obtained by the Laser Ablation - Inductively Coupled Plasma - Mass Spectrometry (LA-ICP-MS) method. Ore grade analysis was conducted to quantify the metal content in mineralized samples.

Table 1: Overview over all samples collected for analyses together with investigative methods. Information regarding the analytical methods and sample preparation are given in Chapter 3. Abbreviations: TLM – Transmission light microscopy, RLM – Reflected light Microscopy, SEM-EDS – Scanning Electron Microscope - Energy Dispersive X-ray Spectroscopy.

| **Locality** | **Sample** | **Sampling location** | **Investigative methods** | | | | | | |
|---|---|---|---|---|---|---|---|---|---|
| | | | TLM | RLM | Ore grade | Lithogeochemistry | LA-ICP-MS | SEM-EDS | Sulfur isotopes |
| **Alvsvågen** | **20ALS7B** | 59.461646 N, 5.095295 E | x | | | x | | | |
| | **20ALS7S1** | 59.461662 N, 5.095314 E | x | | x | x | | | x |
| | **20ALS7S3** | 59.461662 N, 5.095314 E | | | x | | | | x |
| | **20ALS7C** | 59.461662 N, 5.095314 E | x | | | | | | |
| | **20ALS6D1** | 59.461865 N, 5.094590 E | x | x | x | | | | x |
| | **20ALS6D2** | 59.461865 N, 5.094590 E | x | | | | | | |
| | **20ALS3S1** | 59.469160 N, 5.095139 E | | x | x | | x | x | x |
| | **20ALS4E** | 59.461156 N, 5.094521 E | | x | | | x | x | x |
| | **20ALS4F** | 59.461156 N, 5.094521 E | | x | x | | | x | x |
| | **20ALS11** | 59.469160 N, 5.095139 E | | x | | x | | | |
| | **20ALS9** | 59.767992 N, 5.158297 E | x | | | x | | | |
| **Lindøya** | **20LIND4B** | 59.452175 N, 5.132214 E | | x | x | | x | x | x |
| | **20LIND-H** | 59.754835 N, 5.224530 E | x | x | x | | x | | x |
| | **20LIND2** | 59.452099 N, 5.132319 E | x | | | | | | |
| | **20LIND5** | 59.452176 N, 5.132172 E | x | | | x | | | |
| **Litlabø** | **19LIT2** | Sampled from within mine | | x | x | | x | x | x |
| | **19LIT3** | Sampled from within mine | | x | x | | | x | x |
| | **20LIT3** | 59.473465 N, 5.251616 E | x | | | | | | |
| | **20LIT7** | 59.473487 N, 5.251773 E | | x | | | | x | |
| | **20LIT8** | 59.473465 N, 5.251616 E | x | | | | | | |

## 5.2 Thin/thick section preparation

Representative parts of the selected samples were cut by a diamond saw into small blocks suitable for thin and/or thick section preparation. Thick sections were prepared for the RLM, SEM and LA-ICP-MS analyses. Polished thick sections were prepared at a thickness of 500 μm and the polished thin sections at 30 μm. In total 10 polished thick sections and 11 polished thin sections were prepared.

### 5.2.1 TLM and RLM microscopy:

For microscopic investigations the microscope Nikon Eclipse LV100POL was used and for microphotographs the camera Nicon DS – F3 was used in association with the imaging software NIS – Elements BR 5.11.01 64 – bit. Transparent minerals were studied under TLM while RLM was used for the opaque and ore minerals.

## 5.3 Scanning Electron Microscope – Energy Dispersive X-ray Spectroscopy

The 500 μm thick sections were introduced to RLM to find representative areas for further analysis of ore minerals, gangue minerals and chlorites. After preparation of the 500 μm thick sections were introduced to the scanning electron microscope for both spot analysis and elemental mapping. The scanning electron microscope used were the ZEISS SUPRA 55VP. Before the analysis all thick sections selected for analysis were coated with carbon. For elemental mapping a resolution of 256x192 were used together with frame time of 20 and 200 frames. The working distance (WD) used during the analysis was 8.5 millimeters. For sulfides and iron oxides the method was mainly qualitative to determine the various mineral phases. For spot analysis of sulfides and iron oxides the method was purely qualitative to determine the various mineral phases.

For chlorite thermometry the measurements of elements in the chlorite grains were conducted with spot analysis measured against standards (Appendix A). The most relevant standards used for chlorite measurements were iron for Fe, corundum for Al, wollastonite for Si and magnesium oxide for Mg. All standards were measured before, during and after analysis as to monitor instrumental drift. The WD used during the analysis was 8.5 mm.

## 5.4 Laser ablation ICP-MS analyses of thick sections

A total of 36 elements was analyzed with LA-ICP-MS from sulfide grains from both the Alvsvågen and Litlabø deposits. 49 spots were analyzed with a total of 36 from Alvsvågen and 13 from Litlabø. For the 36 spots from Alvsvågen 18 were pyrrhotite, 12 chalcopyrite and 6 pyrite. From Litlabø a total of 13 spots were acquired with 12 being pyrite and 1 pyrrhotite. The data collected are listed in in Appendix B.

Trace element analysis of single sulfide grains with a single collector ICP-MS were performed at the Geological Survey of Finland (GTK), using a Nu AttoM SC-ICPMS (Nu Instruments Ltd., Wrexham, UK) and an Analyte 193 Arf laser-ablation system (Photon machines, San Diego, USA). The method used is provided by GTK:

When analyzing the laser was run at a pulse frequency of 5 Hz with a pulse energy of 5 mJ. This was done at a 30 % attenuation to produce an energy flux of 2.5 J / $cm^2$ at the surface of the sample with a 40 mm spot size. For each analysis a 20 second baseline measurement was done, followed by switching on the laser for 40 seconds for signal acquisition. Analyses were made using time resolved analysis (TRA) with continuous acquisition of data for each set of point. Generally following the scheme of primary standard, quality control standard and 10-20 unknowns. For external standardization synthetic pressed nanopellet sulfide standard UQAC FeS-1 was used, and nanopellet sulfide standards FeS-5 and FeS-6 were used as quality control. Measurements were performed on 65 isotopes covering 38 elements at low resolution ($\Delta M/M = 300$), using the fast scanning mode. Reduction of data was handled using the software GLITTER $^{TM}$ (Van Actherbergh, 2001) allowing baseline subtraction and the integration of the signal over a selected time resolve area and the quantification using known concentrations of the external and internal standards.

## 5.3 Trace and main element analysis

### 5.3.1 Sample preparation

All weathered surfaces were removed from the samples by the use of a diamond saw prior to further crushing the sample down to a fragment 0.3 mm fragment size compatible with the agate-ball-mill. The agate-ball-mill was then used to mill the sample into fine powder. The mill was run for 10 minutes at 400 rounds per minute. To ensure proper results, the program was run three times for each sample. The powder was weighed in at approximately 2-4 grams and heated in a furnace at 1000 °C for 4 hours removing all volatiles and organic material from the sample. Afterwards the powder was weighed again, and the loss of ignition was calculated (LOI%).

### 5.3.2 Main element analysis

#### 5.3.2.1 Glass tablet preparation

An aliquot of 0.960 g of the rock powder was mixed with 6.720 g of dried flux (Spectromelt A-10, Lithium Teatraborate). The mix was then placed in a gold/platinum crucible which was placed in a rotating furnace. The molten mass was then poured into another platinum crucible which cools the sample and gives it a tablet form. This process also ensures that the mix of compounds within the sample gets homogenously distributed within the glass tablet. Six samples for X-ray fluorescence were prepared.

#### 5.3.2.2 X-ray fluorescence

Silica content within the samples were analyzed using X-ray fluorescence analysis (XRF). The elemental concentration is given and reported as oxides and are reported as weight percent (wt%). The samples were analyzed using an AXS S4 Pioneer XRF. The results were measured against two standards, the GSP-1 (Silver Plume Granodiorite) and BCR-2 (Colombia River Basalt).

### 5.3.3 Trace element analysis

#### 5.3.3.1 Sample preparation

0.10 grams of the sample prepared previously were weighed inn accurately in 25 ml PFA savillex beakers. Afterwards the sample was digested in 3 ml of concentrated HF and warmed at 135 °C on a heating plate for 48 hours. During this, HF supernatant was removed from the

sample through evaporation. Afterwards residues of fluoride were hydrolyzed in a weak solution of $HNO_3$ on the heating plate below sub-boiling point and evaporated to dryness and most samples were completely dissolved using this method. The result of this method is nitrate salt which is again dissolved in ca 2 ml 2N $HNO_3$ prior to dilution with 2% $HNO_3$ in a volumetric flask with a volume of 50 ml. Occurring in some of the samples were still undissolved particles, which was ascribed to be transition metal compounds, mostly $MnO_2$. To dissolve these particles about 1 ml of Aqua Regia (3:1 Concentrated HCl) were used on the heating plate. To function as an internal standard indium was added to the sample.

#### 5.3.3.2 Inductively Coupled Plasma - Mass Spectrometry (ICP-MS)

For analysis of trace elements, a Thermo Scientific Element XR$^{TM}$ Inductively Coupled Plasma Mass Spectrometer were used. The elements covered within the analysis were rare earth elements (REE) and some selected trace elements. As for standard reference material BCR2 was analyzed before and after samples together with SPS-SW2 in between samples. Two blanks were used under the analysis with the first containing only $HNO_3$, while the second blank was prepared in the same manner as the samples.

#### 5.3.3.3 Inductively Coupled Plasma - Optical Emission Spectrometry (ICP-OES/AES)

Using a Thermo Scientific ICap 7600 Inductively Coupled Plasma Atomic Emission Spectrometer (ICP-AES) the samples have been analyzed for a range of major and trace elements. External calibration curves are used for quantification (multi element standard solutions prepared from certified single element solutions from Spectrapure) while Sc was used for internal standard. All samples are diluted with 2 % w/v $HNO_3$ to an acceptable level. The quality of the analysis is assured with the standard USGS CRM BCR2 (Columbia river basalts). The standard is prepared in the same way as the sample from the digestion step in preparation. To monitor performance and have direct control over the calibration curves during the analysis CRM SPS-SW-2 (Spectrapure Standards AS), synthetic water was analyzed through the runs.

## 5.4 Sulfur isotopes

From the selected samples all different sulfide minerals present were identified, and a drill was used to extract the selected mineral. These were again marked and stored within containers for further transport and analysis. All of the analysis was performed by the Institute of Earth Surface Dynamics of Lausanne in Switzerland. All measurements were done with an on-line EA-IRMS system. This was again coupled together with a Carlo Erba 1108 Elemental Analyzer (EA) with a continuous helium flow interface to the Thermoquest/Finnigan Mat Delta S IRMS. All samples were oxidized by the EA which has a stream of helium and oxygen using flash combustion in a single oxidation/reduction quartz tube. The tube was filled with oxidizing tungsten trioxide and reducing elemental copper at a temperature of 1030 °C. For removing water anhydrous magnesium perchlorate were used with the gases entering a chromatographic column (Poropak QS) to separate the $SO_2$ which analyses the isotopes by using IRMS (Giesemann et al., 1994). Measured values of sulfur isotopes are given in the δ-notation and relative to the V-CDT standard. The laboratory assured reproducibility with replicate analysis with given standards (natural pyrite +6.1 ‰, synthetic mercury sulfide, +15.5 ‰, barium sulfate, +12.5 ‰ $\delta^{34}S$) to be better than 0.2 ‰.

## 5.6 Ore grade analysis

The ore grade analysis was performed by Bureau Veritas Mineral Laboratories in Canada. The methods used will be given as procedure codes from the lab. All samples were crushed down with the PRP90-250 procedure code. Gold content in the samples were measured using FA330-Au procedure code while all other elements were measured by the procedure code MA370.

## 5.7 Chlorite thermometry:

From the SEM-EDS measurements of chlorites, a chlorite thermometer by Jowett (2021) was used for temperature calculations. The thermometer is based upon previous work by Cathelineau (1988) with modifications from Kranidiotis and MacLean (1987) as base. From SEM-EDS the values were recalculated to oxides and 10 measurements were used for further calculations. The temperature calculations are listed in Appendix A.

# Chapter 6 Results

## 6.1 Petrography of host rock and ore mineralization

### 6.1.1 The Alvsvågen area

#### 6.1.1.1 Barren layered gabbro

The samples 20ALS9 and 20ALS10C represent the layered gabbro of the Lykling Ophiolite Complex in the Alvsvågen area. The layered gabbro (sample 20ALS9) has been sampled out of the mineralization area and it is barren. The barren gabbro appears as grey to greenish in the field and shows occasional layering (Figure 19A, C). The main mineral phases in the layered barren gabbro (20ALS9) are amphibole (~40 vol.%), saussurite (~40 vol.%) and chlorite (~20 vol.%) indicating that the gabbro was strongly affected by the regional metamorphic overprint (Figures 3B, C). Minor amounts of plagioclase (<5%) are observed (Figure 19C) as most grains are replaced by saussurite. The amphiboles are often distinguished from the chlorite by clear 60-120° cleavage and the grains range in size from 400 to 600 μm (Figure 19B, C). Chlorite is somewhat less abundant and forms needle-like aggregates with some examples of perfect cleavage (Figure 19B).

#### 6.1.1.2 Mineralization hosted by gabbro

The slightly mineralized gabbro (sample 20ALS10C; Figure 19D) exhibit some variation in mineralogical composition compared to the barren layered gabbro (sample 20ALS9). The main mineral phases are amphibole (~20 vol.%) and chlorite (~30 vol.%) within a matrix of plagioclase and quartz (~30 vol.%) (Figure 19E, F). Amphiboles appear as anhederal exhibiting clear cleavage and are found almost exclusively in contact with chlorite, with the latter having both well-developed crystals as well as more needle like features. Plagioclase crystals appear as well developed with euhedral features and exhibits clear lamellar twinning in cross polarized light (Figure 19F). Saussuritization are observed locally within the interior of preserved plagioclase grains (Figure 19F). Quartz are abundant and fill in the space between amphiboles and chlorites together with plagioclase/saussurite (Figure 19E-F).

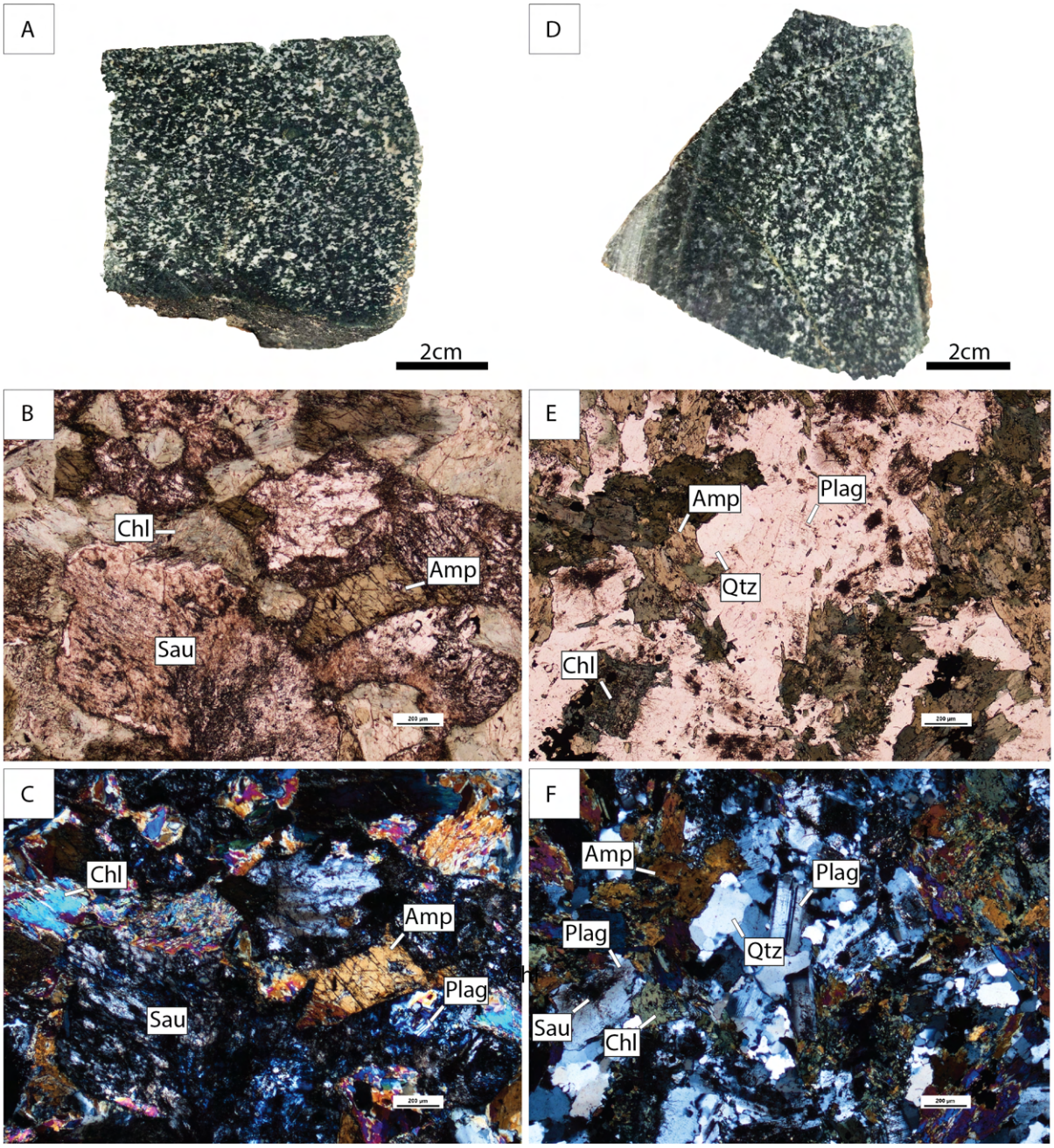


Figure 19: A) Photograph of the Alvsvågen layered gabbro (sample 20ALS9). B) Microphotograph illustrating the mineralogy of the gabbro (sample 20ALS9) in plain polar light. C) Microphotograph of the barren layered gabbro (sample 20ALS9) in cross polar light. D) Photograph of the slightly mineralized gabbro (sample 20ALS10C). E) Microphotograph illustrating the mineralogy of the slightly mineralized gabbro (sample 20ALS10C) in plain polar light. F) Microphotograph of the slightly mineralized gabbro (sample 20ALS10C) in cross polar light. Abbreviations: Amp - Amphibole, Chl – Chlorite, Plag – Plagioclase, Qtz – Quartz, Sau – Saussurite.

The mineralization hosted in the coarse-grained gabbro appears as both sulfide lenses and minor disseminations (Figure 20A). The reflected light microscopy revealed that chalcopyrite and pyrrhotite represent the major sulfide phases (Figure 20B). Rare anhederal grains of pyrite appears in association with pyrrhotite (Figure 20C). Chalcopyrite and pyrrhotite often appear as separated phases with minor inclusions of both phases occurring within the other. Chalcopyrite is mostly found in association with elongated epidote and chlorite grains (Figure

20B) while pyrrhotite forms larger grains which appears as clusters and are highly altered with most grains being either partially or entirely replaced by Fe-oxides and silicates (Figure 20C). Elongated ilmenite grains are confirmed by the Ti content in the SEM element maps and are often observed in association with sulfides, especially in association with lager pyrrhotite grains (Figure 20B, D). The main gangue minerals are epidote, chlorite and minor amounts of quartz.

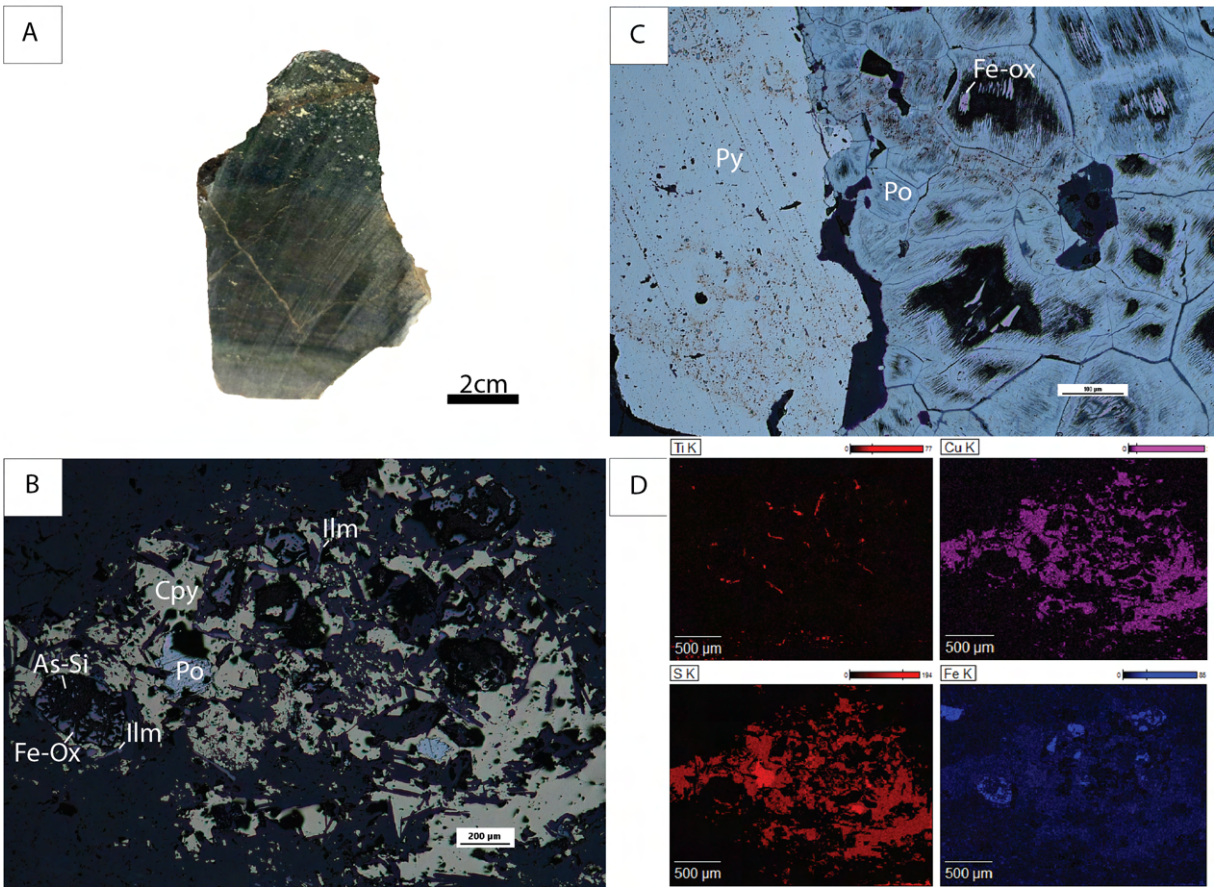


Figure 20: A) Photograph of mineralization hosted within gabbro (sample 20ALS4F). B) Microphotograph of the gabbro illustrating the ore mineralogy under reflected light. C) B) Microphotograph illustrating the relation between pyrite and pyrrhotite and weathering of the latter. D) SEM-EDS analysis of the area in (B) showing the element composition of the gangue minerals as well as titanium content which separates ilmenite from other Fe-oxides. Abbreviations: Cpy – Chalcopyrite, Po – Pyrrhotite, Py – Pyrite, Ilm – Ilmenite, Fe-Ox – Iron-oxide, As-Si – Arsenic Silicate.

The micro-gabbro (sample 20ALS7B) was collected in close proximity to the mineralization in the northern shear zone and appears as hydrothermally altered exhibiting a strong greenish color (Figure 21A). A variation in grain size is recognized and disseminated sulfides are observed throughout the entire sample. Under TLM the major mineral phases are determined to be amphibole (~20 vol.%), chlorite (~40 vol.%) within a matrix of quartz (~20 vol.%) and plagioclase (~20 vol.%) (Figure 21B, C). Amphiboles are recognized in association with chlorites and clear cleavage is observed within well-developed grains (Figure 21B). Chlorite is the main mineral phase in the gabbro with a strong greenish color in plain polar light and the grains appear as well developed. Some variation is recognized in regard to birefringence colors under cross polarized light, displaying variation between high blue and darker orange color (Figure 21C). This might indicate that some of the pre-metamorphic minerals have been preserved and are not fully altered throughout the section. The matrix is mainly composed of quartz and plagioclase (Figure 21B, C).

Weakly mineralized micro-gabbro (sample 20ALS3S2) was sampled from the southern shear zone (Figure 9) (Figure 21D). From TLM the major mineral phases are determined to be chlorite (~40 vol.%), epidote (~30 vol.%) and quartz (~20 vol.%) with minor amounts of saussurite (Figure 21E, F). Grains of chlorite are recognized both as larger well developed and needle-like grains often in association quartz rich veins, and under cross polarized light (Figure 21F) both grey and “Berlin blue” birefringence colors are recognized. Epidote exhibits a brown color in plain polarized light (Figure 21E) and high birefringence colors in cross polarized light (Figure 21F) and in some instances dark rims are recognized around anhederal grains. Quartz is recognized in association with chlorite as well as forming clusters in some areas together with opaque minerals which are recognized as large euhedral sulfide grains. The original gabbroic lithology appears to be completely altered as no original mineral phases have been observed throughout the section.

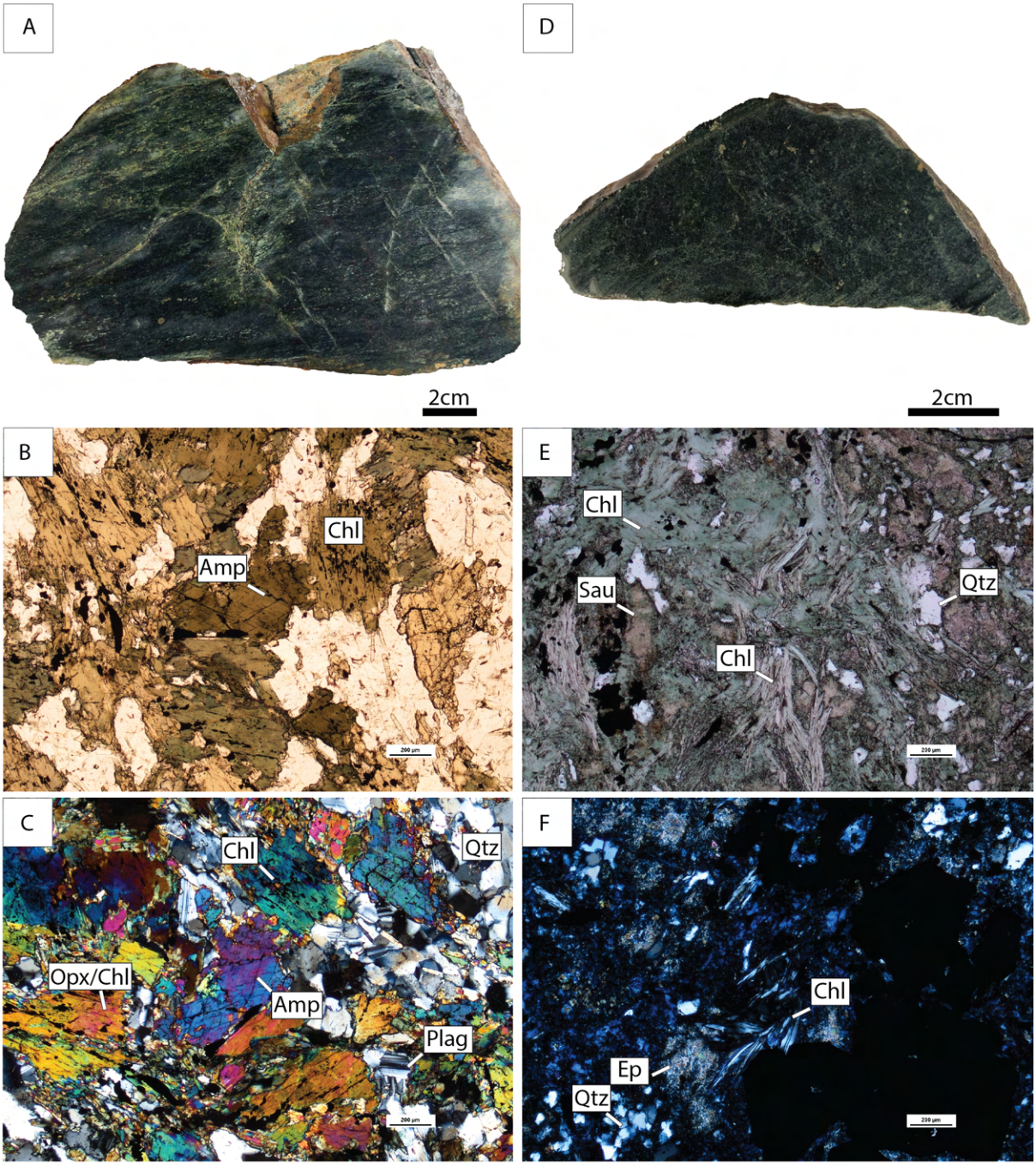


Figure 21: A) Photograph of the mineralization related gabbro in Alvsvågen (sample 20ALS7B). B) Microphotograph of the gabbro (sample 20ALS7B) illustrating the mineralogy in plain polarized light. C) Microphotograph of the gabbro in cross polarized light. D) Photograph of the mineralization related micro-gabbro in Alvsvågen. E) Microphotograph of the micro-gabbro (sample 20ALS3S2) illustrating the mineralogy in plain polarized light. F) Microphotograph of the micro- gabbro in cross polarized light. Abbreviations: Abbreviations: Amp - Amphibole, Chl – Chlorite, Plag – Plagioclase, Qtz – Quartz.

The mineralization hosted by micro-gabbro (sample 20ALS4E) appear as both disseminations and lenses of primarily chalcopyrite (Figure 22A). Chalcopyrite (~70 vol.%) and pyrrhotite (~30 vol.%) are recognized from RLM as the main sulfide phases. The former is concentrated within the lens with minor pyrrhotite appearing as inclusions (Figure 22B, C). Pyrrhotite appears as more disseminated in the matrix with minor amounts of associated chalcopyrite. From the SEM elemental maps, the main element in the lens is copper (Figure 22E) with the

areas rich in iron and lacking in copper recognized as pyrrhotite. Various amounts of titanite with exsolution lamella are observed with rare minor chalcopyrite grains as inclusions (Figure 22C). The gangue mineralogy is primarily comprised of larger quartz crystals as is recognized in the silica content from the elemental map (Figure 22E). Magnesium rich and silica poor areas (Figure 22E) are interpreted to represent chlorite with epidote appearing as elongated grains in close association with sulfides (Figure 22D).

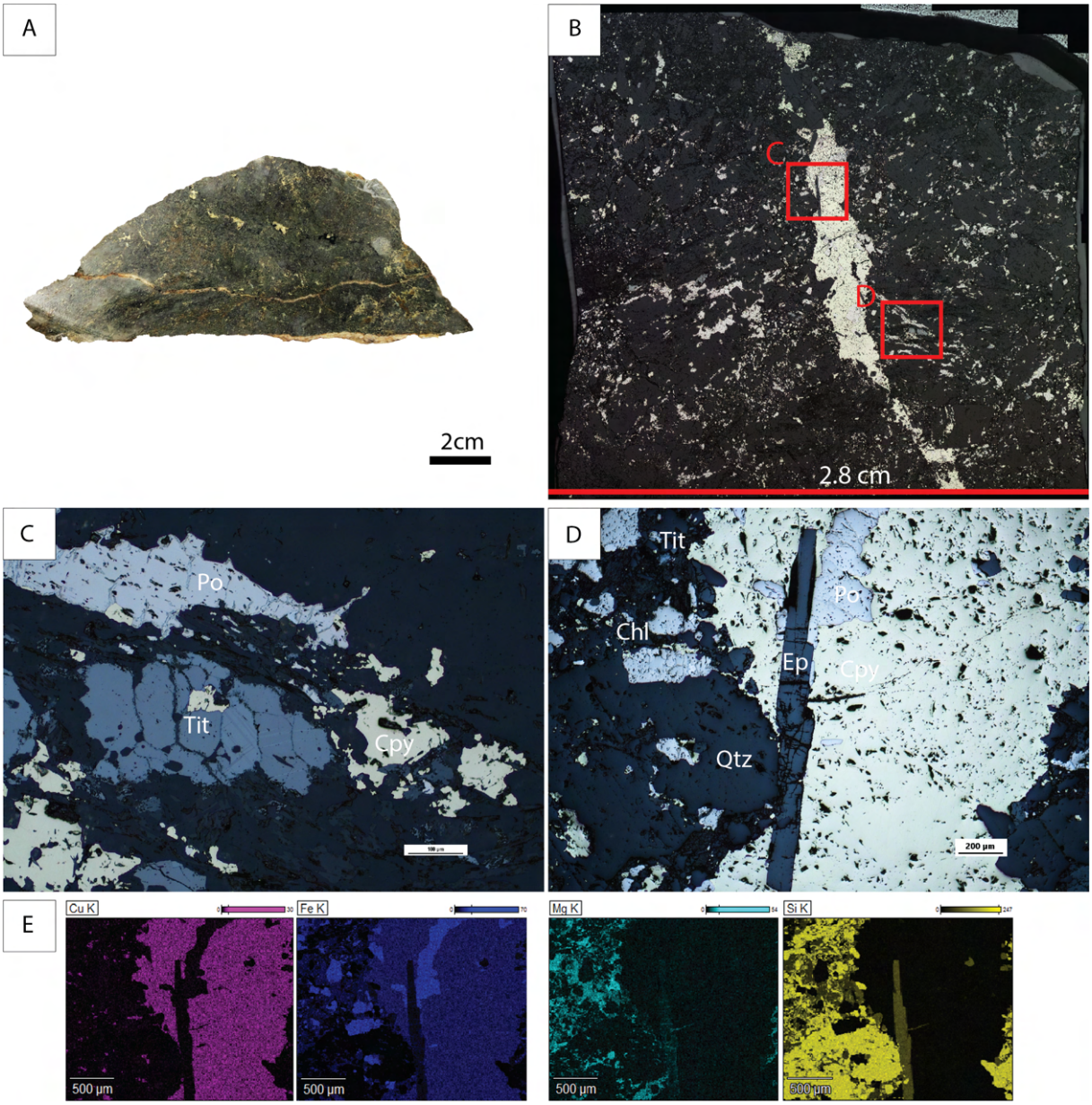


Figure 22: A) Photograph of mineralization hosted within the micro-gabbro (sample 20ALS4E). B) Mosaic of the thin section representing the micro-gabbro with the close-up images marked within by the number figure. C) Microphotograph of the micro-gabbroic sample illustrating the ore mineralogy under reflected light. Various minerals are marked with magnetite exhibiting isotropic features containing a chalcopyrite inclusion. D) Microphotograph of the micro-gabbroic sample illustrating the ore mineralogy under reflected light. Chalcopyrite vein with pyrrhotite inclusions together with an elongated epidote crystal. E) SEM-EDS analysis of the area in (C) showing the element content of various phases. Abbreviations: Cpy – Chalcopyrite, Po – Pyrrhotite, Py – Pyrite, Sph – Sphalerite, Mt – Magnetite, Ep – Epidote, Qtz – Quartz

6.1.1.3 Mineralization hosted by shear zones

The shear zone in which the mineralization is hosted appears as strongly deformed with clear banding along one plane (Sample 20ALS7C; Figure 23A). Sulfides veins are recognized with euhedral pyrite appearing in some instances. From TLM the main minerals phases of the host rock are chlorite (~20 vol.%), epidote (~10 vol.%) and quartz (~65 vol.%). Chlorite and epidote exhibit sharp contacts towards the quartz with the exception being individual oriented grains located within the quartz matrix (Figure 23B, C). Chlorite appear as needle-like grains with dark birefringence colors under cross polarized light, with some rare exceptions of grey and "Berlin blue" (Figure 23B). Epidote appear almost exclusively in association with chlorite exhibiting high birefringence colors (Figure 23C). Rare epidotes are recognized within the quartz appearing in secondary vein-like structures often cross cutting the orientation of the foliation.

A second sample from the mineralized shear zone (sample 20ALS6D2) exhibits different mineralogical characteristics indicating some internal variation in the ore hosting lithology. In a matrix of quartz, euhedral plagioclases and epidote the latter appear as elongated grains oriented along the foliation exhibiting high birefringence colors in cross polarized light (Figure 23D). Chlorite appear as green in plain polarized light within veins perpendicular on the epidote orientation in association with biotite which are observed exclusively in association with chlorite (Figure 23D). Sulfides are associated with chlorite and epidote and are rarely observed within the quartz (Figure 5B, D).

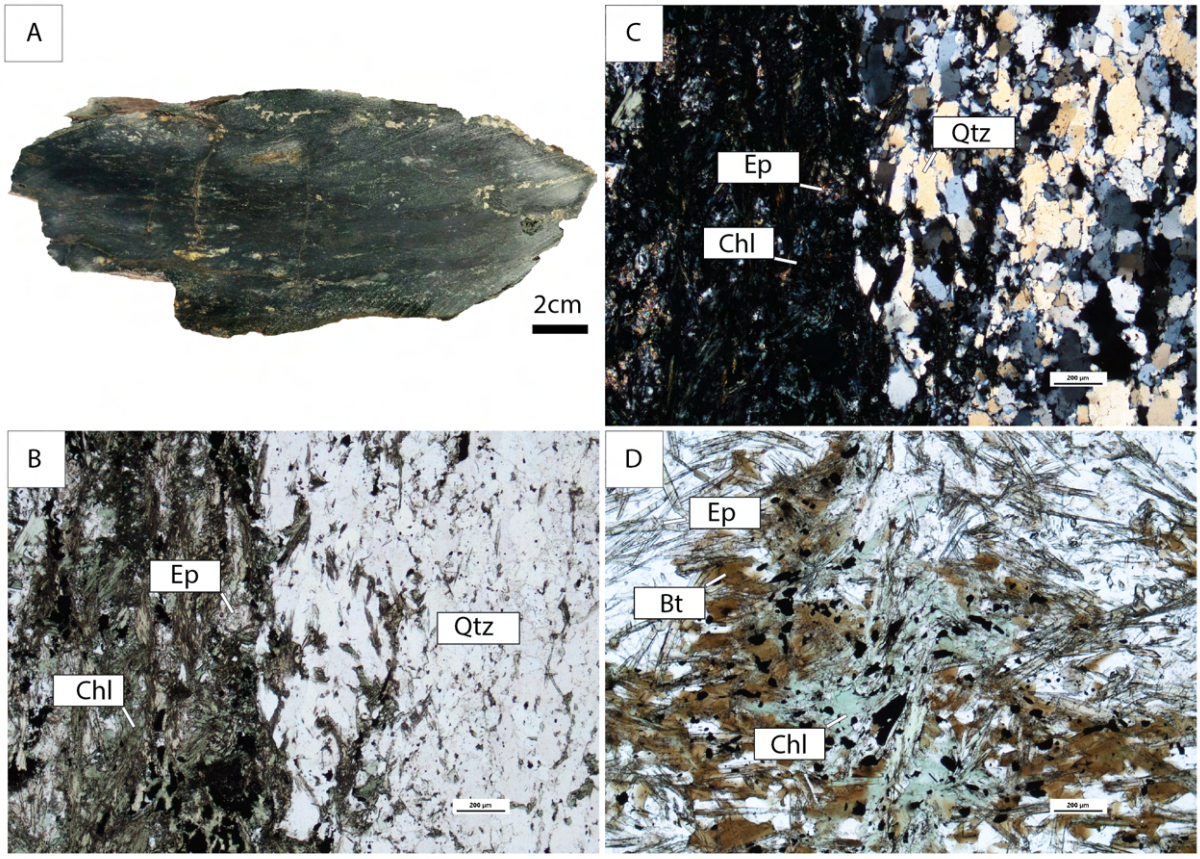


Figure 23: A) Photograph of the shear zone sample (20ALS7C). B) Microphotograph of the shear zone sample illustrating the mineralogy in plain polarized light. C) Microphotograph of the shear zone sample in cross polarized light. D) Microphotograph of the shear zone sample (20ALS6D2) illustrating the mineralogy in plain polarized light. Abbreviations: Chl – Chlorite, Qtz – Quartz, Bt – Biotite, Ep- Epidote.

The main ore minerals recognized in the shear zones are pyrrhotite and chalcopyrite with minor amounts of sphalerite, pyrite and Fe-oxides. Sample 20ALS6D1 (the northern shear zone) is mainly comprised of chalcopyrite and pyrrhotite with minor amounts pyrite (Figure 24A, B). Pyrite grains appear as brecciated with pyrrhotite and minor chalcopyrite filling in the open spaces (Figure 24B). Chalcopyrite do on occasions feature cubanite with and without lamella which are characterized by a darker brown color and rectangular crystal habits (Figure 24B).

Sample 20ALS3S1 (the southern shear zone) exhibits similar mineralogical characteristics but abundant pyrite is recognized (Figure 24C). Pyrrhotite (~60 vol.%) makes up the main mineral phase appearing weathered with veins of recrystallization indicating supergene processes (Figure 24D). Chalcopyrite (~10 vol.%) are observed in association with the latter two phases filling in open spaces or forming rims around the larger pyrites (Figure 24D) together with minor amounts of sphalerite (~1 vol.%) (Figure 24D). The weathering veins in the pyrrhotite exhibits iron/sulfur ratios similar to that of pyrite in SEM-EDS (Figure 24E). It can possibly be inferred from this observation that the pyrrhotite have been altered to pyrite. From the elemental

maps the silica content defines the gangue mineral phases with quartz being recognized by higher contents relative to chlorite and epidote (Figure 24E). The latter appear as elongated well-defined grains in association with the sulfides.

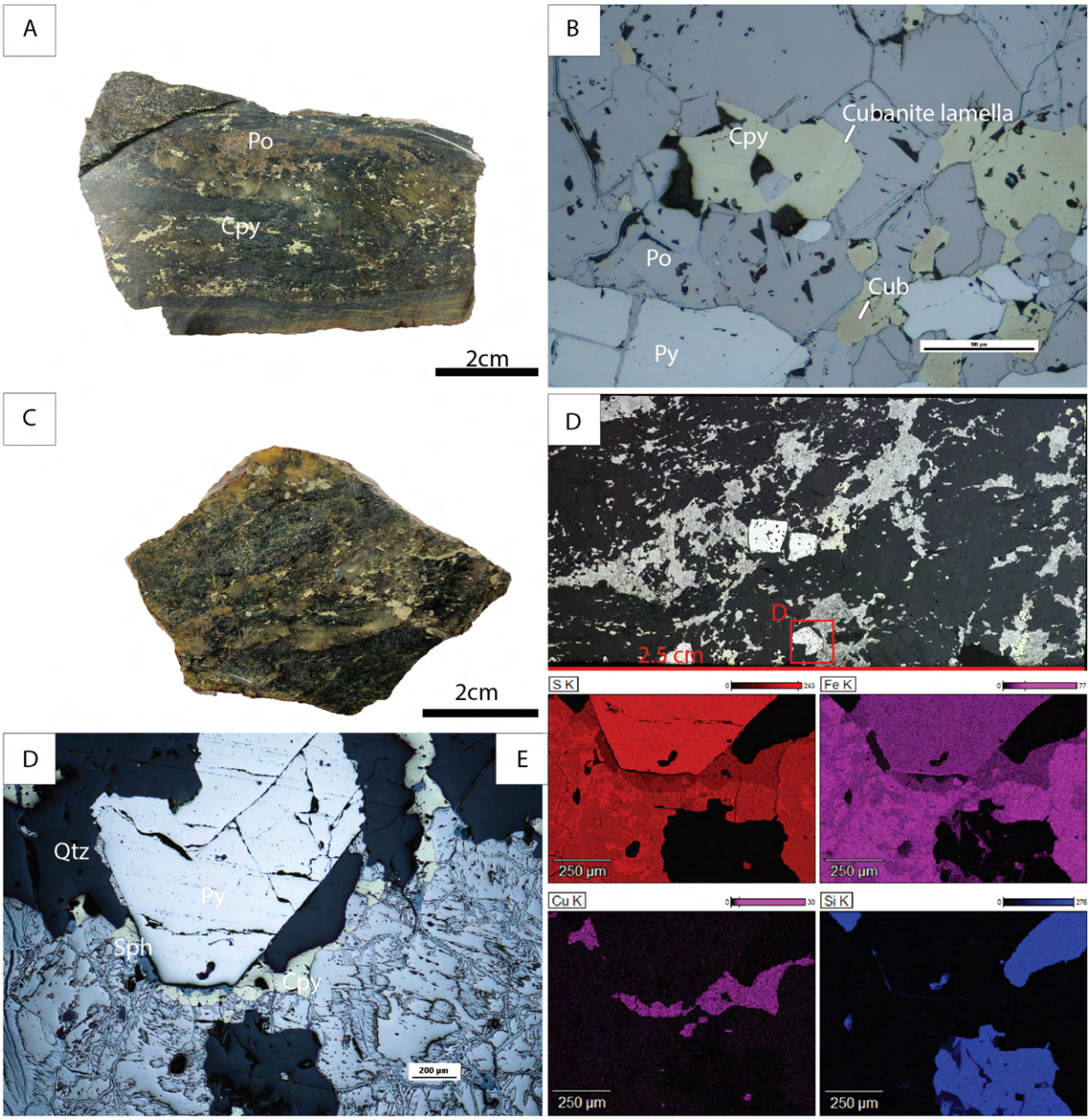


Figure 24: A) Photograph of mineralization hosted within the northern shear zone (sample 20ALS6D1). B) Microphotograph of the northern shear zone (sample 20ALS6D1) illustrating the ore mineralogy under reflected light. Various minerals are marked with cubanite lamella being visible in the chalcopyrite. C) Photograph of mineralization hosted within the southern shear zone (sample 20ALS3S1). D) Mosaic of the thin section representing the shear zone mineralization with the close-up image marked within with reference to the number off the figure. D) Microphotograph of the southern shear zone sample (sample 20ALS6D1) illustrating the ore mineralogy under reflected light. Large euhedral pyrite together with weathered pyrrhotite is clearly visible with smaller amounts of chalcopyrite and sphalerite. E) SEM-EDS element maps of various elements. Abbreviations: Cpy – Chalcopyrite, Po – Pyrrhotite, Py – Pyrite, Sph – Sphalerite, Qtz – Quartz, Cub – Cubanite.

## 6.1.2 The Lindøya area

### 6.1.2.1 Barren micro-gabbro and mineralization hosting basalt

The barren micro-gabbro (sample 20LIND5) sampled in close proximity to the sulfide mineralization has well-developed grains and the main minerals phases are amphiboles (~20 vol.%), chlorite (~50 vol.%) and plagioclase (~30 vol.%) (Figure 25B). Chlorite exhibit strong blue birefringence colors under cross polarized light with the rare exception of orange (Figure 25B). Amphiboles are rare in the sample. The mineralization hosting basalt (sample 20LIND-H; Figure 25C, D) show a similar mineralogical composition as the micro-gabbro with amphiboles appearing as elongated crystals (Figure 25C, D) within a matrix of plagioclase and chlorite that exhibit cleavage on rare occasions.

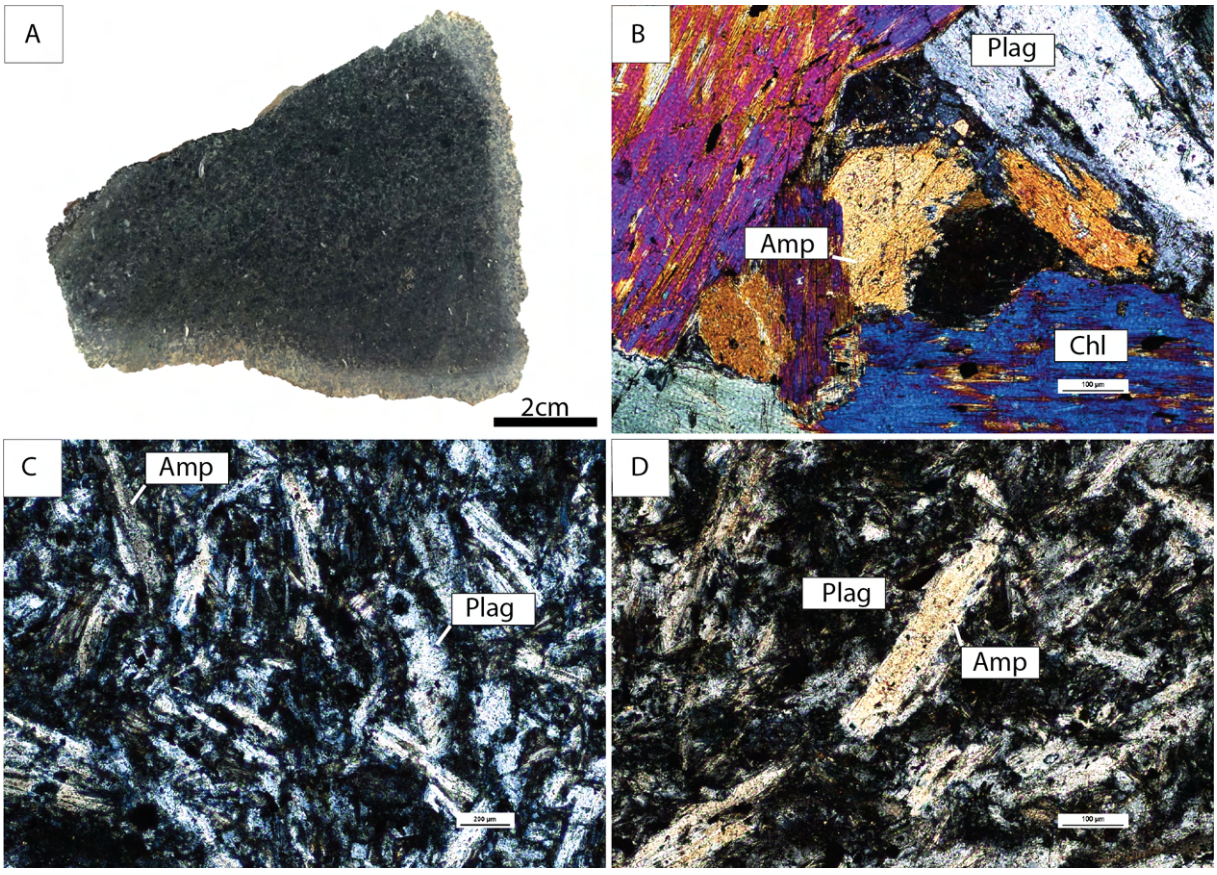


Figure 25: A) Photograph of the micro-gabbro (sample 20LIND5). B) Microphotograph of the micro-gabbroic sample illustrating the mineralogy under cross polarized light. C) Microphotograph of the basalt (sample 20LIND-H) illustrating the mineralogy under plain polarized light. D) Microphotograph of the basaltic (sample 20LIND5) illustrating the mineralogy with emphasis on a large amphibole crystal under cross polarized light. Abbreviations: Amp - Amphibole, Chl – Chlorite, Plag – Plagioclase.

#### 6.1.2.2 Massive bedded and basalt hosted mineralization

Two main types of sulfide mineralization are recognized in the Lindøya area: a massive mineralization (sample 20LIND4B; Figure 26A) and a basalt hosted mineralization (sample 20LIND-H). The massive mineralization show sulfide/silica layering with secondary veins of sulfides cross cutting layering. Some variation in sulfide content is recognized within the sample as the mineralization have areas with more massive mineralization richer in pyrrhotite.

The main sulfide phase in the massive mineralization is pyrite forming euhedral to sub-hederal grains within a matrix of smaller grains of both pyrite and pyrrhotite (Figure 26B, C). Later pyrite rich veins fill minor faults and cracks that crosscut the primary layering. Magnetite and minor amounts of chalcopyrite are also observed within the veins (Figure 26C). The SEM-EDS elemental maps indicate that the matrix is predominantly composed of silica (Figure 26E) with some variation indicating the presence of other faces. high levels of arsenic are also recognized from the matrix which might indicate the presence of an arsenic rich mineral phase.

The basalt hosted mineralization is characterized by a lower sulfide content. Larger euhedral grains of arsenopyrite (~300 μm) and pyrite (~200 μm) are recognized in comparison to pyrrhotite which appears weathered with only the rims being preserved while other grains appears to be completely altered (Figure 26F). Chalcopyrite and sphalerite appear in minor quantities in association with other sulfide phases (Figure 26F, G). The sulfide mineralization is associated with abundant colorization (Figure 26G).

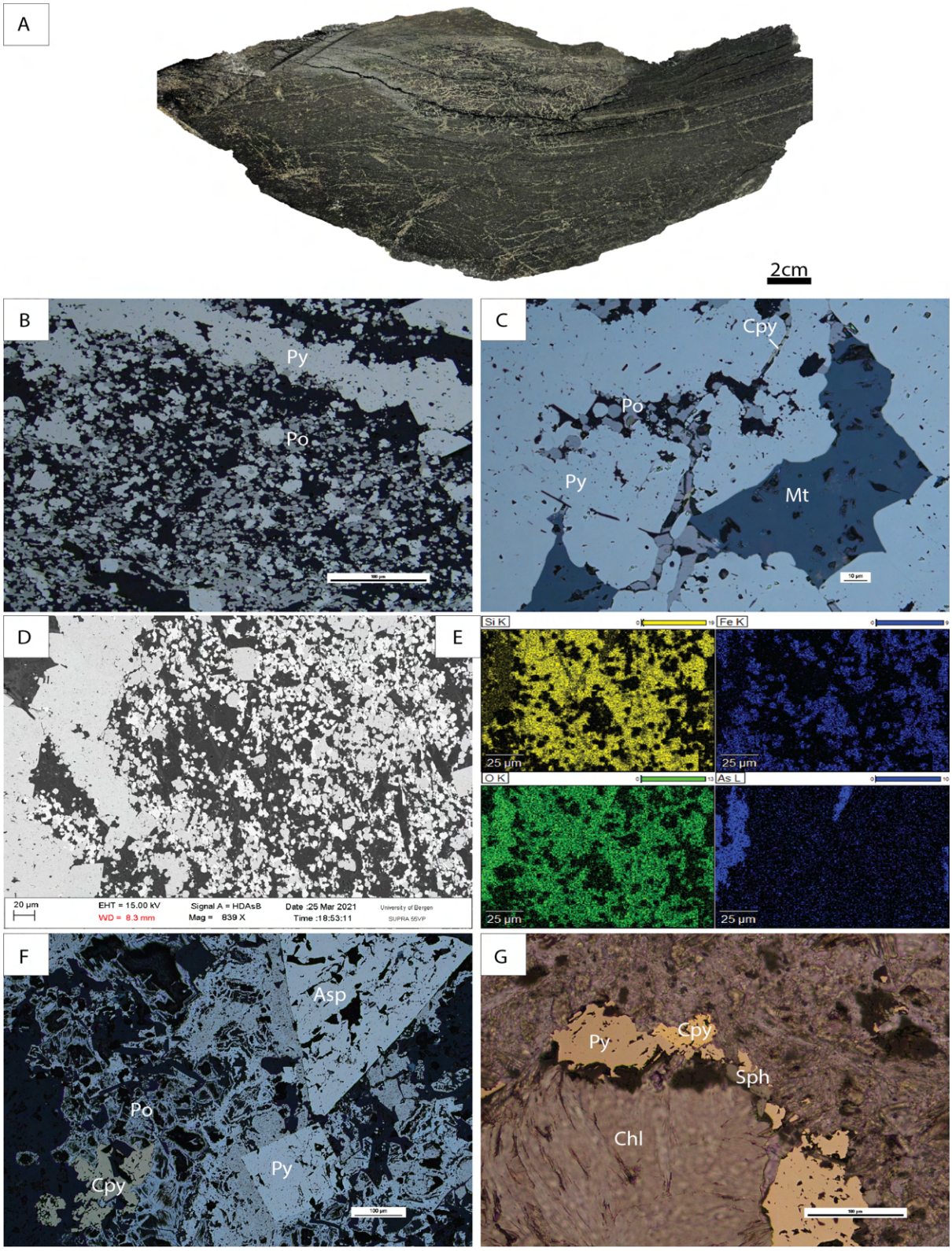


Figure26: A) Photograph of the massive mineralization (Sample 20LIND4B). B) Microphotograph of the mineralization sample illustrating the ore mineralogy under reflected light. C) Microphotograph of the massive mineralization sample under reflected light. Magnetite, pyrrhotite and chalcopyrite grains within massive pyrite. D) SEM image of the massive sulfide mineralization illustrating the mineralogical details. E) SEM-EDS analysis of the massive sulfide mineralization showing the element composition of the gangue minerals. Needle like minerals are observable with lower silika content together with variations in concentrations of arsenic. F) Microphotograph of the basaltic mineralization (sample 20LIND-H) under reflected light. Large euhedral pyrite and arsenopyrite together with weathered pyrrhotite. G) Sulfide mineralization in association with chlorite. Abbreviations: Cpy – Chalcopyrite, Po – Pyrrhotite, Py – Pyrite, Asp – Arsenopyrite, Mt – Magnetite, Chl – Chlorite.

### 6.1.3 The Litlabø area

#### 6.1.3.1 Mineralization related black shale and siliciclastic rock

The mineralization at Litlabø, the Stord island, is associated with organic rich black shales (sample 20LIT3) and a layered siliciclastic sedimentary rock (sample 20LIT8) together with cherts, greenstones and jaspers. The black shale appear as fine grained and rhythmic layers are recognized with minor amounts of visible sulfides (Figure 27A). Crosscutting the sample are yellowish minor veins. From TLM the rhythmic layering is evident, with a fine-grained matrix containing some larger unidentified transparent grains (Figure 27B). From RLM the sulfide content is evident with disseminated small grains throughout the entire sample (Figure 27D).

The layered siliciclastic rock has a dark purple color and appears somewhat coarser grained than the black shale. Crosscutting are coarse grained quartz surrounded by rims of oxidation (Figure 27D). From TLM the fine-grained matrix appears as dark in plain polarized light with smaller transparent crystals evenly distributed within (Figure 27E). Dark laminas are also recognized and RLM indicates that the layering represents fine-grained sulfides (Figure 27F). Cutting the bedding are large secondary veins of quartz and plagioclase with a rim of elongated oxidized minerals. In the center of the vein chlorite exhibiting “Berlin blue” birefringence colors are recognized and the oxidized minerals (Figure 27E) have similarities in their crystal habit and might represent iron rich chlorite, however identification is not certain from microscopic analysis.

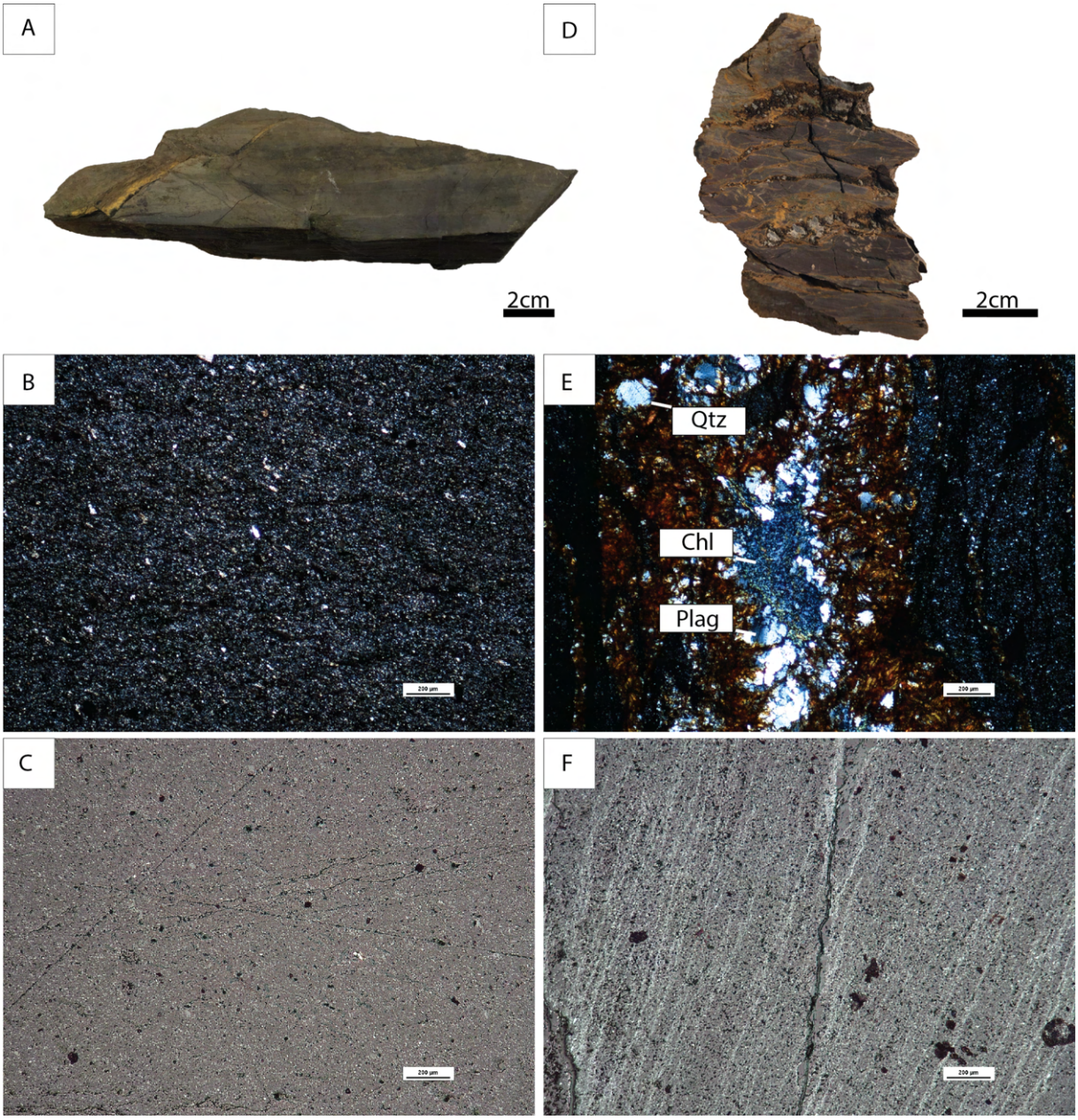


Figure 27: A) Photograph of the black shale (sample 20LIT3). B) Microphotograph of the dark shale illustrating the mineralogy under plain polarized light. C) Microphotograph of the black shale under reflected light. Small bright grains represent small sulfide crystals disseminated throughout the sample. D) Photograph of the layered siliciclastic rock (sample 20LIT8). E) Microphotograph of the layered siliciclastic rock under cross polarized light. Rusty needle-like minerals are clear along the edges and quartz, plagioclase and chlorite make up the center cutting the darker layers. F) Microphotograph of the layered siliciclastic under reflected light. Clear rhythmic layers of sulfide minerals are observed. Abbreviations: Chl – Chlorite, Qtz – Quartz, Plag – Plagioclase.

### 6.1.3.2 Massive pyrite mineralization

The ore is comprised of massive pyrite (sample 19LIT2; Figure 14A) and from RLM it is revealed that the mineral assemblage is almost exclusively comprised of massive pyrite with quartz veins cutting the bedding (Figure 14B). The massive pyrite appears as bedded and deformation features are recognized in proximity to the quartz veins. In association to the quartz veins, pyrite gets more massive often exhibiting euhedral features (Figure 13C) with minor amounts of chalcopyrite and sphalerite. SEM elemental maps (Figure 13D) show that the iron content in pyrite is homogenous while Si shows some variation, indicating the presence of at least one or more unidentified silicate mineral phases.

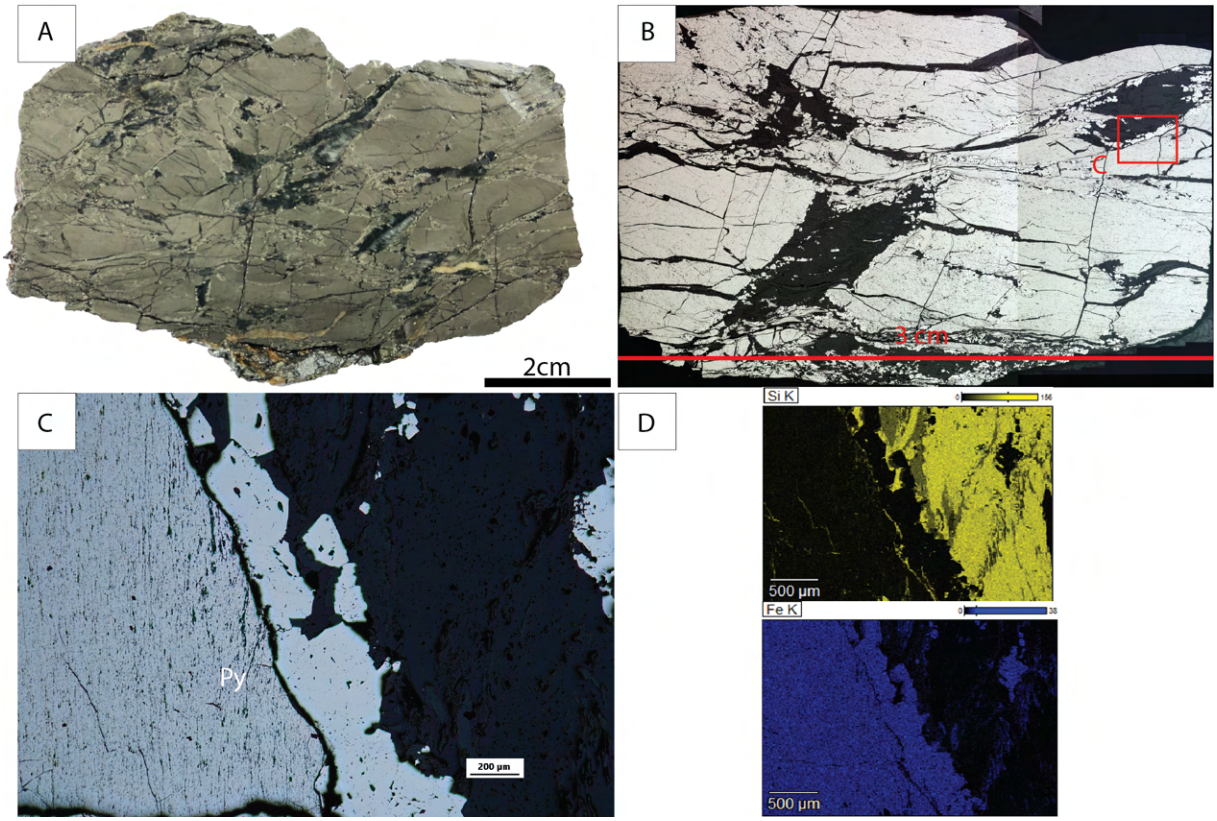


Figure 14: A) Photograph of massive pyrite mineralization (sample 19LIT2). B) Mosaic of the thin section in reflected light representing the massive pyrite with the location of the close-up image marked. C) Microphotograph of the massive pyrite mineralization under reflected light. The boundary between the two various lithologies are clear in the center of the photo with the more massive pyrite to the right. D) SEM-EDS analysis of the massive pyrite. From the Si content quartz make up the main gangue constituent together with another unknown silika phase. Abbreviations: Py – Pyrite

#### 6.1.3.3 Massive pyrrhotite mineralization

The massive pyrrhotite ore (sample 19LIT3) appears as a massive brecciated dark sulfide mineralization with clear deformation features (Figure 28A). Remnants of layering are recognized with recrystallized sulfides in between the darker layers. Deformation is evident with the original bedding destroyed in many instances appearing brecciated.

The mineralization is subdivided into two main types with one appearing as a massive pyrrhotite and the other appearing as bedded exhibiting a more variable mineralogy (Figure 28B). The main sulfide phase is pyrrhotite making out the majority of the sample which is especially evident in the massive part were other sulfide phases also occur together with silica minerals in smaller quantities. Recognized accessory phases are euhedral arsenopyrite (Figure 28C, E) and minor quantities of chalcopyrite, sphalerite and iron oxides (Figure 28B, C). The resolution of the SEM was too low for spot analysis of separate grains, however from elemental maps potassium, magnesium, calcium and aluminum were abundant (Figure 28F, G). Elemental mapping also revealed a presence of zirconium and titanium (Figure 28E, G). Titanium may indicate the presence of ilmenite or titanite, but these were not recognized from microscopic investigations.

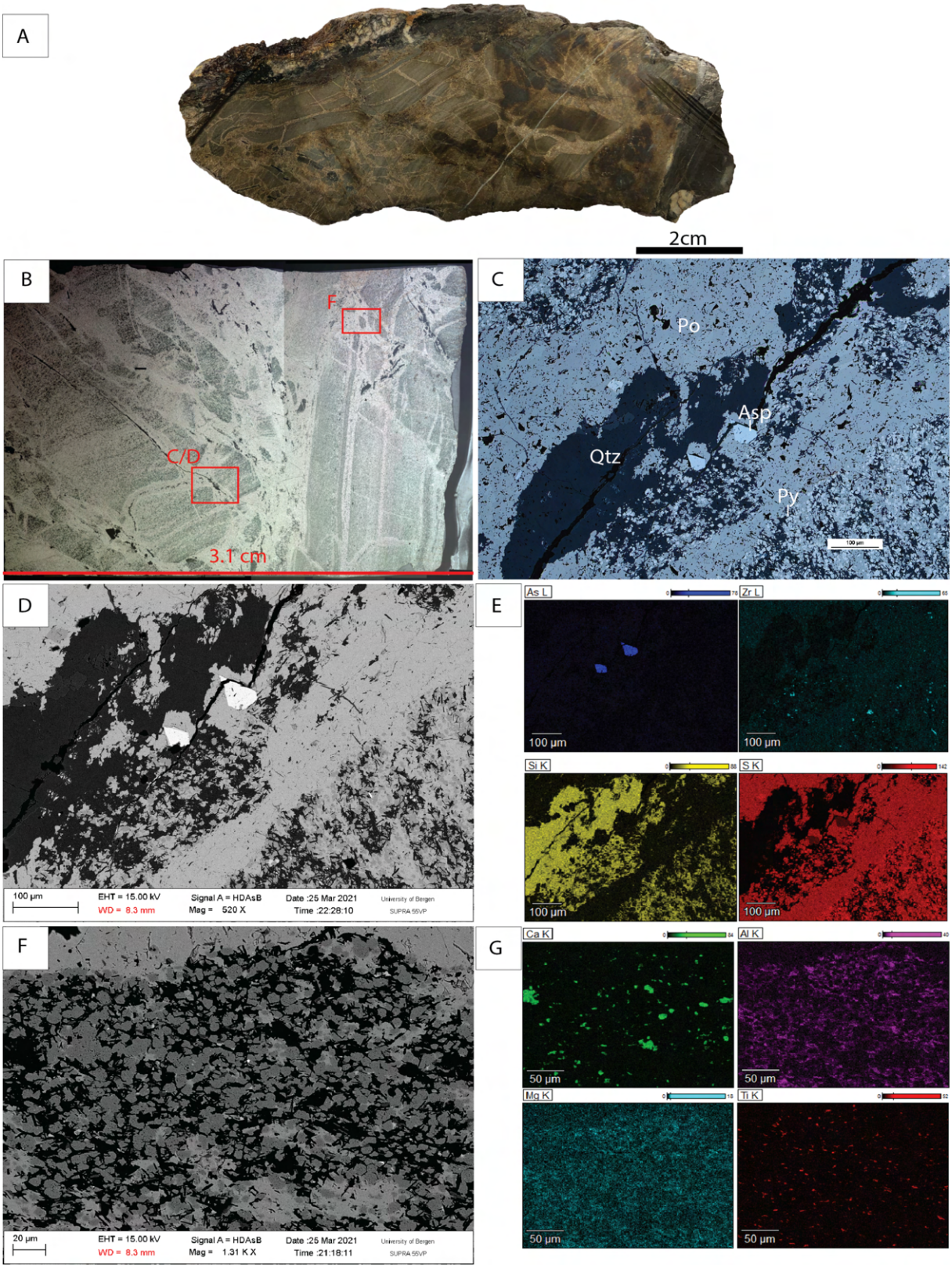


Figure 28: A) Photograph of the massive pyrrhotite mineralization (sample 20LIT3). Bedding like features as well as more brecciated parts are clearly observable in the upper part of the sample. B) Mosaic of the thin section in reflected light representing the massive pyrrhotite/pyrite mineralization with the location of the close-up images marked. C) Microphotograph of the more massive mineralized area. Vein features are evident in the center with the main mineral quartz. The more pyrite rich areas are found in association with silicate phases. D) SEM image of the area were analyzed in SEM. E) SEM-EDS analysis of the massive pyrrhotite mineralization indicating the presence of different elements. Clear variations in sulfur content indicates the various sulfide phases. F) SEM image of an area analyzed in SEM. G) SEM-EDS analysis of 20LIT3 indicating the distribution of different elements. Abbreviations: Po – Pyrrhotite, Py – Pyrite, Asp – Arsenopyrite, Qtz – Quartz.

## 6.2 Lithogeochemistry of the host rocks

Six host rock samples were selected from the Alvsvågen and Lindøya areas for the major and trace element analysis (Table 3).

### 6.2.1 Major element and rock chemistry

The major element composition of all samples is given in Table 2. All samples are characterized by low concentrations of $SiO_2$ and alkali elements, and plot as mafic rocks in the TAS (Total Alkali versus Silica) diagram (Figure 29A). The Alvsvågen samples appear as to have an overall mafic composition with the barren layered gabbro (sample 20ALS9) plotting on the border with peridot-gabbro, and the barren micro-gabbro (sample 20ALS7B) plotting in the same area with slightly elevated $Na_2O+K_2O$ levels. The gabbroic shear zone (sample 20ALS11) together with the mineralized gabbro (sample 20ALS10C) are characterized by higher concentrations of $SiO_2$, possibly indicating metamorphic or hydrothermal remobilization of mobile elements and plots as gabbroic diorite (Figure 28A). Plotted within the AFM (alkali, iron, magnesium) diagram (Figure 28C) it is evident that the rocks in Alvsvågen plots along the tholeiitic magma series. At Lindøya the micro-gabbro (sample 20LIND5) plots in the higher gabbroic area in the TAS diagram (Figure 18A) exhibiting a higher content of $Na_2O+K_2O$. From the AFM diagram (Figure 18C) the Lindøya micro-gabbro plots within the tholeiitic magma series.

Table 2: Major element composition of analyzed host rocks (in wt%).

| Locality | Sample | SiO2 | Al2O3 | Fe2O3 | MgO | CaO | Na2O | K2O | TiO2 | MnO | P2O5 | %LOI | Total% |
|---|---|---|---|---|---|---|---|---|---|---|---|---|---|
| **Alvsvågen** | **20ALS7B** | 52.07 | 16.11 | 11.50 | 7.28 | 8.54 | 3.16 | 0.13 | 0.78 | 0.19 | 0.13 | 1.17 | 101.06 |
| | **20ALS9** | 45.88 | 16.99 | 9.28 | 8.66 | 15.03 | 1.25 | 0.10 | 0.47 | 0.16 | 0.08 | 2.39 | 100.27 |
| | **20ALS10C** | 58.62 | 15.13 | 11.73 | 3.47 | 7.58 | 2.82 | 0.19 | 0.63 | 0.19 | 0.09 | 1.12 | 101.58 |
| | **20ALS11** | 57.27 | 12.55 | 16.42 | 4.57 | 3.24 | 1.54 | 0.08 | 0.83 | 0.13 | 0.14 | 4.36 | 101.12 |
| **Lindøya** | **20LIND5** | 48.40 | 14.75 | 12.37 | 7.00 | 7.74 | 3.50 | 0.60 | 1.37 | 0.20 | 0.15 | 3.96 | 100.05 |

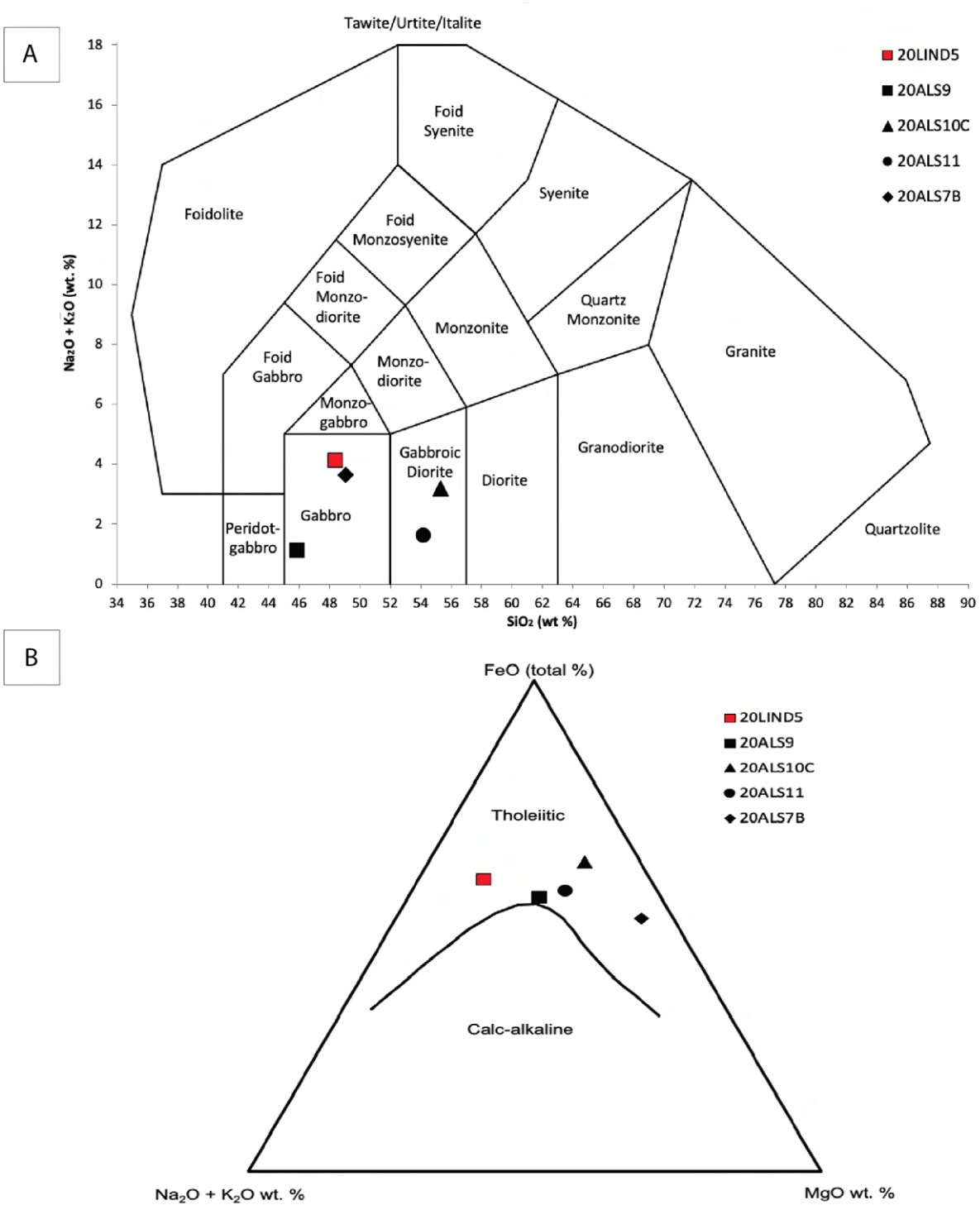


Figure 28: A) TAS diagram for plutonic rocks showing the chemical classification of the different rocks using $Na_2O+K_2O$ vs $SiO_2$. Diagram from Middlemost (1994). B) AFM diagram using MgO, FeO and Na2O+K2O for magma classification. Diagram from Marshall (1996).

### 6.2.3 Trace and Rare Earth Element (REE) composition

All trace element data from analyzed samples presented in this section are listed within Table 3, and all REE data presented are listed within Table 4.

#### 6.2.3.1 Alvsvågen

The layered barren gabbro (sample 20ALS9) show a strong depletion in light rare earth elements (LREE) relative to heavy rare earth elements (HREE) compared to the other Alvsvågen samples (Figure 29A). The barren micro-gabbro (sample 20ALS7B) is characterized by a depletion of LREE relative to HREE. The mineralized micro-gabbro (sample 20ALS7S1) show the highest concentration of REE together with a minor depletion in LREE. 20ALS7S1 also features a progressive enrichment from HREE to LREE together with a minor negative anomaly of Eu. The gabbroic shear zone (sample 20ALS11) show enrichment from HREE to LREE differentiating it from the other samples together with a minor negative anomaly of Eu. Also, to be noted is that the micro-gabbroic and shear zone lithologies are more enriched in REE relative to the gabbros.

All Alvsvågen samples are characterized by similar trace element patterns with the exception of the layered barren gabbro (sample 20ALS9; Figure 29B) which is characterized by a general depletion in the large ion lithophile elements (LILE) whit the exception of Cs and Rb. In the high field strength elements (HFSE) the trend appears as similar to the other Alvsvågen samples with depletion in Er, Zr and Hf and otherwise values close to N-MORB. The other Alvsvågen samples show strong similarities within the LILE elements (Figure 29B) with pronounced depletions in Ta and Nb and enrichment in Cs, Rb, Ba, Th, U and Pb. Some variation in amount of depletion/enrichment are recognized in the samples, however all are characterized by the same general trends.

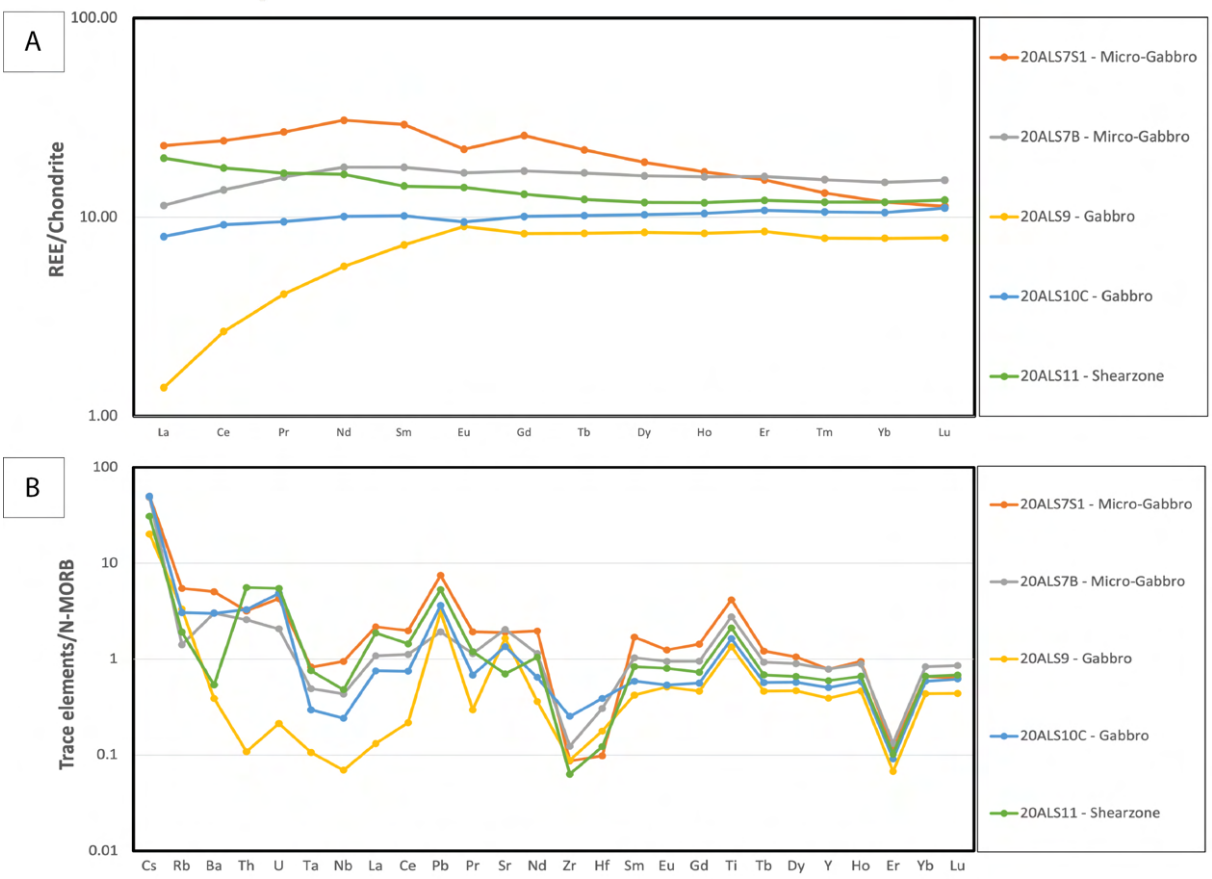


Figure 29: A) Spiderdiagram representing chondrite normalized REE patterns of the Alvsvågen samples. B) N-MORB normalized diagrams showing the trace element patterns of the same rocks. REE are normalized against Chondrite with values from Sun and McDonough (1989), and trace elements against N-MORB from Sun and McDonough (1989).

### 6.2.3.2 Lindøya

The micro-gabbro (sample 20LIND5) is characterized by a 10 times enrichment in REE relative to chondrite (Figure 30A). A small progressive enrichment from Lu to Gd is apparent together with a minor depletion in LREE. The trace element patterns are characterized by an enrichment in most of the LILE elements with the exception of Tb and Nb. Many of the HFS elements have concentrations similar to that of N-MORB but minor depletions are recognized in Zr, Hf and Er. Enrichment in Pb are also recognized.

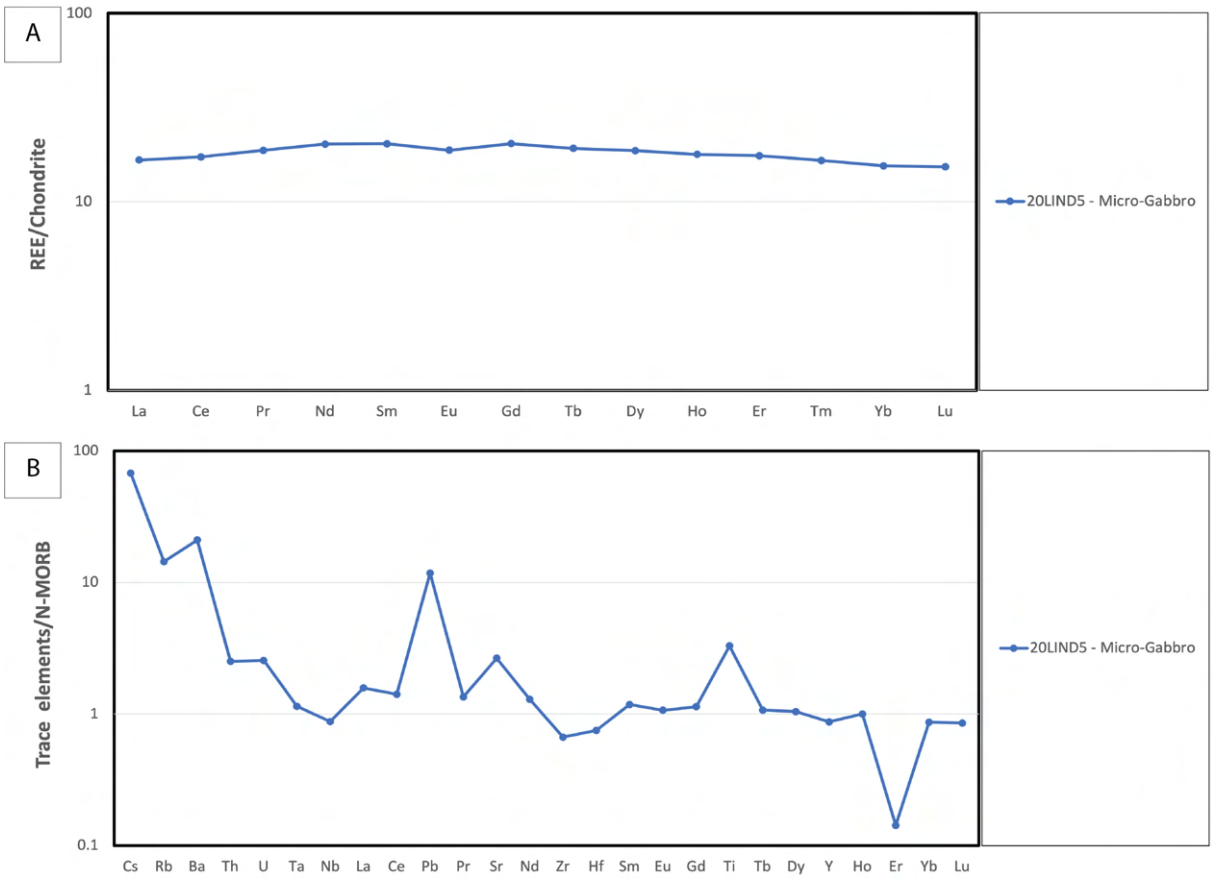


Figure 30: A) Spiderdiagram representing chondrite normalized REE patterns of the Lindøya sample. B) N-MORB normalized diagrams showing the trace element patterns of the same rock. REE are normalized against Chondrite with values from Sun and McDonough (1989), and trace elements against N-MORB from Sun and McDonough (1989).

Table 3: Trace element composition (ppm) of samples from Alvsvågen and Lindøya.

| Sample | Li | Sc | V | Cr | Co | Ni | Cu | Zn | Rb | Sr | Y | Zr | Nb | Cs | Ba | Hf | Ta | Pb | Th | U |
|---|---|---|---|---|---|---|---|---|---|---|---|---|---|---|---|---|---|---|---|---|
| **20ALS7S1** | 5.08 | 51.86 | 21.99 | 0.85 | 22.26 | 3.07 | 21571.50 | 89.56 | 3.06 | 170.5 | 21.92 | 6.43 | 2.21 | 0.351 | 31.76 | 0.201 | 0.109 | 2.25 | 0.382 | 0.201 |
| **20ALS7B** | 4.88 | 41.06 | 234.2 | 67.23 | 35.80 | 44.64 | 82.58 | 59.60 | 0.791 | 184.0 | 22.30 | 9.13 | 1.01 | 0.339 | 19.05 | 0.628 | 0.065 | 0.578 | 0.309 | 0.097 |
| **20ALS9** | 9.54 | 45.96 | 230.2 | 454.3 | 40.37 | 70.86 | 81.46 | 54.11 | 1.87 | 148.3 | 11.34 | 6.51 | 0.162 | 0.141 | 2.45 | 0.364 | 0.014 | 0.933 | 0.013 | 0.010 |
| **20ALS10C** | 9.66 | 35.46 | 355.1 | 5.23 | 23.52 | 5.23 | 205.10 | 86.51 | 1.71 | 121.4 | 14.68 | 18.72 | 0.565 | 0.351 | 18.93 | 0.799 | 0.039 | 1.09 | 0.394 | 0.228 |
| **20ALS11** | 10.62 | 23.70 | 157.8 | 69.28 | 33.91 | 38.37 | 2250.50 | 55.26 | 1.07 | 63.10 | 17.60 | 4.68 | 1.12 | 0.216 | 3.39 | 0.250 | 0.100 | 1.60 | 0.668 | 0.257 |
| **20LIND5** | 12.48 | 39.80 | 337.6 | 113.5 | 40.95 | 35.75 | 46.70 | 107.0 | 8.07 | 238.9 | 24.81 | 49.40 | 2.04 | 0.474 | 132.4 | 1.54 | 0.151 | 3.54 | 0.301 | 0.120 |

Table 4: Rare earth element (REE) composition (ppm) of samples from Alvsvågen and Lindøya.

| Sample | La | Ce | Pr | Nd | Sm | Eu | Gd | Tb | Dy | Ho | Er | Tm | Yb | Lu |
|---|---|---|---|---|---|---|---|---|---|---|---|---|---|---|
| **20ALS7S1** | 5.42 | 14.82 | 2.54 | 14.31 | 4.46 | 1.27 | 5.28 | 0.813 | 4.79 | 0.955 | 2.55 | 0.337 | 2.02 | 0.288 |
| **20ALS7B** | 2.71 | 8.39 | 1.51 | 8.31 | 2.72 | 0.967 | 3.50 | 0.623 | 4.09 | 0.901 | 2.65 | 0.393 | 2.54 | 0.389 |
| **20ALS9** | 0.330 | 1.63 | 0.390 | 2.64 | 1.11 | 0.521 | 1.70 | 0.310 | 2.13 | 0.470 | 1.40 | 0.200 | 1.33 | 0.200 |
| **20ALS10C** | 1.89 | 5.60 | 0.902 | 4.71 | 1.55 | 0.548 | 2.07 | 0.381 | 2.61 | 0.591 | 1.79 | 0.271 | 1.79 | 0.282 |
| **20ALS11** | 4.69 | 10.81 | 1.58 | 7.66 | 2.19 | 0.816 | 2.68 | 0.459 | 3.01 | 0.669 | 2.01 | 0.303 | 2.02 | 0.310 |
| **20LIND5** | 4.11 | 11.03 | 1.85 | 9.84 | 3.24 | 1.14 | 4.35 | 0.748 | 4.95 | 1.05 | 3.03 | 0.440 | 2.75 | 0.405 |

## 6.3 Ore grade

All four samples from Alvsvågen exhibit high Cu contents ranging between 1.19 wt.% to >10 wt.% (Table 5) and gold contents correlates positively with the amount of Cu. Silver ranges from 3 - 12 ppm and together with Fe and S follow the same correlation towards Cu. Other base metals have low concentrations, usually <0.01 % with some minor variations among samples. Sample 20ALS7S1 differs from other analyzed samples by higher contents of Al (8.5 wt.%), Mg (1.55 wt.%) and Na (4.39 wt. %).

The two analyzed samples from Lindøya exhibits variation in regard to concentrations in elements and metals. The massive bedded mineralization (sample 20LIND4B) almost exclusively contains Fe (30.6 wt.%) and S (>30 wt.%) together with a minor concentration of Al (1 wt.%). Concentration of base metals such as Cu, Ni, Pb and Zn are in the range of ~ 0.001 wt.%. Arsenic and Mn have somewhat higher concentrations in the range of ~ 0.3 wt.%. and the Au content is low at 67 ppb. The basalt hosted mineralization (sample 20LIND-H) show a different composition to the previous sample with a generally lower metal content. This is observed through the low content of Fe (7.28 wt.%) and S (4.2 wt.%) and higher Al (9.12 wt.%) values together with Mg (3.04 wt.%) and Na (4.83 wt.%) reflecting the basaltic rock. All other base metals have low concentrations in the range of ~0.02 - 0.01 wt.% except for Mn with 0.09 wt.%. Gold content is low as 14 ppb (Table 5).

From the sediment hosted mineralizations at Litlabø both samples contain primarily Fe and S with some variation between the two samples. The massive pyrrhotite mineralization (sample 19LIT3) almost exclusively contains Fe (51 wt.%) and S (24.8 wt.%) together with an Au content of 201 ppb. Base metal content is low and in the range of 0.001 – 0.21 wt.%. The massive pyrite (sample 19LIT2) contains mainly Fe (38.4 wt.%) and S (>30 wt.%). Base metal content is minor and in the range of ~ 0.001 – 0.04 wt.%. Gold content is low at 39 ppb (Table 5).

Table 5: Ore grade data of selected samples. All results are given in wt% with the exception of Au and Ag which are given inn ppb and ppm respectively. Values below <0.001 are below the detection limit.

| Sample | Au ppb | Mo% | Cu% | Pb% | Zn% | Ag ppm | Ni% | Co% | Mn% | Fe% | As% | Sr% | Cd% | Sb% | Bi% | Ca% | P% | Cr% | Mg% | Al% | Na% | K% | W% | S% |
|---|---|---|---|---|---|---|---|---|---|---|---|---|---|---|---|---|---|---|---|---|---|---|---|---|
| **20LIND4B** | 67 | 0.004 | 0.008 | <0.02 | 0.02 | <2 | 0.003 | <0.001 | 0.03 | 30.61 | 0.03 | <0.01 | <0.001 | <0.01 | <0.01 | 0.16 | <0.01 | 0.001 | 0.6 | 1.14 | 0.13 | 0.3 | <0.01 | >30.00 |
| **20LINDH** | 14 | <0.001 | 0.006 | <0.02 | 0.01 | <2 | 0.001 | <0.001 | 0.09 | 7.28 | <0.02 | <0.01 | <0.001 | <0.01 | <0.01 | 0.96 | 0.07 | <0.001 | 3.04 | 9.12 | 4.83 | 0.11 | <0.01 | 4.19 |
| **20ALS7S1** | 40 | <0.001 | 3.339 | <0.02 | 0.01 | 3 | <0.001 | 0.004 | 0.09 | 9.04 | <0.02 | 0.02 | <0.001 | <0.01 | <0.01 | 2.18 | 0.18 | <0.001 | 1.55 | 8.5 | 4.39 | 0.21 | <0.01 | 2.9 |
| **20ALS7S3** | 85 | <0.001 | >10.000 | <0.02 | 0.04 | 12 | 0.006 | 0.029 | 0.02 | 15.02 | <0.02 | <0.01 | <0.001 | <0.01 | <0.01 | 1 | 0.04 | <0.001 | 0.9 | 1.58 | 0.17 | 0.03 | <0.01 | 10.18 |
| **20ALS6D1** | 70 | <0.001 | 5.427 | <0.02 | 0.03 | 5 | 0.01 | 0.036 | 0.04 | 19.47 | <0.02 | <0.01 | <0.001 | <0.01 | <0.01 | 0.71 | 0.01 | 0.001 | 1.37 | 2.13 | 0.69 | 0.02 | <0.01 | 7.86 |
| **20ALS3S1** | 45 | <0.001 | 1.196 | <0.02 | 0.03 | 3 | 0.005 | 0.011 | 0.02 | 9.63 | <0.02 | <0.01 | <0.001 | <0.01 | <0.01 | 0.13 | <0.01 | 0.012 | 0.38 | 0.57 | 0.11 | 0.02 | <0.01 | 5.76 |
| **19LIT3** | 201 | 0.002 | 0.056 | 0.07 | 0.12 | <2 | 0.021 | 0.005 | 0.15 | 51.84 | 0.04 | <0.01 | <0.001 | <0.01 | <0.01 | 0.15 | 0.07 | <0.001 | 0.17 | 0.36 | 0.03 | 0.12 | <0.01 | 24.87 |
| **19LIT2** | 39 | <0.001 | 0.035 | <0.02 | 0.04 | 2 | 0.006 | <0.001 | 0.07 | 38.4 | 0.05 | <0.01 | <0.001 | <0.01 | <0.01 | 0.7 | <0.01 | <0.001 | 0.17 | 0.69 | <0.01 | 0.23 | <0.01 | >30.00 |

## 6.4 Sulfur stable isotopes

Sulfur isotope values of sulfide minerals from the Alvsvågen deposit range from 0.4 ‰ to 3.9 ‰ V-CDT (n=12; mean=1.6 ‰; Table 6). The basalt hosted and massive sulfide mineralization at Lindøya exhibit $\delta^{34}S$ values ranging from 4.9‰ to 5.9‰ V-CDT (n=5; mean=5.4 ‰). The massive sulfide mineralizations from Litlabø show a strong depletion with $\delta^{34}S$ values ranging between -19.7 ‰ and -15.7 ‰ V-CDT (n=4; mean= 17.6 ‰) (Table 6). The samples show variation from each other with 19LIT2 exhibiting $\delta^{34}S$ values of ~ 19 ‰ with minor internal variation within the sample. The same is for 19LIT3 which have slightly lower $\delta^{34}S$ values of ~15 ‰ with minor internal variation within the sample.

Table 6: Overview over all samples analyzed for sulfur isotopes together with lithology and mineralogy of analyzed grains. Po1-2-3-4 represent that several sulfides were analyzed from each sample.

| **Locality** | **Sample** | **Mineralization type** | **Mineralogy** | **$\delta^{34}S$ V-CDT (‰)** |
|---|---|---|---|---|
| **Alvsvågen** | 20ALS3S1 | Shear zone | Pyrite | 0.5 |
| | 20ALS3S2-po1 | Shear zone | Pyrite | 3.9 |
| | 20ALS3S2-po2 | Shear zone | Pyrite | 0.4 |
| | 20ALS4E | Micro-Gabbro | Pyrite | 1.8 |
| | 20ALS4F | Coarse-Gabbro | Pyrite | 3 |
| | 20ALS7S1-po2 | Micro-Gabbro | Pyrite | 2.4 |
| | 20ALS7S3-po1 | Gabbro | Pyrite | 1.4 |
| | 20ALS7S3-po2 | Gabbro | Pyrite | 1.6 |
| | 20ALS6D1-po1 | Shear zone | Pyrite | 1.5 |
| | 20ALS6D1-po2 | Shear zone | Pyrite | 0.6 |
| | 20ALS6D2 | Shear zone | Pyrite | 1.8 |
| | 20ALS10B | Gabbro | Chalcopyrite | 0.9 |
| **Lindøya** | 20LIND-H | Basalt | Pyrite | 4.9 |
| | 20LIND4B-po1 | Basalt | Pyrite | 5.9 |
| | 20LIND4B-po2 | Basalt | Pyrite | 5.7 |
| | 20LIND4B-po3 | Basalt | Pyrrhotite | 5.9 |
| | 20LIND4B-po4 | Basalt | Pyrrhotite | 5.7 |
| **Litlabø** | 19LIT2-po1 | Sediment | Pyrite | -19.3 |
| | 19LIT2-po2 | Sediment | Pyrite | -19.7 |
| | 19LIT3-po1 | Sediment | Pyrrhotite | -15.8 |
| | 19LIT3-po2 | Sediment | Pyrrhotite | -15.7 |

## 6.5 Chlorite thermometry

The chlorite thermometry was applied to the mineralized gabbro (sample 20ALS4E) with an aim to determine temperature of chlorite crystallization as a proxy for temperature of formation of the Alvsvågen Cu mineralization. Based on SEM-EDS data (Table 7) and the chlorite thermometer from Jowett (2021) the chlorite composition corresponds to ripidolite. Temperatures were estimated to range between 363 to 398 °C with a mean of 372 °C. Some internal variation in temperatures from single chlorite grains are recognized.

Table 7: Overview over SEM-EDS data used for calculation and estimated temperatures. A total SUM of 100 are not reached as the rest of the mineral is attributed to OH groups which the SEM cannot measured.

| Spot ID | MgO | Al2O3 | SiO2 | FeO | SUM | Temperature °C |
|---|---|---|---|---|---|---|
| **Chlorite 1-1** | 15.64 | 22.14 | 26.70 | 28.17 | 92.65 | 363 |
| **Chlorite 3-2** | 17.23 | 22.24 | 25.56 | 26.67 | 91.70 | 398 |
| **Chlorite 3-3** | 17.23 | 22.24 | 25.56 | 26.67 | 91.70 | 398 |
| **Chlorite 3-4** | 13.27 | 19.95 | 26.72 | 33.65 | 93.59 | 348 |
| **Chlorite 3-5** | 17.40 | 23.90 | 27.00 | 26.51 | 94.81 | 383 |
| **Chlorite 4-1** | 13.27 | 19.95 | 26.72 | 33.65 | 93.59 | 348 |
| **Chlorite 4-2** | 14.34 | 21.03 | 26.40 | 32.45 | 94.22 | 371 |
| **Chlorite 5-1** | 13.58 | 23.54 | 26.10 | 33.95 | 97.17 | 404 |
| **Chlorite 5-2** | 13.32 | 19.86 | 27.92 | 35.20 | 96.29 | 331 |

## 6.7 Trace element composition of ore minerals

The results of the LA-ICP-MS analyses obtained from the sulfide minerals are listed in Appendix B while summary statistics are listed in Table 8. Distribution of selected trace and minor elements among the main sulfide phases is presented as box plots in Figure 32.

The Alvsvågen *pyrrhotite* is enriched in Co and the median concentration is 750.61 ppm. The range in cogenerations is large, extending from 8.45 ppm to 2276.11 ppm. Nickel and Se show comparable enrichments with median values of 498.756 ppm and 295.651 ppm respectively. The other elements exhibit mostly minor enrichments with median values in the range of ~ 0.006 – 2 ppm. Gold content is low with only one measurement above the detection limit. *Chalcopyrite* is enriched in Zn (Med, 600.078 ppm) and Se (Med, 332.657 ppm). Chalcopyrite also shows enrichment in some of the chalcophile elements (Ag, Cd, In and Te) relative to pyrrhotite and pyrite. All other elements show only minor enrichments. *Pyrite* show enrichment in Co and Se with median concentrations of 2131.62 ppm and 298.158 ppm respectively. Cobalt exhibit a considerable range in concentrations extending from 17.5 ppm to 4866.86 ppm. The base metals Zn and Cu show minor enrichments along with Te. Also recognized from these elements are large ranges in concentrations.

The Litlabø *pyrite* show large enrichment in Zn and As with median concentrations of 2294.074 ppm and 759.984 ppm respectively. Zinc show a large range in concentrations while As content appear as more uniform. Some redox elements (Mo, V, Mn and U) show minor enrichment together with the base metals Cu, Ni, Pb and Co. Gold content generally low though some range is recognized. Only one measurement was acquired of *pyrrhotite* from the Litlabø deposit. Major enrichments in the base metals Zn and Cu is recognized with concentrations of 247414.1 ppm and 8003.59 ppm respectively. Manganese and Cd show enrichment, but to a lesser degree than Zn and Cu. Minor enrichments are also recognized in As, Se, In, Sb and Pb.

Table 8: Trace and minor element composition for each of the mineral phases at both localities. Values represented are the median (Med), maximum (Max) and the minimum (Min). n = x resents the number of measurements on which the values are based on. Abbreviations: Po – Pyrrhotite, Cpy – Chalcopyrite, Py - Pyrite

| | **Alvsvågen** | | | | | | | | | **Litlabø** | | | |
|---|---|---|---|---|---|---|---|---|---|---|---|---|---|
| | **Po n=15** | | | **Cpy n=13** | | | **Py n=10** | | | **Py n=12** | | | **Po n=1** |
| | **Med** | **Max** | **Min** | **Med** | **Max** | **Min** | **Med** | **Max** | **Min** | **Med** | **Max** | **Min** | **Values** |
| **Co** | 750.61 | 2276.11 | 8.45 | 3.925 | 11.66 | 0.050 | 2132.62 | 4866.86 | 17.15 | 4.957 | 9.13 | 1.13 | 0.165 |
| **Ni** | 498.756 | 680.85 | 266.44 | 16.268 | 19.62 | 12.17 | 4.923 | 20.47 | 0.87 | 31.331 | 88.87 | 7.41 | 126 |
| **Mo** | 2.19 | 1.679 | 1.636 | 0.688 | 0.857 | 0.495 | 1.648 | 2.2 | 1.293 | 9.458 | 30.56 | 1.3 | 5.57 |
| **V** | 0.023 | 0.114 | 0.002 | 0.255 | 2.85 | 0.002 | 0.033 | 0.158 | 0.001 | 18.021 | 65.6 | 1.25 | 5.93 |
| **Cr** | 1.870 | 4.56 | 0.097 | 3.154 | 18.36 | 0.71 | 0.051 | 0.056 | 0.043 | 39 | 208.59 | 4.75 | 4.14 |
| **Mn** | 1.078 | 2.64 | 0.59 | 1.332 | 9.71 | 0.1 | 0.591 | 0.95 | 0.428 | 6.59 | 19.97 | 1.29 | 1246.73 |
| **Cu** | 0.411 | 1.671 | 0.043 | 293964.075 | 335244.59 | 8.11 | 5.850 | 49.51 | 0.255 | 6.59 | 19.97 | 1.29 | 8003.59 |
| **Ge** | 0.805 | 1.86 | 0.055 | 0.564 | 1.59 | 0.048 | 0.856 | 1.25 | 0.51 | 1.266 | 1.74 | 0.84 | 0.124 |
| **Zn** | 0.541 | 1.78 | 0.087 | 600.078 | 1062.2 | 439.64 | 5.891 | 56.13 | 0.0459 | 2294.074 | 27360.35 | 0.31 | 247414.11 |
| **As** | 2.695 | 3.58 | 1.87 | 2.12 | 2.95 | 1.31 | 81.446 | 257.17 | 0.6 | 759.984 | 1104.23 | 423.21 | 37.33 |
| **Se** | 295.651 | 389.42 | 243.42 | 332.657 | 433.69 | 255.81 | 298.158 | 723.19 | 79.76 | 4.184 | 7.89 | 0.294 | 35.01 |
| **Ag** | 0.623 | 2.09 | 0.025 | 18.052 | 31 | 12.05 | 0.065 | 0.509 | 0.001 | 0.709 | 2.41 | 0.080 | 6.7 |
| **Cd** | 0.032 | 0.101 | 0.006 | 9.167 | 15.93 | 5.26 | 0.074 | 0.53 | 0.002 | 13.877 | 164.84 | 0.005 | 1376.66 |
| **In** | 0.003 | 0.015 | 0.0004 | 12.306 | 23.22 | 3.01 | 0.005 | 0.024 | 0.0002 | 0.113 | 1.29 | 0 | 13.34 |
| **Sb** | 0.477 | 2.63 | 0.0019 | 0.382 | 0.51 | 0.275 | 0.638 | 2.22 | 0.0009 | 6.725 | 18.67 | 0.69 | 10.51 |
| **Te** | 1.261 | 1.84 | 0.73 | 15.848 | 19.83 | 10.74 | 8.280 | 36.38 | 0.007 | 0.124 | 0.262 | 0.007 | 0.015 |
| **Hg** | 0.690 | 1.48 | 0.21 | 0.954 | 1.62 | 0.23 | 0.246 | 0.73 | 0.017 | 0.822 | 5.35 | 0 | 37.01 |
| **Tl** | 0.006 | 0.038 | 0.0005 | 0.004 | 0.011 | 0.0005 | 0.0018 | 0.005 | 0.0003 | 0.507 | 1.2 | 0.101 | 1.63 |
| **Pb** | 1.226 | 6.64 | 0.0009 | 1.021 | 1.9 | 0.428 | 0.629 | 1.68 | 0.009 | 23.580 | 64.28 | 3.53 | 50.42 |
| **Au** | <DL | 0.003 | <DL | <DL | 0.003 | <DL | 0.004 | 0.006 | 0.0037 | 0.026 | 0.057 | 0.001 | 0.041 |
| **U** | <DL | <DL | <DL | <DL | 0.002 | <DL | <DL | <DL | <DL | 0.215 | 0.95 | 0.009 | 0.99 |

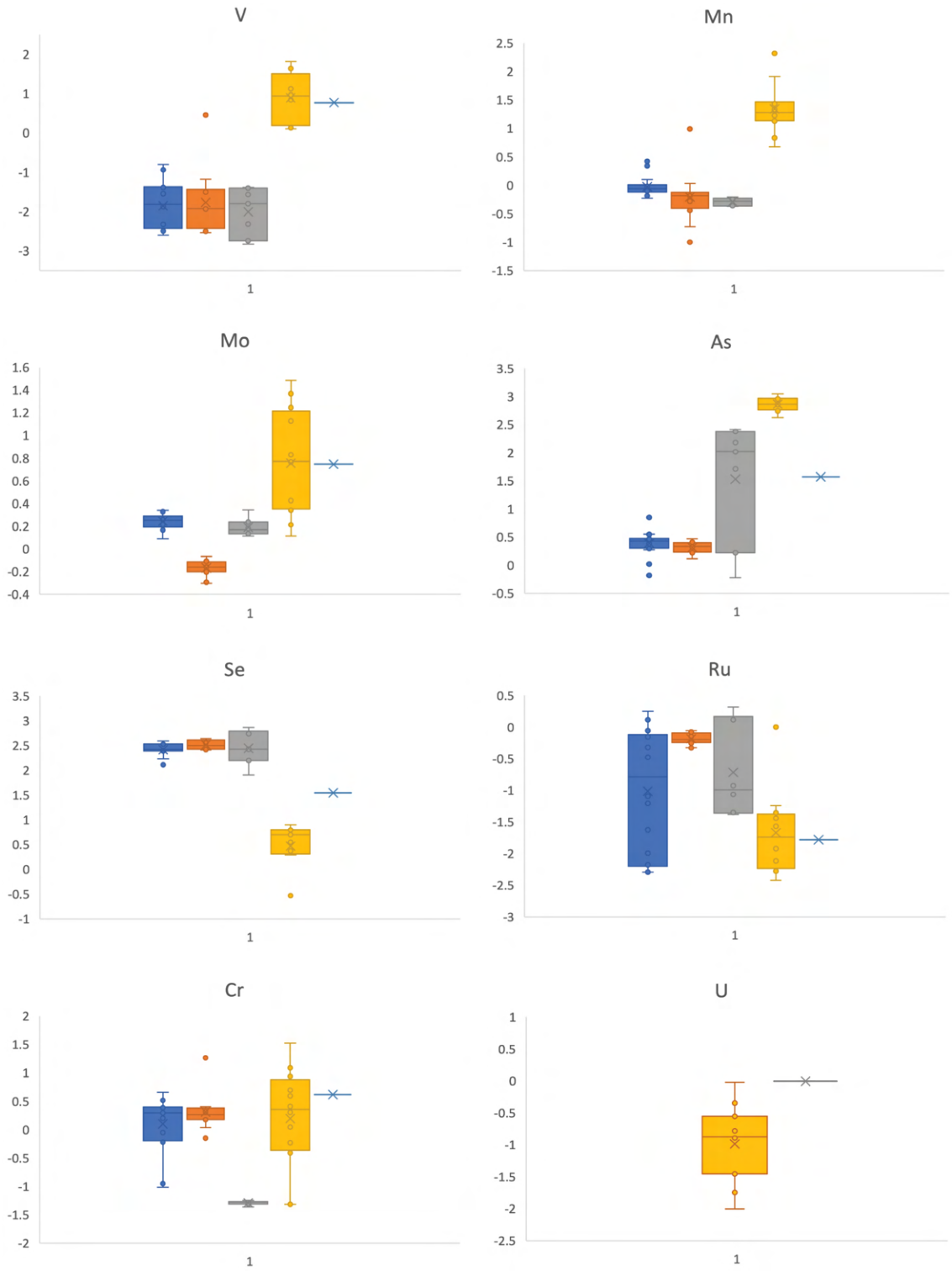


Figure 31: (Continued)

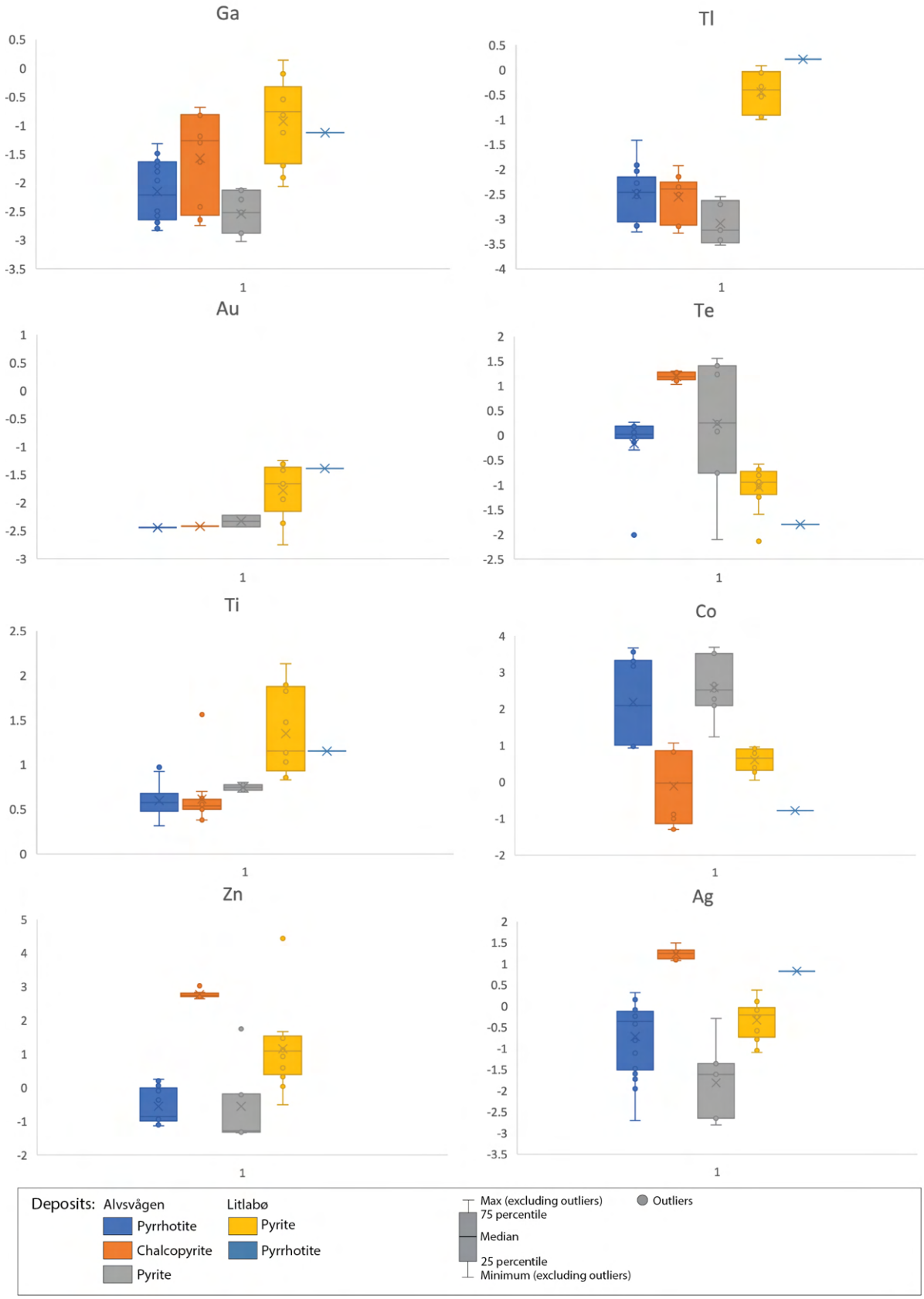


Figure 31: Boxplots of some selected minor and trace elements from sulfide minerals analyzed with LA-ICP-MS. All values were recalculated to log (10) as to make them more representable in the boxplots. Original values are given in ppm and are listed in Appendix B.

# 7 Discussion

## 7.1 The Alvsvågen Cu deposit

### 7.1.1 Geotectonic environment of the Alvsvågen area

The Alvsvågen deposit is hosted by gabbroic rocks (Figure 28A) of the Lykling Ophiolite Complex. The AFM diagram (Figure 28B) indicates their tholeiitic character. Both mineralized and barren types of the gabbroic rocks exhibit similar trace element and REE trends. Still, some minor variations in both REE and trace element composition have been recognized (Figure 29). The layered gabbro samples (sample 20ALS9 and 20ALS10C) show depletion in REE compared to micro-gabbro (samples 20ALS7S1 and 20ALS7B) and to the mineralized gabbro in the shear zone (sample 20ALS11). All types of gabbro from the Alvsvågen area (layered vs. micro-gabbro; barren vs. mineralized) with the exception of the gabbroic shear zone are characterized by a depletion in LREE that indicates a depleted mantle source similar to MORB (Sun and McDonough, 1989).

The spider diagrams (Figure 29B) reveal that all samples feature similar trends with depletion in Ta and Nb and enrichment in Th, U and Pb resembling a subduction zone related signature (Perfit et al., 1980). The exception is the barren layered gabbro 20ALS9 which is characterized by depletions in almost all incompatible elements with the exception of the highly mobile Cs and Rb. The geochemical differences indicate that the ore hosting lithologies formed in a different environment relative to the layered gabbro and supports the presence of a high-level gabbroic zone. Previously, a supra-subduction zone (SSZ) affinity has been proposed for the overlying Geitung Unit by Pedersen and Dunning (1997) and the samples from the Alvsvågen area exhibit similar trace element characteristics. A SSZ-influenced basaltic rock typically features trace element patterns with enrichment in Sr, Rb, Ba, Th ± Ce ± Sm and lack of enrichment in Ta, Nb, Hf, Zr, Ti, Y and Yb (Pearce et al., 1984). These characteristics are also recognized in the trace element patterns from the Alvsvågen samples with the exception of the layered barren gabbro (sample 20ALS9). A SSZ affinity for the ore hosting lithologies in Alvsvågen is therefore likely, and the same geochemical traits are also recognized from a study on meta-basalts from the Lykling ophiolite Complex (Furnes et al., 1982). This supports a model where the formation of the high-level gabbro occurred above a subduction zone. On the other hand, the barren layered gabbro 20ALS9 show a more depleted signature in many of the incompatible elements but additionally features many of the subduction related characteristics with enrichment in Cs, Rb, Pb and Ti. A gradual evolution of the ophiolite might therefore be

inferred. In the shear zone that crosscuts the gabbroic lithology (sample 20ALS11) one would expect a high degree of alteration and mobilization of trace elements from the hydrothermal fluids, however the trace element composition closely resembles all other high-level gabbro. Variation is noted in Ba which show strong depletion while Sr exhibit a minor depletion. According to Humphris and Thompson (1978), Ba typically show minor mobilization in hydrothermal systems but exhibit considerable general variations in concentration, while Sr tends to follow Ca, leaching from the rock. Anyway, in the case of the gabbroic shear zone sample leaching of Ba during hydrothermal alteration is most likely as no other samples show such features.

### 7.1.2 Mineral assemblages

The Alvsvågen deposit is characterized by mineral assemblages composed of chalcopyrite, pyrrhotite, Fe-oxides, sphalerite ± cubanite, titanite, ilmenite and pyrite (Table 11). The gabbro hosted mineralizations have similar mineral assemblages but show different characteristics. In the micro-gabbro the mineralization appears as lenses and disseminations while the coarser gabbro mostly features sulfides as disseminations. This might be attributed to that the coarse-grained gabbro was more resistant to deformation with fewer open spaces forming to host concentrations of sulfides. Ilmenite is only recognized in the coarse-grained gabbro and is determined as to be native to the gabbro as it is also found in the general matrix. Titanite in the micro-gabbro also show similar characteristics as it is also recognized in the general matrix but can also be formed by the hydrothermal circulation as it is a common alteration product from high temperature reduced fluids (Alt et al., 2010). The shear zones exhibit similar mineral assemblages as the gabbroic samples but host a higher content of pyrite and a more varying chalcopyrite content. Also, in the northern shear zone cubanite lamella in chalcopyrite were observed. The presence of cubanite in association with chalcopyrite and pyrite may reflect formation temperatures above 300°C (Novoselov et al., 2015).

Two studied shear zones show differences in their mineral and metal contents. Ore grade indicates a significantly higher Cu content in the northern shear zone (~10 and ~5 wt.% Cu; Table 5) compared to the southern shear zone (1 wt.% Cu; Table 5). The northern shear zone has a higher abundance of chalcopyrite together with cubanite. In comparison, the southern shear zone contains more pyrrhotite relative to chalcopyrite. This variation might be a result of selective sampling, however, variation in textures are recognized with pyrite in the southern

shear zone appearing as more euhedral and chalcopyrite and sphalerite appearing in close association (Figure 26D). In the northern shear zone, pyrite is less common and appear as more brecciated with the other phases filling in (Figure 26B). These observations might indicate varying formational conditions caused by different degree of deformation in the shear zones, temperature differences and/or different fluid/rock ratios. In the hand sample (20ALS6D1; Figure 26A) chalcopyrite and pyrrhotite often appear as separate phases which might indicate that the ore forming conditions or Cu content in the fluids varied over time. These features are not recognized in the southern shear zone, highlighting the likelihood of different formational environments between the two shear zones.

### 7.1.3 Trace and minor element composition of the Alvsvågen sulfides

Most of the trace and minor elements hosted incorporated in sulfide minerals within the gabbro and shear zone hosted mineralization show similar compositions with some exceptions. The two different shear zones also show similarities in most elements which may indicate formation from the same metal-bearing fluid. Variations are however recognized between the different coexisting mineral phases (Figure 32). Chalcopyrite shows enrichment in some of the chalcophile and fluid mobile elements, including Zn, Ag, Cd, In and Sn, compared to pyrite and pyrrhotite, indicating that Cu was hydrothermally introduced into the system. Arsenic is enriched in pyrite compared to the other sulfide phases (Figure 32), as substitution of Fe with As is a common feature in pyrite (Deditius et al., 2008). Cobalt show enrichment in pyrite and pyrrhotite relative to chalcopyrite (Figure 32). Internal variation is also recognized between the shear zones and the gabbro. In the gabbroic sample (20ALS4F) the pyrrhotite show enrichment in Co, and the pyrite relative depletion. In the Shear zone samples (20ALS3S1) the opposite is recognized with Co depletion in pyrrhotite and enrichment in pyrite. The Co depleted pyrrhotite are all located in close proximity to large euhedral pyrite. One can infer from this that the when the pyrite formed, Co preferentially chose to incorporate into the crystal lattice of pyrite compared to pyrrhotite as enrichment in Co is recognized when not in proximity to pyrite.

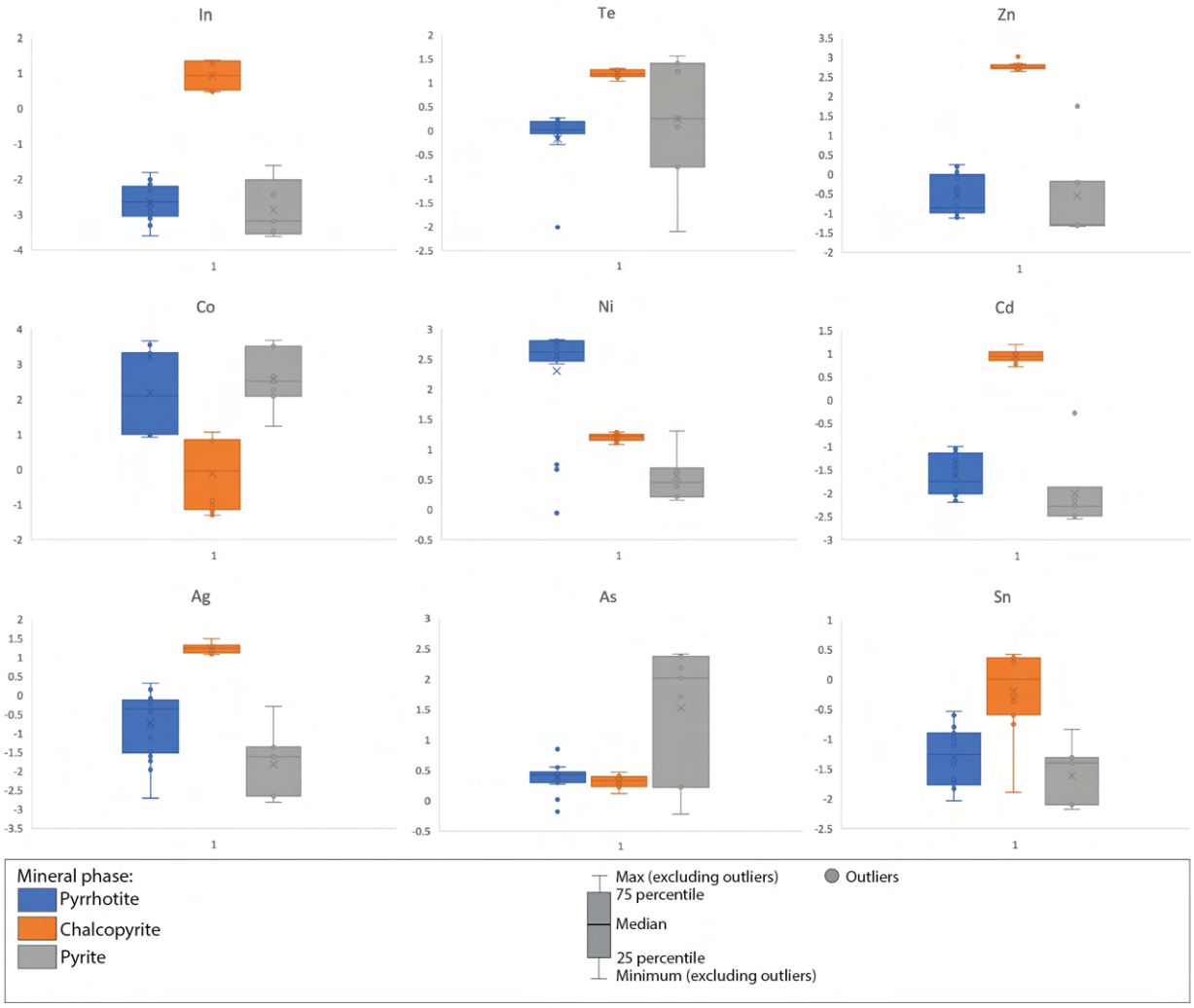


Figure 32: Boxplots showing concentrations of selected minor and trace elements in sulfide minerals from the Alvsvågen deposits. All values are presented in the log-scale. Original values are given in ppm and are listed in Appendix B.

### 7.1.4 Hydrothermal alteration

The alteration mineral assemblages at Alvsvågen is composed of chlorite, amphibole, biotite, epidote and quartz. The mineralized micro-gabbro (sample 20ALS7S1) and mineralized gabbro hosted by the shear zone (sample 20ALS11) show strong signs of chloritization and silicification together with a significant enrichment in copper (Table 3). These features indicate that the samples have been altered by the Cu bearing hydrothermal fluids. Enrichment in $SiO_2$ (Figure 28A) in both the gabbroic samples suggests that both samples have been affected by silicification as is also recognized from microscopic observations (Figure 33A, B) by comparing the barren gabbro (sample 20ALS9; Figure 33A) with the mineralized gabbro (sample 20ALS10C; Figure 33B). Microscopic observations infer that the sulfides appear in association with chlorite, biotite and epidote (Figure 23B). Chlorite, epidote, silicic and sericite alterations are well known from VMS deposits elsewhere (Bonnet et al., 2007). The former three are abundant at Alvsvågen while sericite has not been observed in any of the Alvsvågen

samples. Saussurite is however abundant and can be comprised of a variable assemblage of minerals (zoisite, epidote, sericite, albite). A suggestion might be made that the saussurite might mask the sericite alteration, thus explaining the absence of sericite in the samples.

From chlorite thermometry the temperature of chlorite formation was found to be in the range of 320 - 400 °C, giving an indication of fluid temperatures for the hydrothermal alteration which coincide with greenschist facies conditions. The temperature does also coincide with the typical fluids in VMS deposits that are thought to feature temperatures in the range of 350-400 °C (Ridley, 2013). The mineral assemblages at Alvsvågen also coincide with the mineral assemblages proposed in Alt et al. (2010) regarding high temperature alteration in sheeted dyke complexes and plutonic rocks by reduced fluids in modern systems. Temperatures from chlorite thermometry must however be applied with care as the ophiolitic rocks have been the subject of greenschist metamorphism during the Caledonian orogeny (Amaliksen, 1983). Several authors emphasize the need for detailed knowledge of coexisting mineral assemblages as to ensure correct results (De and Walshe, 1993; Jowett, 2021). Cathelineau (1988) explains that the relict minerals which are replaced by chlorite can affect the temperatures acquired by chlorite thermometry. Therefore, to support the formation temperatures acquired, a barren gabbro from the Alvsvågen area could be analyzed for reference.

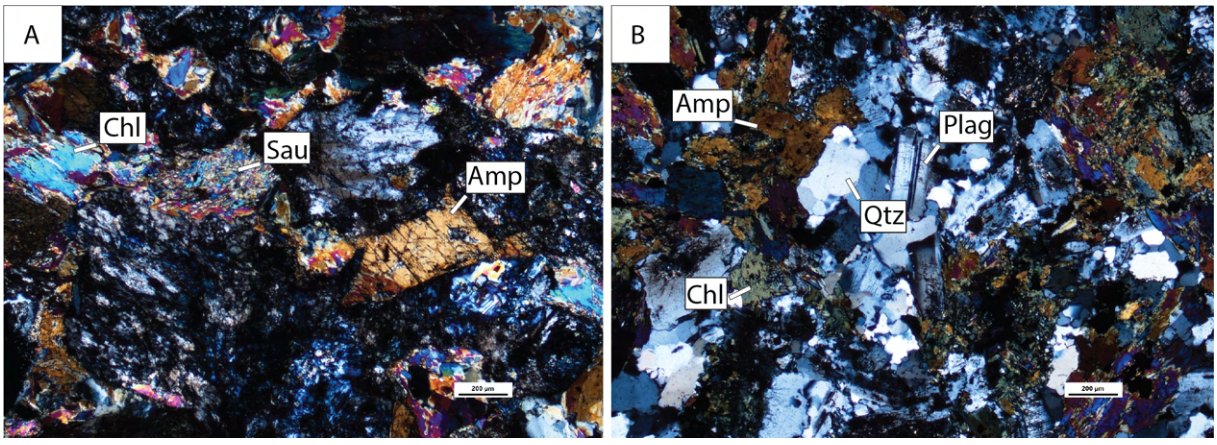


Figure 33: Comparison of (A) the barren layered gabbro 20ALS9 and (B) the mineralized gabbro sample (20ALS10C) showing hydrothermal alteration with silicification. Abbreviations: Abbreviations: Amp - Amphibole, Chl – Chlorite, Plag – Plagioclase, Qtz – Quartz, Sau – Saussurite.

### 7.1.5 Sulfur stable isotope signature

The Alvsvågen deposit show low $\delta^{34}S$ values in the range of +0.04 ‰ to +3.9 ‰ (VCDT) with the mean value of +1.6 ‰. Thermochemical reduction of sulfur will usually display a lower degree of fractionation and a $\delta^{34}S$ signature higher than that recognized from the Alvsvågen

deposit would be expected (Krouse and Coplen, 1997). Thus, thermochemical reduction is considered unlikely for the Alvsvågen deposit. Mantle derived sulfur is assumed to represent $\delta^{34}S$ values of 0 to +2 ‰ (Seal, 2006) and mid-ocean ridge basalts have been found to range between +0.3 ± 2.3 ‰, while gabbro represents values clustering around 0 ‰ (Sakai et al., 1984, Chaussidon et al., 1989, Torssander, 1989). The range of $\delta^{34}S$ values acquired from the Alvsvågen deposit have a mean value of +1.6 ‰ which correlates well with values for primary magmatic sulfur. One outlier is recognized (+3.9 ‰), differing from two other measurements from the same sample which show values of +0.4 and +0.5 ‰.

### 7.1.6 Ore forming model

The Alsvågen mineralization is spatially associated with 4 NW-SE trending shear zones of which two are exposed (Figure 9). The shear zones cut the high-level gabbroic rocks of the Lykling ophiolite which show a subduction related trace element composition and a depletion in LREE indicating a depleted mantle source. The mineralization is primarily Cu-rich, featuring low quantities of other base metals and minor Au content. Copper is contributed from hydrothermal leaching of the gabbroic lithologies by reduced high-temperature fluids (Galley et al., 2007). Fluid temperature is well defined as chlorite thermometry indicate temperatures in the range of 320 – 400 °C, and the alteration mineral assemblages/ore minerals also closely resemble what is recognized from high temperature modern systems (Alt et al., 2010) as well as altered stockworks/stringer zones in ancient deposits (Bonnet et al., 2007; Galley et al., 2007). The Cu contents at Alvsvågen is high but variable, showing ranges between 1 – 10 wt.% (Table 5). Enrichment in some of the fluid mobile elements (Zn, Ag, Cd, In and Sn) in chalcopyrite indicates that Cu was contributed from the rising hydrothermal fluids. High concentrations of Cu are a typical feature for mafic-type VMS deposits as bimodal and felsic type deposits usually show higher enrichment in Pb (Barrie and Hannington, 1999). Typical VMS deposits in Norway do on average exhibit lower Cu contents with an average of 1 – 3 % (Grenne et al., 1999; Hannington et al., 1999). However, this is not directly relatable as the numbers presented from the previously mentioned authors mostly feature the massive sulfide mounds which are not directly relatable to the Alvsvågen deposit. The Alvsvågen deposit show indications of a formation in the deeper crust, which is recognized both through the hosting high-level gabbros and sulfur isotopic signatures. A magmatic source for sulfur is recognized from Alvsvågen with low $\delta^{34}S$ values in the range of +0.04 ‰ to +3.9 ‰ (VCDT) (Seal, 2006),

inferring that the mineralization formed below the influence of the seawater sulfate of which higher $\delta^{34}S$ values would be expected (Seal, 2006).

Some uncertainties remain about the genesis of the Cu mineralization Alvsvågen. The deposit is epigenetic in its character as the mineralization is hosted in association with shear zones. As the proposed fluid temperature, stratigraphical indications and sulfur isotopes indicate a deeper formation. One suggestion is that the shear zone represents the lower fluid conduits for a VMS system. This is supported by the association with the layered and the high-level gabbroic lithologies as well the proposed ore forming temperature, resembling what is believed to represent the high-temperature reaction zone (Ridley, 2013). The mineral alteration assemblage can also be suggested to support the model, resembling typical alteration related to the high temperatures in VMS deposits (Bonnet el al., 2007; Galley et al., 2007; Alt et al., 2010). However, these features do reflect the temperatures of fluids affecting the altered rock and do not directly prove the model as the fluids originally could have another origin. The Sunnhordaland batholith is located within close proximity to the deposit and felsic intrusions are recognized at Alvsvågen. The batholith might represent the heat source driving the hydrothermal circulation. Bases on this, a model similar to porphyry deposits (Sillitoe, 2010) might be inferred with the shear zone forming as a result of the intrusion channeling fluids as a result of devolatilization. Based on the evidence previously discussed, the former model appears as more likely, however a formation related to the formation of the batholith cannot be discarded to its entirety.

## 7.2 The Lindøya deposit

### 7.2.1 Geotectonic environment of the Lindøya area

The barren micro-gabbro sample (20LIND5) is characterized by enrichment in Th, U and Sr and minor depletion in, Nb, Ta, Zr and Hf (Figure 30A) and a tholeiitic character is suggested (Figure 28B). The REE patterns indicate a slightly depleted mantle source similar to MORB (Sun and McDonough, 1989). In regard to trace element patterns, the Lindøya micro-gabbro show strong similarities to the ophiolitic micro-gabbro (sample 20ALS7B) from the Alvsvågen area (Figure 34). The trace element patterns appear almost identical with minor variation in the degree of enrichment/depletion of some elements. A similar geotectonic environment as Alvsvågen with an SSZ related back-arc basin is therefore inferred for the Lindøya micro-gabbro. The micro-gabbro is enveloped by trondhjemite which is characterized by a calc-alkaline trace element composition (Viken, 2017; Saltvedt, in prep.). Similar geochemical characteristics are also recognized for the basaltic dykes cutting the island in a similar orientation as the micro-gabbro/basalt and is interpreted by Viken (2017) to be related to the Siggjo Complex. From REE patterns the previously mentioned rocks exhibit a strong depletion in Eu which is also the case for the Geitung Unit (Saltvedt, in prep.). Depletion in Eu is not recognized in the micro-gabbro from Lindøya or the ophiolitic rocks from Alvsvågen. Hence, the micro-gabbro at Lindøya is likely to related to the ophiolitic lithologies. Although a connection can be made it does not place the mineralization in direct association with the ophiolitic rocks as the micro-gabbro is not directly associated with the basalt hosted ore body. From this the formation of the deposit is linked to the formation of the ophiolitic, immature island-arc and trondhjemite lithologies which formed ~ 485 - 494 Ma (Pedersen et al., 1997; Viken, 2017; Saltvedt, in prep.). The Lykling ophiolite cannot be directly associated with the ages provided for the other units as it has not been dated directly, but the spatial association can be inferred through stratigraphic relations and trace element composition with the Lindøya micro-gabbro.

One thing the author finds troubling in regard to the proposed geotectonic and later deposit forming model is the volumes of trondhjemite intrusions in proximity to the deposit. Clear stratigraphic relations are not well known as limited field work has been conducted. Geochemical indices separate the trondhjemite and basaltic dykes from the micro-gabbro, however the latter is not directly associated with the mineralization. Therefore, to confirm a possible link to the ophiolitic/island-arc lithologies geochemistry of the basalt should be

acquired. A possibility is that the intruding trondhjemite acted as the heat source for hydrothermal circulation. Felsic intrusions associated with VMS deposits are recognized in both the Fundsjø area and Gjersvik deposits in Norway (Grenne et al., 1999, Pedersen, 1979). The former is associated with tonalitic intrusions (490 Ma) and the latter with quartz diorite and gabbro (483 Ma) (Grenne et al., 1999), and correlate well in time with the trondhjemite on Lindøya which have an age of 485 ± 6 (Saltvedt, in prep.). Both deposits can possibly be used as analogies for Lindøya, and one possible scenario is that the trondhjemite intruded to a larger degree at Bømlo, affecting or assimilating parts of the VMS, or that hydrothermal circulation was driven by the intruding body.

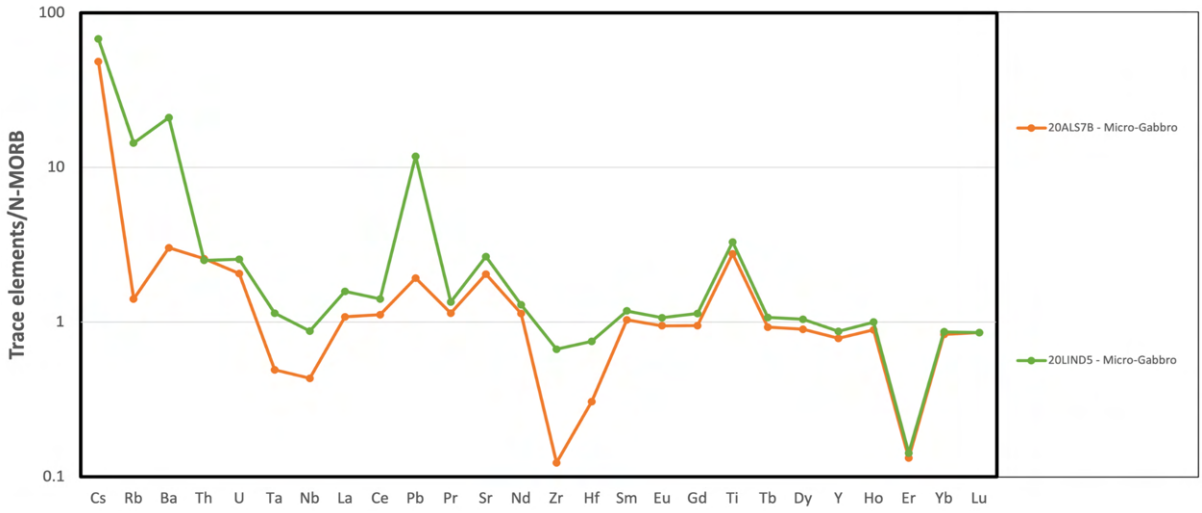


Figure 34: Spider diagrams comparing the trace element compositions of the two micro-gabbroic lithologies from Alvsvågen (20ALS7B) and Lindøya (20LIND5).

### 7.2.2 Mineral assemblages and mineral paragenesis

The Lindøya mineralization occurs as massive sulfides and as veins/disseminations in basalt. The mineral assemblages are characterized by pyrite and pyrrhotite with minor amounts of sphalerite, chalcopyrite, magnetite and in the basalt hosted mineralization, arsenopyrite (Table 11). The massive sulfide is characterized by alternating primary pyrite and pyrrhotite/pyrite rich layering in a silica rich matrix (Figure 35). Faults and soft deformation structures cut the layering often hosting larger grains of sulfides (Figure 35). The larger sulfide grains contain higher contents of both base metal sulfides (chalcopyrite and sphalerite) together with magnetite and are interpreted to be the result of recrystallization at a later stage as a result of deformation and/or metamorphism. According to Galley et al. (2007) recrystallization and deformation in massive sulfides is a common feature in association with regional metamorphic and deformational events. This comes as a result of the ductile nature of massive sulfide bodies and are not as commonly recognized in the more resistant volcanic rocks. The layering in the

massive sulfide mineralization can also have formed as a result of dynamic recrystallization during regional metamorphism (Galley et al., 2007). However, as recrystallization is recognized from the recrystallized larger sulfide grains and deformation from the folding/faulting features cutting the layering this appears as unlikely. As the result, the layering is interpreted as to be primary. Recognized in association with the deposit are also a sulfide poor chert-like lithology which most likely represents amorphous silica derived from the hydrothermal fluids.

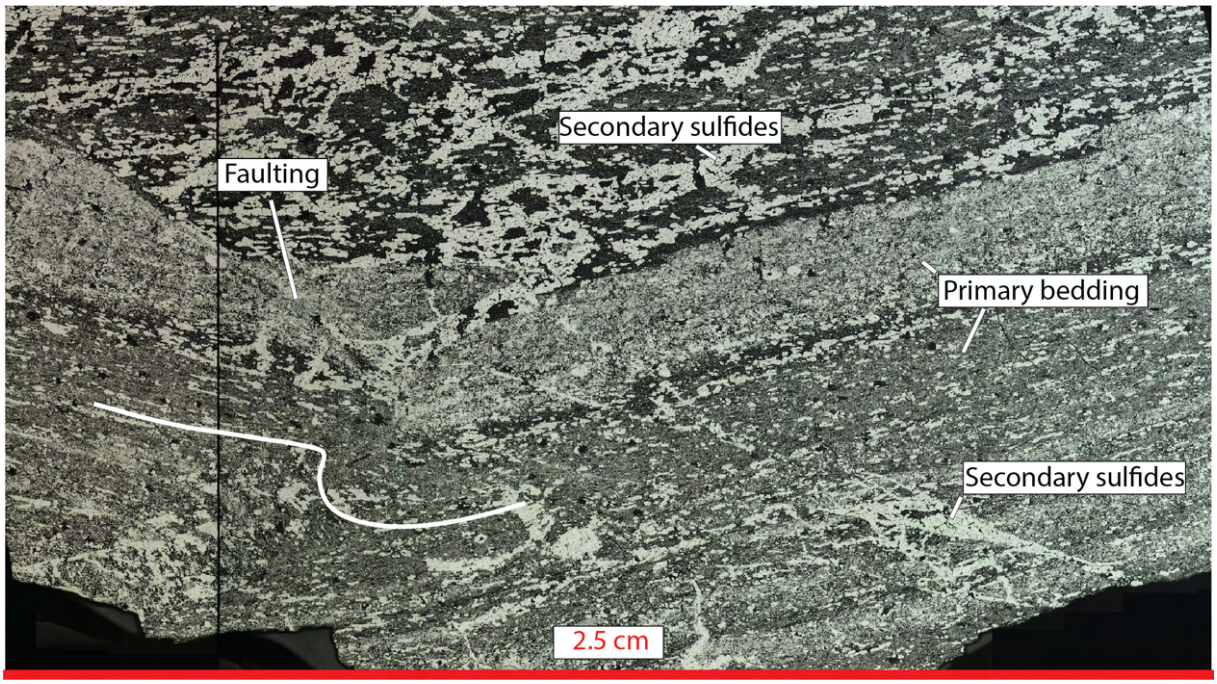


Figure 35: Mosaic of the bedded mineralization 20LIND4B under RLM for illustration. The white line in the lower left corner represents ductile deformation following the layering. The scale is represented by the red line being 2.5 cm.

The basalt hosted mineralization shows no such deformation features and sulfides are associated with chloritic alteration along mineralized veins and as disseminations (Figure 26B). Determining the paragenesis of the mineralization is trying as many of the sulfides appears as heavily weathered. However, as the layered massive mineralization show signs of recrystallization it is safe to assume that the basalt hosted mineralization has gone through similar thermal and/or deformational events. Euhedral pyrite and arsenopyrite appears with sharp contacts towards the other phases and exhibit considerably larger grain sizes (Figure 26F) and is interpreted to have formed as a result of recrystallization.

### 7.2.3 Sulfur isotopic signature of sulfide minerals

The basalt and massive sulfide mineralization at Lindøya exhibit $\delta^{34}S$ isotopic values in the range of +4.9 ‰ to +5.9 ‰ (V-CDT) (Table 6). These relatively heavy isotopic signatures most likely represent thermochemical reduction of seawater sulfate as the main source of sulfur (Seal,

2006) combined with $H_2S$ from combined hydrolysis of rock sulfides and sulfide reduction as a result of reactions with ferrous minerals in the oceanic crust (Shanks III, 2001). The basalt hosted part of the system represents the lowest $\delta^{34}S$ value (+4.9 ‰) compared to the massive mineralization which exhibit more uniform $\delta^{34}S$ values of +5.7 to +5.9 ‰. Sulfur $\delta^{34}S$ values for the Lindøya deposits coincide with values from Cu-Zn VMS deposits (Guldberg/Hysstad deposits; Figure 8) which are hosted in the Langevåg Group having $\delta^{34}S$ values in the range of +4 ‰ (Grenne and Slack, 2019).

### 7.2.4 Ore-forming model

The mineralization at Lindøya is hosted in basalts in association with micro-gabbros and trondhjemite. The stratigraphical relations are not clear as is discussed previously, however with some certainty the formation can be attributed to either an ophiolitic (Lykling ophiolite) or an immature island-arc geotectonic setting (Geitung Unit). Exhalative sulfide iron formations are described as sulfidic black chert-like lithologies (Spry et al., 2000) with a low base metal content (Raaness et al., 2020). Base metal contents in the Lindøya deposit are low (Table 5) and microscopic observations support this suggestion, as rare base metal sulfides recognized in the primary layered mineralization. As Fe contents are 30.61 wt.%, S >30 wt.% and all other major rock forming elements are present only in low quantities, one can assume that much of the remaining mass consist of silica as is also recognized from SEM-EDS elemental maps (Figure 26D). On the basis of these observations and assumptions along with that layering is a common feature in exhalatives which often display fine laminated layers of alternating mineral phases in a silica rich matrix (Spry et al., 2000; Peter, 2003) an exhalative VMS model for the main massive sulfide mineralization is proposed.

A depositional model similar to the Litlabø exhalative (Section 7.4.3) with bacterial reduction as a driver for sulfide deposition (Grenne and Slack, 2019) are discarded by the sulfur isotopic signatures as a strongly depleted signature would be expected (Seal, 2006). The isotopic values for Lindøya show signatures indicating thermochemical reduction of seawater sulfur as the main source of sulfur indicating that the sulfur was provided by hydrothermal venting. According to Bekker et al. (2010) the redox state of the ocean controls the deposition of exhalatives. In the case of the Lindøya deposit, $Fe/H_2S$ ratios in the ocean likely allowed for immediate precipitation vent derived iron together with silica, indicating an $H_2S$ rich anoxic environment. The variation seen in the bedding with different phases alternating (Figure 35) can reflect the redox state of the ocean were sulfides are deposited in $H_2S$ rich seawater while

more silica rich layers/lithologies are precipitated during more anoxic, $H_2S$ poor conditions (Bekker et al., 2010). Chert-like silica rich exhalatives are also known to occur above massive sulfide mounds, and is thought to play an important role in the evolution of deposits by confining heat and promoting zone refining (Slack et al., 2003). According to Spry et al. (2000) several other factor can also affect exhalative deposition with examples as bottom currents, clastic sedimentation, physiochemical conditions and the degree of basin isolation. The proximity to the venting might also be inferred from the chloritic alteration and sulfide mineralization recognized in the basalts at Lindøya. These can resemble the alteration zone associated with stock works/hanging wall recognized in relation to VMS deposits (Galley et al., 2007).

Wulff (1993) also proposes a similar genesis for the Lindøya deposit as well as other similar deposits found in the Geitung Unit. From the Kulleseid II deposit which show identical structural and mineralogical features as Lindøya, Wulff (1993) also notes cross-lamination in one of the samples. Though not directly associated with Lindøya some connection might be inferred from the location and stratigraphical relationships. Another discrepancy is the small size and lack of base metals in the Lindøya deposit which are present in most other Caledonian VMS deposits (Grenne et al., 1999, and sources therein). Low base metal contents are also recognized in most massive deposits hosted within both the Lykling Ophiolite Complex and Geitung Unit (Wulff, 1993). This inconsistency might be explained by a poorly evolved system, poor source of metals, low temperatures of vent fluids or that the parts rich in base metals are poorly exposed on the surface, in the Lindøya deposit.

## 7.3 The Litlabø deposit

### 7.3.1 Geotectonic environment of the Litlabø area

As previously discussed in Chapter 2 "Regional geology", the geotectonic setting of the Litlabø area and the Langevåg Group is the subject of debate. The first possible tectonic setting is the formation of a deepening back-arc basin linked to the to the destruction of the island-arc lithologies (Sivertsen, 1992; Viken, 2017). The second possibility is the formation of a deepening basin following the collapse of the Taconian orogeny. The stratigraphic succession in the Langevåg Group displays an upward transition from subaerial lava and pyroclastic deposits of transitional calc-alkaline/tholeiitic character into submarine pelagic sediments with alkaline pillow lavas (Brekke, 1983) compared to the tholeiitic signature of the Alvsvågen and Lindøya deposits. This does however not put in association with either settings as both feature such traits. For this discussion both settings are applicable as the geotectonic environments represents the possibility of a limited restricted basin.

### 7.3.2 Mineral assemblages and mineral paragenesis

From Litlabø the mineral assemblages are composed of pyrite and pyrrhotite with minor chalcopyrite and sphalerite (Table 11). The massive pyrite mineralization is almost exclusively comprised of pyrite which show tendencies towards layering (Figure 36A). The secondary mineralization is also comprised of pyrite hosted in association with quartz veins which most likely is the result of circulating fluids (Figure 36A). Minor amounts of chalcopyrite and sphalerite are exclusively recognized within the recrystallized veins. The massive pyrrhotite mineralization show a more variable mineral assemblage in comparison and the primary mineralization is bedded pyrrhotite, pyrite and silicates with minor amounts of sphalerite. The secondary mineralization occurs in the veins were the original bedding have been destroyed as a result of deformation (Figure 36B). The veins are also characterized by a more variable mineralogy with chalcopyrite, sphalerite, magnetite and euhedral arsenopyrite. Both types of the mineralizations show signs of deformation and recrystallization even though the original features are preserved in both.

The Litlabø sulfides are categorized as "vasskis" as a result of the low base metal content (Table 5) and adherent mineralogy of mainly pyrite and pyrrhotite. The lack of base metals might be attributed to a distal precipitation from the vent as these was deposited more proximal or in the mound through replacement features (Doyle and Allen, 2003; Galley et al., 2007). In contrast

to the Løkken deposit which show many similarities to the Litlabø deposits, the latter also comprises considerable amounts of pyrrhotite. Grenne and Slack (2019) attributes this variation in mineralogy as a result of lower $fO_2$ conditions and buffering of organic matter which precipitate pyrrhotite over pyrite. This interpretation is also supported by a higher content of organic matter in the Litlabø deposit contrary to the similar Løkken deposit (Grenne and Slack, 2019). The mineral assemblages (Py, Po and Asp) recognized in the secondary mineralization is a common feature in metamorphosed Fe-sulfides in exhalative mineralizations (Spry et al., 2000).

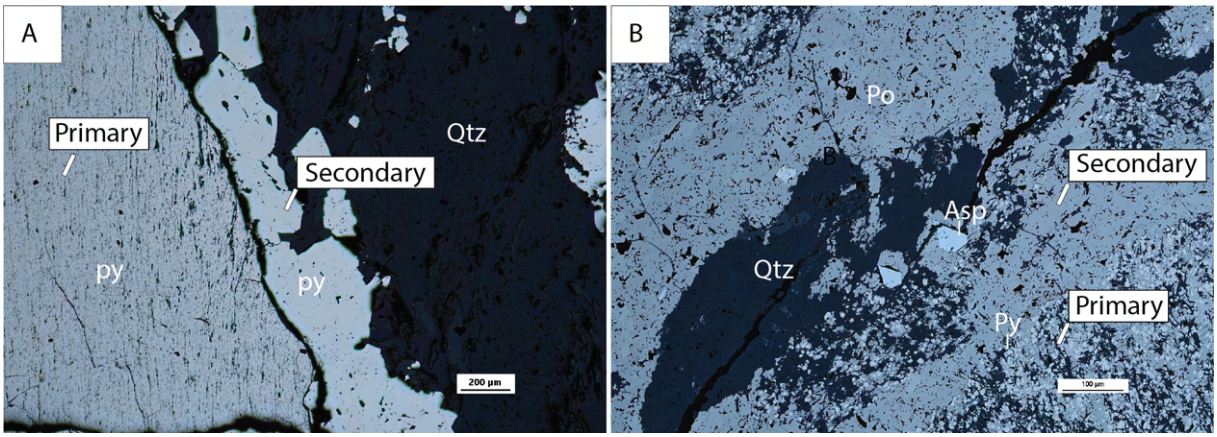


Figure 36: Microphotographs of the Litlabø samples illustrating the metamorphic remobilization of sulfides under RLM. Abbreviations: Po – Pyrrhotite, Py – Pyrite, Asp – Arsenopyrite, Qtz – Quartz.

From LA-ICP-MS, enrichment in the redox sensitive elements (Mn, Mo, V and U) are recognized in Litlabø (Figure 37). Enrichment of redox sensitive elements have been linked to anoxic/euxinic conditions in black shales (Tribovillard et al., 2006) and similar black shale lithologies are found in close association to the massive sulfides at Litlabø. This is due to the fact that the redox sensitive elements are less soluble in anoxic/euxinic conditions contrary to oxic seawater conditions (Tribovillard et al., 2006). Grenne and Slack (2019) also suggests an enrichment in U, Mo and V from bulk analysis of the iron formations, but lower than what is common for black shales in euxinic seawater conditions. If these enrichment features typical for the black shales can be directly correlated with the massive sulfides is uncertain, though similar depositional conditions for pyrite from the water column might be inferred. High Zn and Cd concentrations (Zn; 24000 – 27000 ppm, Cd; 164 – 1376 ppm) are recognized in the secondary pyrite are likely to represent micro-inclusions of sphalerite (Gregory et al., 2015). This enrichment in the secondary pyrite/pyrrhotite is also recognized in Cu (~ 8000 ppm) and Mn (~ 200-1200 ppm) confirming the higher base metal content. Arsenic is also enriched in all

pyrite (~ 500 – 1000 ppm) which is common as As substitutes for Fe and S in the pyrite crystal lattice, which is confirmed by the lack of enrichment in pyrrhotite (37.33 ppm).

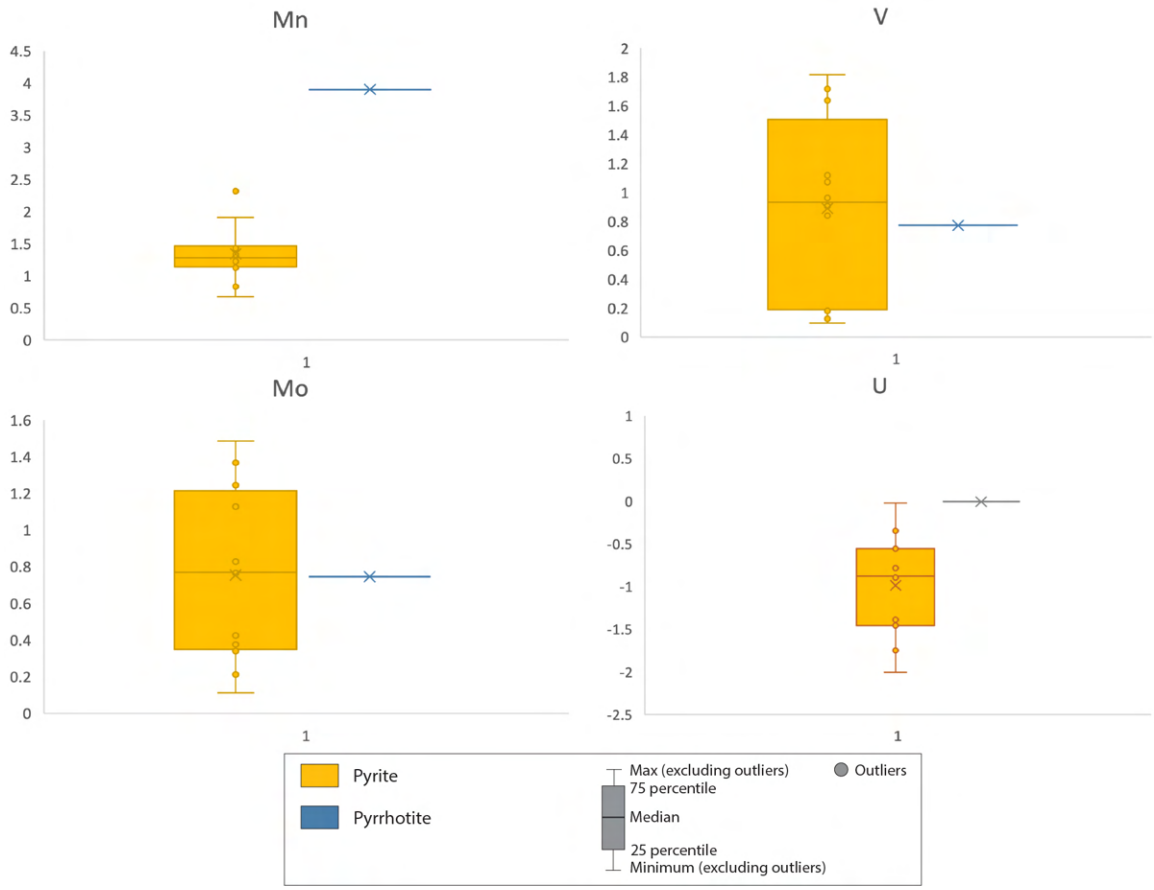


Figure 37: Boxplots of Mn, V, Mo and U from Litlabø from sulfide minerals analyzed with LA-ICP-MS. All values were recalculated to log (10) values as to make them more representable in the boxplots. Original values are given in ppm (Appendix B).

### 7.3.3 Sulfur isotopic signature

The massive mineralizations in Litlabø show rather uniform $\delta^{34}S$ isotopic values between both the pyrite and pyrrhotite rich mineralizations. Isotopic values are in the range of -19.7‰ and -15.7‰ (V-CDT) indicating a strong influence of bacterial reduction of seawater sulfate (Seal, 2006). This isotopic signature is attributed to several conditions, among them lower temperatures and a anoxic/euxinic environment in either the water column or the sediments (Seal, 2006). Previously, sulfur isotopes from the Litlabø deposit have been determined and compared to the Løkken deposit by Grenne and Slack (2019) in regard to depositional conditions of both Fe-silicate beds and the massive sulfides. From the Løkken deposit $\delta^{34}S$ are in the range of -25.3‰ and -18.8 ‰ and from the Litlabø deposit values in the range of -16.0‰ to -15.1 ‰ and are both attributed to bacterial reduction in anoxic/euxinic sea water conditions (Grenne and Slack, 2019)

### 7.3.4 Ore-forming model

The ore forming model proposed for the massive sulfides at Litlabø are exhalatives with biological reduction of seawater sulfur as the main source of reduced sulfur (Figure 37). Reflecting this depositional environment is a significant depletion of $\delta^{34}S$ in the deposit (Table 6). This leads to several indications of an anoxic/euxinic environment were a high $Fe/H_2S$ ratio prohibits the immediate deposition of vent derived iron as a reducing agent is lacking (Shanks III, 2001). Dissolved iron will under these conditions remain in solution within the hydrothermal plume and is deposited distally (Bekker et al., 2010). When bacterial derived $H_2S$ is available as a reducing agent, iron sulfides precipitate from the hydrothermal plume. From Grenne and Slack, (2019) the water column is described as anoxic and at times euxinic. Circulation with the overlaying water column contributes seawater sulfate to the lower parts which feeds the system. In periods of anoxic water compositions, jasper is mainly deposited with sulfides mainly being deposited during more euxinic conditions when $H_2S$ is readily available. Black shales are also found in close association with the massive sulfides at Litlabø, and similar lithologies elsewhere have been proposed to represent the same euxinic/anoxic conditions (Van Houten and Arthur, 1989). All mentioned lithologies are present at the Litlabø deposit inferring a continuously changing ocean chemistry. The formation of such anoxic/euxinic conditions as is referred can be attributed to low sulfate concentrations in the Early Ordovician seawater (Thompson and Kah, 2012) and/or isolated basins with limited circulation. These conditions can be correlated with the proposed geotectonic environments for the Langevåg Group that is thought to represent a back-arc basin. The temporal association with other Cu-Zn VMS deposits (Guldberg/Hysstad deposits; Figure 8) (Raaness et al., 2020) also confirms the presence of other hydrothermal systems in the Langevåg Group. However, no direct connection can be made as the deposits are hosted in stratigraphically separate parts of the succession. The Løkken deposit show similar stratigraphic and geochemical characteristics and are directly associated with the massive sulfide mound (Grenne and Slack, 2005, Grenne and Slack, 2019). Other similar deposits with massive sulfide formations (“vasskis”) in association with jaspers are hosted within the Scandinavian Caledonides (Grenne et al., 1999). These are described as iron formations and are mainly located in association with the massive sulfide bodies (Reinsbakken, 1992, Grenne et al., 1995). The massive sulfide mound associated with Cu-Zn-Pb rich mineralizations is missing in the Litlabø deposit, which infer an even more distal deposition.

## 7.4 Comparison of the studied types of VMS deposits

### 7.4.1 Mineralogical and geochemical comparison

Table 11: Visualization of the mineral assemblages for all deposits. **X**: Main mineral phases, x: Minor mineral phases. Abbreviations: Py – Pyrite, Po – Pyrrhotite, Cpy – Chalcopyrite, Sph – Sphalerite, Mt – Magnetite, Tit – Titanite, Ilm – Ilmenite, Asp – Arsenopyrite, Cub – Cubanite.

| **Deposit** | **Mineralization** | Py | Po | Cpy | Sph | Mt | Tit | Ilm | Asp | Cub | Fe-oxide |
|---|---|---|---|---|---|---|---|---|---|---|---|
| **Alvsvågen** | Gabbro | x | **X** | **X** | x | | **X** | **X** | | | x |
| | Shear zone | **X** | **X** | **X** | x | | x | | | x | x |
| **Lindøya** | Massive sulfide | **X** | **X** | **X** | x | x | | | | | x |
| | Basalt | **X** | **X** | x | x | x | | | x | | x |
| **Litlabø** | Massive pyrite | **X** | | x | | | | | | | |
| | Massive pyrrhotite | **X** | **X** | x | x | x | | | x | | |

Although all three deposits investigated on Bømlo and Stord are classified as VMS deposits, they show different mineral, geochemical and stable isotope characteristics reflecting different ore forming conditions. Both the Alvsvågen and Lindøya gabbros show highly similar geochemical characteristics with a tholeiitic, subduction related trace element composition and depleted REE mantle source signature while the rock from the Langevåg Group show a transitional tholeiitic to calc-alkaline composition (Amaliksen, 1983; Viken, 2017). The Alvsvågen deposit formed from high temperature fluids depositing Cu as chalcopyrite and rare cubanite in shear zones and surrounding gabbroic rocks. On the other hand, the Lindøya and Litlabø deposits are base metal poor and host mainly Fe-sulfides in association with Fe-oxides and silicates (Table 11). Both deposits are mainly exhalatives but show vast differences in in depositional characteristics and appearance. At Lindøya, the exhalatives are deposited in close association to the vent and sulfides hosted as veinlets in basalt. The volcano-sedimentary hosted Litlabø deposit formed distally from the venting from plume fallout and show a greater variation in mineralogy with both pyrite and pyrrhotite rich mineralizations. These massive sulfides at Litlabø also have a higher content of sulfides. From the sulfur isotopic signatures, the differences in ore forming conditions are evident (Figure 38) reflecting the respective depositional environments. Alvsvågen have a magmatic source of sulfur that indicate a deeper formation beyond the reach of seawater influence while Lindøya have thermochemical reduction of seawater sulfur as the main source of sulfur which is more similar to the typical VMS deposits. Litlabø show vastly different isotopic signatures with low temperature bacterial reduction of seawater sulfate as the main source. The different depositional characteristics are also recognized from trace and minor element compositions with the hydrothermal Alvsvågen

showing enrichment in fluid mobile elements while the sedimentary Litlabø deposit is enriched in redox sensitive elements reflecting the ocean chemistry.

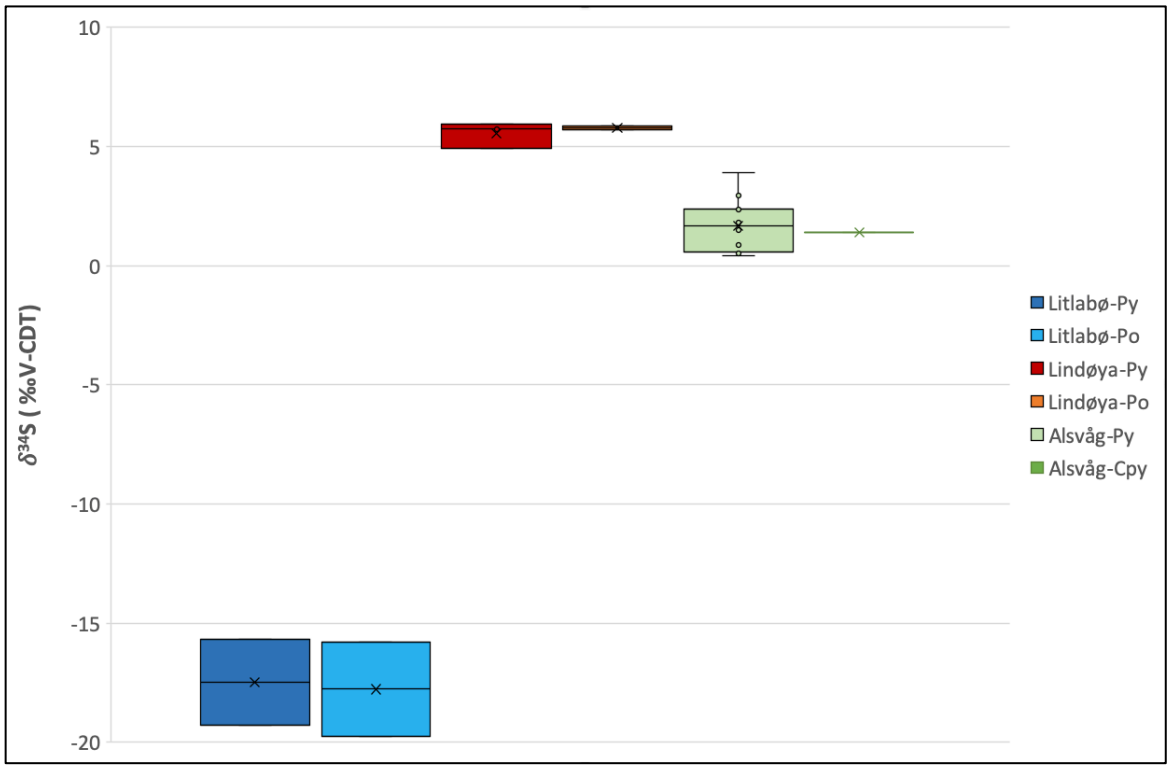


Figure 38: Box-plot visualizing the $\delta^{34}S$ values of the analyzed samples from the different localities.

### 7.4.2 Characterization and relative timing of deposits

A formation model for each deposit is proposed in Figure 38. Based on these observations and the deposits place in the stratigraphy, a division of deposition in time and space is partially possible. The Alvsvågen deposit timing and general placement is uncertain as no other similar deposits are hosted within the Sunnhordaland area or found in the overall literature. However, from the data presented in this thesis a formation as a lower part of a VMS system in association to the Lykling Ophiolite Complex is likely. The Lindøya deposit show similarities to mafic-type deposits as it is hosted in association with gabbro and basalts most likely related to the Lykling ophiolite. One possibly is that the systems similar to what is observed at Alvsvågen acted as conduits for deposits like Lindøya. However, as Wulff (1993) notes several similar deposits are also hosted within the Geitung Unit, and the Lindøya deposit might therefore be linked to the immature island-arc lithologies. To resolve this question further field work must be conducted to clearly lay out the stratigraphical relations. The Litlabø deposit is disconnected from the other deposits in space by the Sunnhordaland Fault (Andersen and Jansen, 1987a). As the time of formation of the Langevåg Group is the subject of debate with two possible

formational settings, both representing restricted basins. Formation can be either as a back-arc basin related to the destruction of an island-arc (Sivertsen, 1992; Viken, 2017) or as a deepening continental basin related to the collapse of the Taconian orogeny (Pedersen 2021, personal communication). Compared to other deposits in Norway, the Litlabø deposit, which is hosted in the same stratigraphic units as Cu-Zn deposits show greater likeness towards the likes of the Løkken, Grong and Folldal deposits (Grenne et al., 1999). Base metals are only recognized in minor quantities in the ophiolite and island-arc lithologies as is recognized at Lindøya. One thing Wulff (1993) also notes are the variation in size of deposits with the Bømlo deposits being minor compared to those hosted on Stord and in Hardangerfjorden in general. Similar deposits are also hosted in Iapetus ocean lithologies in Newfoundland which are also interpreted to be hosted in island-arc and back-arc related lithologies (Piercey et al., 2007). These deposits do however have a higher content of base metal sulfides and show a larger likeness towards the Langevåg Group/Hardangerfjorden deposits.

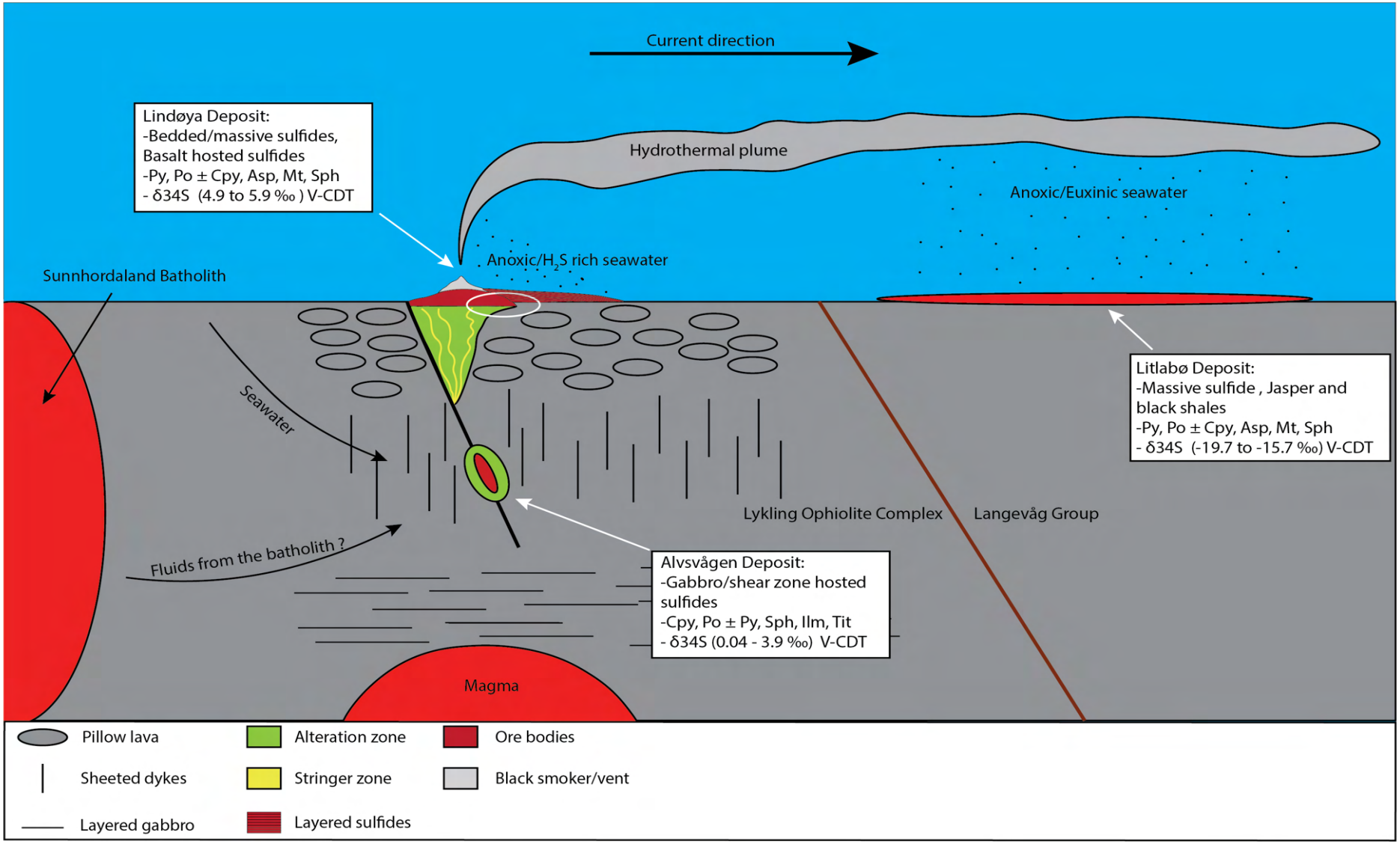


Figure 38: Depositional model for the Alvsvågen, Lindøya and Litlabø deposits. In the model the deposits are put in association. To be emphasized is that the deposits are separated in both space and/or time.

# 8 Conclusion

The results from the present study have brought forward new knowledge about geochemical, mineralogical, stable isotope and trace elements for the Alvsvågen, Lindøya and Litlabø deposits in the Bømlo and Stord areas, the Sunnhordaland region, SW Norway:

- The mineralization at the Alvsvågen deposit is predominantly hosted by four NW-SW trending shear zones which are hosted by the high-level gabbroic rocks of the Lykling Ophiolite complex. The host gabbroic rocks have a tholeiitic character and their trace element characteristics and REE patterns reflect a depleted mantle source and the formation related to a SSZ setting.
- The main commodity in the Alvsvågen deposit is Cu. The mineral assemblage is predominantly composed of chalcopyrite, pyrrhotite, pyrite with minor amounts of sphalerite, cubanite, titanite and ilmenite. The sulfur isotope composition of sulfides indicates a magmatic source of sulfur. Trace element composition of sulfide phases reveals an enrichment in chalcophile and fluid mobile elements (Zn, Ag, Cd, In and Sn) and Co.

- The Lindøya deposit is hosted by basalts and associated micro-gabbro of the Lykling Ophiolite Complex. The geochemical signature of the tholeiitic micro-gabbro suggests a depleted mantle source and SSZ related formational setting similar to the Alvsvågen high-level gabbro.
- The main mineral assemblages are composed of pyrite and pyrrhotite with minor amounts of base metal sulfides. The mineralization appears as both layered massive sulfides and sulfides hosted as disseminations and veinlets in basalt. The mineralization is separated into a primary and secondary. The obtained sulfur isotope data infers that thermochemical reduction of seawater sulfate was the main source of sulfur.
- The model proposed for the formation is as a vent proximal exhalatives with the basalt possibly represent the alteration halo/stock works. The relative timing of deposition is linked to the Lykling Ophiolite Complex and/or the Geitung Unit.

- The massive sulfide mineralization at the Litlabø deposit is hosted by a volcano-sedimentary sequence composed of black shales, siliciclastic sediments, and greenstones (basalts). The sequence was deposited in a back-arc basin.

- The main mineral assemblages are composed of pyrite and pyrrhotite with minor amounts of base metal sulfides. The primary mineralization is bedded massive pyrite and pyrrhotite and the secondary mineralization is attributed to deformation. Sulfur isotopes infers that bacterial reduction of seawater sulfate was the main source of sulfur. The sulfides are enriched in redox sensitive trace elements (V, Mn, Mo and U) and pyrrhotite contains inclusions of sphalerite.
- The model proposed for formation of the deposit is as exhalatives deposited distally from the vent in a restricted basin in euxinic/anoxic conditions.

## Further work

In the Alvsvågen area further structural analyses are needed with an aim to shed light onto the origin of the ore-bearing shear zones. A more detail hydrothermal alteration analysis may distinguish P-T-X characteristics of the regional metamorphism from the ore-bearing hydrothermal event.

In the Lindøya deposit, a detailed fieldwork would shed light on the stratigraphical relations between the basalt, micro-gabbro and trondhjemite. Geochemical analyses of the basalt along with trace element composition of sulfides should also be acquired whereas they have not been obtained in this thesis due to analytical problems.

In the Litlabø deposit a depositional model is well defined. However, geochemical analysis of the black shales should be acquired for comparison with the massive sulfides. The temporally associated Cu-Zn deposits in the Langevåg Group should also be analyzed for their trace element and sulfur isotope analyses with an aim to refine the regional genetical model for this type of sulfide mineralization.

# References

ALT, J. C., LAVERNE, C., COGGON, R. M., TEAGLE, D. A., BANERJEE, N. R., MORGAN, S., SMITH-DUQUE, C. E., HARRIS, M. & GALLI, L. 2010. Subsurface structure of a submarine hydrothermal system in ocean crust formed at the East Pacific Rise, ODP/IODP Site 1256. *Geochemistry, Geophysics, Geosystems,* 11.

AMALIKSEN, K. 1983. *The geology of the Lvkling Ophiolitic Complex, Bømlo, SW Norway Unpubl. Cand. real.* thesis, Univ. Bergen.

ANDERSEN, T. B. & JANSEN, Ø. J. 1987a. The Sunnhordland Batholith, W. Norway; regional setting and internal structure, with emphasis on the granitoid plutons. *Norsk Geologisk Tidsskrift,* 67**,** 159-183.

ANDERSEN, T. B. & JANSEN, Ø. J. 1987b. The Sunnhordland Batholith, W. Norway: regional setting and internal structure, with emphasis on the granitoid plutons. *Norsk geologisk tidsskrift,* 67**,** 159-183.

BAKER, E. T. & GERMAN, C. R. 2004. On the global distribution of hydrothermal vent fields. *Mid-Ocean Ridges: Hydrothermal Interactions Between the Lithosphere and Oceans, Geophys. Monogr. Ser,* 148**,** 245-266.

BANNER, J. L. 2004. Radiogenic isotopes: systematics and applications to earth surface processes and chemical stratigraphy. *Earth-Science Reviews,* 65**,** 141-194.

BARRIE, C. & HANNINGTON, M. 1999. Classification of volcanic-associated massive sulfide deposits based on host-rock composition. *Reviews in Economic Geology,* 8**,** 1-11.

BEKKER, A., SLACK, J. F., PLANAVSKY, N., KRAPEZ, B., HOFMANN, A., KONHAUSER, K. O. & ROUXEL, O. J. 2010. Iron formation: the sedimentary product of a complex interplay among mantle, tectonic, oceanic, and biospheric processes. *Economic Geology,* 105**,** 467-508.

BONNET, A.-L., CORRIVEAU, L. & GOODFELLOW, W. 2007. Alteration vectors to metamorphosed hydrothermal systems in gneissic terranes. *Mineral deposits of Canada: a synthesis of major deposit-types, district metallogeny, the evolution of geological provinces, and exploration methods. Edited by WD Goodfellow. Geological Association of Canada, Mineral Deposits Division, Special Publication,* 5**,** 1035-1049.

BREKKE, H. 1983. *The Caledonian geological patterns of Moster and southern Bømlo. Evidence for Lower Palaeozoic magmatic arc development. Unpubl. Cand. real.* thesis, Univ. Bergen.

BREKKE, H., FURNES, H., NORDÅS, J. & HERTOGEN, J. 1984. Lower Palaeozoic convergent plate margin volcanism on Bømlo, SW Norway, and its bearing on the tectonic environments of the Norwegian Caledonides. *Journal of the Geological Society,* 141**,** 1015-1032.

CHAUSSIDON, M., ALBARÈDE, F. & SHEPPARD, S. M. 1989. Sulphur isotope variations in the mantle from ion microprobe analyses of micro-sulphide inclusions. *Earth and Planetary Science Letters,* 92**,** 144-156.

COOK, N., CIOBANU, C. L., GEORGE, L., ZHU, Z.-Y., WADE, B. & EHRIG, K. 2016. Trace element analysis of minerals in magmatic-hydrothermal ores by laser ablation inductively-coupled plasma mass spectrometry: Approaches and opportunities. *Minerals,* 6**,** 111.

DALSEGG, E. 1980. CP- og VLF-målinger Alvsvåg gruve Bømlo, Hordaland. *Norges Geol. Unders,* NGU - rapport nr. 1800/35C.

DE, C. & WALSHE, L. 1993. Chlorite geothermometry: a review. *Clays and clay minerals,* 41**,** 219-239.

DE RONDE, C. E., BAKER, E. T., MASSOTH, G. J., LUPTON, J. E., WRIGHT, I. C., FEELY, R. A. & GREENE, R. R. 2001. Intra-oceanic subduction-related hydrothermal venting, Kermadec volcanic arc, New Zealand. *Earth and Planetary Science Letters,* 193**,** 359-369.

DEDITIUS, A. P., UTSUNOMIYA, S., RENOCK, D., EWING, R. C., RAMANA, C. V., BECKER, U. & KESLER, S. E. 2008. A proposed new type of arsenian pyrite: Composition, nanostructure and geological significance. *Geochimica et Cosmochimica Acta,* 72**,** 2919-2933.

DEHNAVI, A. S., MCFARLANE, C. R., LENTZ, D. R. & WALKER, J. A. 2018. Assessment of pyrite composition by LA-ICP-MS techniques from massive sulfide deposits of the Bathurst Mining Camp, Canada: from textural and chemical evolution to its application as a vectoring tool for the exploration of VMS deposits. *Ore Geology Reviews,* 92**,** 656-671.

DIETRICHSON, B. & FOSLIE, S. 1955. Kisdistriktet Varaldsøy-Ølve i Hardanger og bergverksdriftens historie.

DOYLE, M. G. & ALLEN, R. L. 2003. Subsea-floor replacement in volcanic-hosted massive sulfide deposits. *Ore Geology Reviews,* 23**,** 183-222.

DURAN, C. J., DUBÉ-LOUBERT, H., PAGÉ, P., BARNES, S.-J., ROY, M., SAVARD, D., CAVE, B. J., ARGUIN, J.-P. & MANSUR, E. T. 2019. Applications of trace element chemistry of pyrite and chalcopyrite in glacial sediments to mineral exploration targeting: Example from the Churchill Province, northern Quebec, Canada. *Journal of Geochemical Exploration,* 196**,** 105-130.

FOSLIE, S. 1926. Norges Svovelkisforekomster: Norges Geol. *Unders• kelse***,** 122.

FOSSEN, H. & HURICH, C. A. 2005. The Hardangerfjord Shear Zone in SW Norway and the North Sea: a large-scale low-angle shear zone in the Caledonian crust. *Journal of the Geological Society,* 162**,** 675-687.

FOSSEN, H. & RYKKELID, E. 1992. Postcollisional extension of the Caledonide orogen in Scandinavia: Structural expressions and tectonic significance. *Geology,* 20**,** 737-740.

FRANKLIN, J., GIBSON, H., JONASSON, I. & GALLEY, A. 2005. Volcanogenic massive sulfide deposits. *Economic Geology 100th anniversary volume,* 98**,** 523-560.

FRANKLIN, J., LYDON, J. & SANGSTER, D. 1981. Volcanic-associated massive sulfide deposits. *Economic Geology,* 75th Anniversary Volume.

FURNES, H., THON, A., NORDÅS, J. & GARMANN, L. B. 1982. Geochemistry of Caledonian metabasalts from some Norwegian ophiolite fragments. *Contributions to Mineralogy and Petrology,* 79**,** 295-307.

GALLEY, A. G., HANNINGTON, M. D. & JONASSON, I. 2007. Volcanogenic massive sulphide deposits. *Geological Association of Canada, Mineral Deposits Division***,** 141-161.

GIBSON, H., ALLEN, R., RIVERIN, G. & LANE, T. The VMS model: Advances and application to exploration targeting. Proceedings of Exploration, 2007. 713-730.

GIBSON, H. L. & WATKINSON, D. H. 1990. Volcanogenic massive sulphide deposits of the Noranda cauldron and shield volcano, Quebec. *Canadian Institute of Mining and Metallurgy,* 43**,** 119-132.

GOODFELLOW, W. D., MCCUTCHEON, S. R. & PETER, J. M. 2003. *Massive sulfide deposits of the Bathurst mining camp, New Brunswick, and northern Maine*, Society of Economic Geologists.

GREGORY, D. D., LARGE, R. R., HALPIN, J. A., BATURINA, E. L., LYONS, T. W., WU, S., DANYUSHEVSKY, L., SACK, P. J., CHAPPAZ, A. & MASLENNIKOV, V. V. 2015. Trace element content of sedimentary pyrite in black shales. *Economic Geology,* 110**,** 1389-1410.

GRENNE, T., BIRKELAND, A., SOLLI, A., HERTOGEN, J., SANDSTAD, J. S. & ERICHSEN, E. 1995. The sequential development of magmatic and ore-forming processes in the Fundsjø Group, Meråker District, central Norway.

GRENNE, T., IHLEN, P. & VOKES, F. 1999. Scandinavian Caledonide metallogeny in a plate tectonic perspective. *Mineralium Deposita,* 34**,** 422-471.

GRENNE, T. & SLACK, J. F. 2005. Geochemistry of Jasper Beds from the Ordovician Løkken Ophiolite, Norway: Origin of Proximal and Distal Siliceous Exhalites. *Economic Geology,* 100**,** 1511-1527.

GRENNE, T. & SLACK, J. F. 2019. Mineralogy and geochemistry of silicate, sulfide, and oxide iron formations in Norway: evidence for fluctuating redox states of early Paleozoic marine basins. *Mineralium Deposita,* 54**,** 829-848.

HANNINGTON, M., HERZIG, P., SCOTT, S., THOMPSON, G. & RONA, P. 1991. Comparative mineralogy and geochemistry of gold-bearing sulfide deposits on the mid-ocean ridges. *Marine geology,* 101**,** 217-248.

HANNINGTON, M. D., DE RONDE, C. D. & PETERSEN, S. 2005. Sea-floor tectonics and submarine hydrothermal systems. Society of Economic Geologists.

HELLAND, A. 1871. *Ertsforekomster i søndhordland og paa karmøen*.

HORIKOSHI, E. 1990. Opening of the Sea of Japan and Kuroko deposit formation. *Mineralium Deposita,* 25**,** 140-145.

HUMPHRIS, S. E. & THOMPSON, G. 1978. Trace element mobility during hydrothermal alteration of oceanic basalts. *Geochimica et Cosmochimica Acta,* 42**,** 127-136.

KOSKI, R. 2012. Hypogene ore characteristics in volcanogenic massive sulfide occurrence model. 2012. *US Geol. Surv***,** 135-146.

KROUSE, H. & COPLEN, T. B. 1997. Reporting of relative sulfur isotope-ratio data (technical report). *Pure and Applied Chemistry,* 69**,** 293-296.

LARGE, R. R. 1992. Australian volcanic-hosted massive sulfide deposits; features, styles, and genetic models. *Economic geology,* 87**,** 471-510.

MACNAMARA, J. & THODE, H. G. 1950. Comparison of the Isotopic Constitution of Terrestrial and Meteoritic Sulfur. *Physical Review,* 78**,** 307-308.

MAKVANDI, S., GHASEMZADEH-BARVARZ, M., BEAUDOIN, G., GRUNSKY, E. C., MCCLENAGHAN, M. B., DUCHESNE, C. & BOUTROY, E. 2016. Partial least squares-discriminant analysis of trace element compositions of magnetite from various VMS deposit subtypes: Application to mineral exploration. *Ore Geology Reviews,* 78**,** 388-408.

MARSHALL, D. 1996. Ternplot: an excel spreadsheet for ternary diagrams. *Computers & Geosciences,* 22**,** 697-699.

MATHIEU, L. 2018. Quantifying hydrothermal alteration: A review of methods. *Geosciences,* 8**,** 245.

MIDDLEMOST, E. A. 1994. Naming materials in the magma/igneous rock system. *Earth-science reviews,* 37**,** 215-224.

NORDÅS, J., AMALIKSEN, K., BREKKE, H., SUTHERN, R., FURNES, H., STURT, B., ROBINS, B. & GEE, D. 1985. Lithostratigraphy and petrochemistry of Caledonian rocks on Bømlo, SW Norway. *The Caledonide Orogen—Scandinavia and Related Areas: New York, John Wiley & Sons Ltd***,** 679-692.

NOVOSELOV, K., BELOGUB, E., KOTLYAROV, V. & MIKHAILOV, A. 2015. Ore mineralogy and formation conditions of the Pirunkoukku gold occurrence (Finland). *European Journal of Mineralogy,* 27**,** 639-649.

O'NEIL, J. R. 1986. Theoretical and experimental aspects of isotopic fractionation. *Reviews in Mineralogy,* 16**,** 1-40.

OHMOTO, H. 1972. Systematics of sulfur and carbon isotopes in hydrothermal ore deposits. *Economic Geology,* 67**,** 551-578.
OHMOTO, H. & LASAGA, A. C. 1982. Kinetics of reactions between aqueous sulfates and sulfides in hydrothermal systems. *Geochimica et Cosmochimica Acta,* 46**,** 1727-1745.
PATTEN, C. G., PITCAIRN, I. K., TEAGLE, D. A. & HARRIS, M. 2016. Mobility of Au and related elements during the hydrothermal alteration of the oceanic crust: implications for the sources of metals in VMS deposits. *Mineralium Deposita,* 51**,** 179-200.
PEARCE, J. A., LIPPARD, S. & ROBERTS, S. 1984. Characteristics and tectonic significance of supra-subduction zone ophiolites. *Geological Society, London, Special Publications,* 16**,** 77-94.
PEDERSEN, R., BRUTON, D. & FURNES, H. 1992. Ordovician faunas, island arcs and ophiolites in the Scandinavian Caledonides. *Terra Nova,* 4**,** 217-222.
PEDERSEN, R.-F., FURNES, H. & DUNNING, G. 1988. Some Norwegian ophiolite complexes reconsidered.
PEDERSEN, R. B. & DUNNING, G. R. 1997. Evolution of arc crust and relations between contrasting sources: U-Pb (age), Nd and Sr isotope systematics of the ophiolitic terrain of SW Norway. *Contributions to Mineralogy and Petrology,* 128**,** 1-15.
PEDERSEN, S. A. S. 1979. Structures and ore genesis of the Grimsdalen sulphide deposits, southern Trondheim Region, Norway. *Norges Geol. Unders,* 351**,** 77-98.
PERFIT, M. R., GUST, D., BENCE, A. E., ARCULUS, R. & TAYLOR, S. R. 1980. Chemical characteristics of island-arc basalts: implications for mantle sources. *Chemical Geology,* 30**,** 227-256.
PETER, J. M. 2003. Ancient iron formations: their genesis and use in the exploration for stratiform base metal sulphide deposits, with examples from the Bathurst Mining Camp. *GeoText,* 4**,** 145-176.
PETER, J. M. & SCOTT, S. D. 1999. Windy Craggy, northwestern British Columbia; the world's largest besshi-type deposit. *Reviews in Economic Geology,* 8**,** 261-295.
PIERCEY, S., PEREIRA, C. & WALSH, D. 2007. Volcanogenic massive sulphide (VMS) deposits of the Newfoundland Appalachians: an overview of their setting, classification, grade-tonnage data, and unresolved questions. *Newfoundland and Labrador Department of Natural Resources, Geological Survey, Report,* 7**,** 169-179.
PIERCEY, S. J., PETER, J. M. & HERRINGTON, R. J. 2015. Zn-rich volcanogenic massive sulphide (VMS) deposits. *Current perspectives on zinc deposits***,** 37-57.
POULSEN, H. & HANNINGTON, M. 1995. Auriferous volcanogenic sulfide deposits. *Geology of Canadian mineral deposit types, Geology of Canada,* 8**,** 183-196.
POULSEN, K. H. 2012. Mineral Deposits and Metallogeny of Fennoscandia. Geological Survey of Finland, Special Paper 53. Society of Economic Geologists.
REES, C., JENKINS, W. & MONSTER, J. 1978. The sulphur isotopic composition of ocean water sulphate. *Geochimica et Cosmochimica Acta,* 42**,** 377-381.
REINSBAKKEN, A. 1992. *The Skorovass volcanogenic massive sulphide deposit: vulcano-stratigraphy, petrochemistry, hydrothermal alteration and paleo-tectonic setting*, Univ.
REUSCH, H. 1888. Bømmeløen og Karmøen med omgivelser. *Geologiska Föreningen i Stockholm Förhandlingar,* 10**,** 392-396.
RIDLEY, J. 2013. *Ore deposit geology*, Cambridge University Press.
ROBERTS, D. 2003. The Scandinavian Caledonides: event chronology, palaeogeographic settings and likely modern analogues. *Tectonophysics,* 365**,** 283-299.
ROBERTS, D., STURT, B. & FURNES, H. 1985. Volcanite assemblages and environments in the Scandinavian Caledonides and the sequential development history of the

mountain belt. *Gee, DG & Sturt, BA (eds.), The Caledonide Orogen–Scandinavian related areas***,** 919-930.

RAANESS, A., WANVIK, J., SCHIELLERUP, H., SANDSTAD, J., KORNELIUSSEN, A., BRÖNNER, M., HELDAL, T., GAUTNEB, H. & NILSSON, L. 2020. Mineralressurser i Vestland fylke.

SAKAI, H., DES MARAIS, D., UEDA, A. & MOORE, J. 1984. Concentrations and isotope ratios of carbon, nitrogen and sulfur in ocean-floor basalts. *Geochimica et Cosmochimica Acta,* 48**,** 2433-2441.

SALTVEDT, S. in prep. The formation of the ophiolitic terrane of SW Norway - relationships between immature island arc sequences and trondhjemitic complexes on Bømlo. *Bergen: Unvierstiy of Bergen*.

SCHEIBER, T., VIOLA, G., WILKINSON, C. M., GANERØD, M., SKÅR, Ø. & GASSER, D. 2016. Direct 40Ar/39Ar dating of Late Ordovician and Silurian brittle faulting in the southwestern Norwegian Caledonides. *Terra Nova,* 28**,** 374-382.

SEAL, R. R. 2006. Sulfur isotope geochemistry of sulfide minerals. *Reviews in mineralogy and geochemistry,* 61**,** 633-677.

SHANKS III, W. C. 2001. Stable isotopes in seafloor hydrothermal systems: vent fluids, hydrothermal deposits, hydrothermal alteration, and microbial processes. *Reviews in Mineralogy and Geochemistry,* 43**,** 469-525.

SHARMAN, E. R., TAYLOR, B. E., MINARIK, W. G., DUBÉ, B. & WING, B. A. 2015. Sulfur isotope and trace element data from ore sulfides in the Noranda district (Abitibi, Canada): Implications for volcanogenic massive sulfide deposit genesis. *Mineralium Deposita,* 50**,** 591-606.

SILLITOE, R. H. 2010. Porphyry copper systems. *Economic geology,* 105**,** 3-41.

SINGER, D. A. 1995. World class base and precious metal deposits; a quantitative analysis. *Economic Geology,* 90**,** 88-104.

SIVERTSEN, J. 1992. *Stratigraphy and geochemistry of the extrusives of the Torvastad Group; marginal basin deposits associated with the Karmøy ophiolite complex, SW Norway. Cand. Scient.* Thesis, Geologisk Institutt, Department A, University of Bergen.

SLACK, J., FOOSE, M. P., FLOHR, M., SCULLY, M. & BELKIN, H. 2003. Exhalative and subsea-floor replacement processes in the formation of the Bald Mountain massive sulfide deposit, northern Maine. *Economic Geology Monograph,* 11**,** 513-547.

SLOTNES, M. S. in prep. Detrital zircon provenance of the Bremnes Migmatite Complex on Bømlo, SW Norway. *Bergen: Unvierstiy of Bergen*.

SPRY, P., PETER, J. & SLACK, J. 2000. Meta-exhalites as exploration guides to ore. *Reviews in Economic Geology,* 11**,** 163-201.

SUN, S.-S. & MCDONOUGH, W. F. 1989. Chemical and isotopic systematics of oceanic basalts: implications for mantle composition and processes. *Geological Society, London, Special Publications,* 42**,** 313-345.

SYME, E. & BAILES, A. 1993. Stratigraphic and tectonic setting of early Proterozoic volcanogenic massive sulfide deposits, Flin Flon, Manitoba. *Economic Geology,* 88**,** 566-589.

TAYLOR, C. D., ZIERENBERG, R. A., GOLDFARB, R. J., KILBURN, J. E., SEAL II, R. R. & KLEINKOPF, M. D. 1995. VOLCANIC-ASSOCIATED MASSIVE SULFIDE DEPOSITS (MODELS 24a-b, 28a; Singer, 1986a, b; Cox, 1986). *Preliminary compilation of descriptive geoenvironmental mineral deposit models***,** 137.

THOMPSON, C. K. & KAH, L. C. 2012. Sulfur isotope evidence for widespread euxinia and a fluctuating oxycline in Early to Middle Ordovician greenhouse oceans. *Palaeogeography, Palaeoclimatology, Palaeoecology,* 313**,** 189-214.

TORSSANDER, P. 1989. Sulfur isotope ratios of Icelandic rocks. *Contributions to Mineralogy and Petrology,* 102**,** 18-23.

TRIBOVILLARD, N., ALGEO, T. J., LYONS, T. & RIBOULLEAU, A. 2006. Trace metals as paleoredox and paleoproductivity proxies: an update. *Chemical geology,* 232**,** 12-32.

VAN ACTHERBERGH, E. 2001. Data reduction software for LA-ICP-MS. *Laser Ablation-ICP-mass spectrometry in the earth sciences: principles and applications***,** 239-243.

VAN HOUTEN, F. & ARTHUR, M. 1989. Temporal patterns among Phanerozoic oolitic ironstones and oceanic anoxia. *Geological Society, London, Special Publications,* 46**,** 33-49.

WULFF, P. W. 1993. En klassikfikation af mineraliseringer på Bømlo, Sunnhordaland, SV-Norge. *Københavns Universitet*.

WULFF, P. W. 1996. En befaring af cirka 100 mineraliseringer i Sunnhordland, SV-Norge. *Norges Geologiske Undersøkelse,* NGU-rapport 96.139

# Appendix A: Chlorite thermometry

Table A1: Overview over standards used as reference during SEM-EDS analysis of chlorite.

| STD | Range | | O | Na | Mg | Al | Si | K | Ca | Ti | Mn | Fe | Ni | Sr | Nb | Ba |
|---|---|---|---|---|---|---|---|---|---|---|---|---|---|---|---|---|
| Fe (Fe) | 6255 | 6541 | 0.01 | | | | | | | | | 99.99 | | | | |
| Jade (Na) | 962 | 1120 | 47.19 | 10.7 | 0.59 | 12.58 | 27.57 | | 1.02 | | | 0.31 | | | | |
| Korondum (Al) | 1403 | 1569 | 47.08 | | | 52.92 | | | | | | | | | | |
| MgO (Mg) | | | 39.69 | | 60.31 | | | | | | | | | | | |
| Mn (Mn) | 5755 | 6035 | 0.01 | | | | | | | | 99.99 | | | | | |
| Ni (Ni) | 7323 | 7631 | 0.01 | | | | | | | | | | 99.99 | | | |
| Orthoclase (K) | 3204 | 3420 | 45.97 | 0.85 | | 9.83 | 30.1 | 12.39 | | | | 0.02 | | 0.03 | | 0.73 |
| Rutile (Ti) | 4386 | 4630 | 39.91 | | | | | | | 59.53 | | 0.29 | | | 0.14 | |
| Wollastonitt (Si) | 1652 | 1828 | 41.11 | | 0.04 | | 23.88 | | 34.46 | | 0.16 | 0.24 | | | | |
| Wollastonitt (Ca) | | | 41.11 | | 0.04 | | 23.88 | | 34.46 | | 0.16 | 0.24 | | | | |

Table A2: Chlorite thermometry calculations based on the geothermometer by Jowett. (2021).

| Elements / Samples | Chlorite 1-1 | Chlorite 3-2 | Chlorite 3-3 | Chlorite 3-4 | Chlorite 3-5 | Chlorite 4-1 | Chlorite 4-2 | Chlorite 5-1 | Chlorite 5-2 |
|---|---|---|---|---|---|---|---|---|---|
| SiO2 | 26.70 | 25.56 | 25.56 | 26.72 | 27.00 | 26.72 | 26.40 | 26.10 | 27.92 |
| TiO2 | | | | | | | | | |
| Al2O3 | 22.14 | 22.24 | 22.24 | 19.95 | 23.90 | 19.95 | 21.03 | 23.54 | 19.86 |
| FeO | 28.17 | 26.67 | 26.67 | 33.65 | 26.51 | 33.65 | 32.45 | 33.95 | 35.20 |
| MnO | | | | | | | | | |
| MgO | 15.64 | 17.23 | 17.23 | 13.27 | 17.40 | 13.27 | 14.34 | 13.58 | 13.32 |
| CaO | | | | | | | | | |
| Na2O | | | | | | | | | |
| K2O | | | | | | | | | |
| BaO | | | | | | | | | |
| Rb2O | | | | | | | | | |
| Cs2O | | | | | | | | | |
| ZnO | | | | | | | | | |
| F | | | | | | | | | |
| Cl | | | | | | | | | |
| Cr2O3 | | | | | | | | | |
| NiO | | | | | | | | | |
| No. of oxygens | 28.00 | 28.00 | 28.00 | 28.00 | 28.00 | 28 | 28 | 28 | 28 |

| Elements / Samples | Chlorite 1-1 | Chlorite 3-2 | Chlorite 3-3 | Chlorite 3-4 | Chlorite 3-5 | Chlorite 4-1 | Chlorite 4-2 | Chlorite 5-1 | Chlorite 5-2 |
|---|---|---|---|---|---|---|---|---|---|
| | 0.00 | 0.00 | 0.00 | 0.00 | 0.00 | 0 | 0 | 0 | 0 |

| | | | | | | | | | |
|---|---|---|---|---|---|---|---|---|---|
| SiO2 | 26.70 | 25.56 | 25.56 | 26.72 | 27.00 | 26.71855109 | 26.39767177 | 26.09818441 | 27.91650053 |
| TiO2 | 0.00 | 0.00 | 0.00 | 0.00 | 0.00 | 0 | 0 | 0 | 0 |
| Al2O3 | 22.14 | 22.24 | 22.24 | 19.95 | 23.90 | 19.95292862 | 21.02993329 | 23.54294419 | 19.85845453 |
| Cr2O3 | 0.00 | 0.00 | 0.00 | 0.00 | 0.00 | 0 | 0 | 0 | 0 |
| Fe2O3 | 0.00 | 0.00 | 0.00 | 0.00 | 0.00 | 0 | 0 | 0 | 0 |
| FeO | 28.17 | 26.67 | 26.67 | 33.65 | 26.51 | 33.65435989 | 32.44506714 | 33.95025067 | 35.19813787 |
| MnO | 0.00 | 0.00 | 0.00 | 0.00 | 0.00 | 0 | 0 | 0 | 0 |
| MgO | 15.64 | 17.23 | 17.23 | 13.27 | 17.40 | 13.26640609 | 14.34430158 | 13.58148323 | 13.31615511 |
| NiO | 0.00 | 0.00 | 0.00 | 0.00 | 0.00 | 0 | 0 | 0 | 0 |
| ZnO | 0.00 | 0.00 | 0.00 | 0.00 | 0.00 | 0 | 0 | 0 | 0 |
| CaO | 0.00 | 0.00 | 0.00 | 0.00 | 0.00 | 0 | 0 | 0 | 0 |
| Na2O | 0.00 | 0.00 | 0.00 | 0.00 | 0.00 | 0 | 0 | 0 | 0 |
| K2O | 0.00 | 0.00 | 0.00 | 0.00 | 0.00 | 0 | 0 | 0 | 0 |
| BaO | 0.00 | 0.00 | 0.00 | 0.00 | 0.00 | 0 | 0 | 0 | 0 |
| Rb2O | 0.00 | 0.00 | 0.00 | 0.00 | 0.00 | 0 | 0 | 0 | 0 |
| F | 0.00 | 0.00 | 0.00 | 0.00 | 0.00 | 0 | 0 | 0 | 0 |
| Cl | 0.00 | 0.00 | 0.00 | 0.00 | 0.00 | 0 | 0 | 0 | 0 |
| H2O* | 11.94 | 11.86 | 11.86 | 11.70 | 12.37 | 11.70459658 | 11.863747 | 12.2034685 | 12.01247656 |
| Total | 104.60 | 103.56 | 103.56 | 105.30 | 107.17 | 105.2968423 | 106.0807208 | 109.376331 | 108.3017246 |
| O=F,Cl | 0.00 | 0.00 | 0.00 | 0.00 | 0.00 | 0 | 0 | 0 | 0 |
| TOTAL | 104.60 | 103.56 | 103.56 | 105.30 | 107.17 | 105.2968423 | 106.0807208 | 109.376331 | 108.3017246 |
| | | | | | | | | | |
| Si | 5.36 | 5.14 | 5.14 | 5.45 | 5.23 | 5.452830683 | 5.307084855 | 5.103331813 | 5.556426499 |
| Al iv | 2.64 | 2.86 | 2.86 | 2.55 | 2.77 | 2.547169317 | 2.692915145 | 2.896668187 | 2.443573501 |
| Al vi | 2.60 | 2.44 | 2.44 | 2.27 | 2.69 | 2.272294549 | 2.318548077 | 2.5574685 | 2.230132855 |
| Ti | 0.00 | 0.00 | 0.00 | 0.00 | 0.00 | 0 | 0 | 0 | 0 |
| Cr | 0.00 | 0.00 | 0.00 | 0.00 | 0.00 | 0 | 0 | 0 | 0 |
| Fe3+ | 0.00 | 0.00 | 0.00 | 0.00 | 0.00 | 0 | 0 | 0 | 0 |
| Fe2+ | 4.75 | 4.66 | 4.66 | 5.86 | 4.33 | 5.858715701 | 5.611726897 | 5.694881912 | 5.947850677 |
| Mn | 0.00 | 0.00 | 0.00 | 0.00 | 0.00 | 0 | 0 | 0 | 0 |
| Mg | 4.68 | 5.16 | 5.16 | 4.04 | 5.02 | 4.036005992 | 4.298918587 | 3.958950929 | 3.950961962 |
| Ni | 0.00 | 0.00 | 0.00 | 0.00 | 0.00 | 0 | 0 | 0 | 0 |
| Zn | 0.00 | 0.00 | 0.00 | 0.00 | 0.00 | 0 | 0 | 0 | 0 |
| Ca | 0.00 | 0.00 | 0.00 | 0.00 | 0.00 | 0 | 0 | 0 | 0 |
| Na | 0.00 | 0.00 | 0.00 | 0.00 | 0.00 | 0 | 0 | 0 | 0 |
| K | 0.00 | 0.00 | 0.00 | 0.00 | 0.00 | 0 | 0 | 0 | 0 |
| Ba | 0.00 | 0.00 | 0.00 | 0.00 | 0.00 | 0 | 0 | 0 | 0 |
| Rb | 0.00 | 0.00 | 0.00 | 0.00 | 0.00 | 0 | 0 | 0 | 0 |
| F | 0.00 | 0.00 | 0.00 | 0.00 | 0.00 | 0 | 0 | 0 | 0 |
| Cl | 0.00 | 0.00 | 0.00 | 0.00 | 0.00 | 0 | 0 | 0 | 0 |
| OH* | 16.00 | 16.00 | 16.00 | 16.00 | 16.00 | 16 | 16 | 16 | 16 |
| Total | 36.03 | 36.26 | 36.26 | 36.17 | 36.05 | 36.16701624 | 36.22919356 | 36.21130134 | 36.12894549 |
| | | | | | | | | | |
| Oxidized | yes | yes | yes | yes | yes | yes | yes | yes | yes |
| Fe/Fe+Mg | 0.50 | 0.47 | 0.47 | 0.59 | 0.46 | 0.592105153 | 0.56623223 | 0.5899089 | 0.600865063 |
| **Variety** | **ripidolite** | **ripidolite** | **ripidolite** | **ripidolite** | **ripidolite** | **ripidolite** | **ripidolite** | **ripidolite** | **ripidolite** |
| | | | | | | | | | |
| Al total | 5.24 | 5.30 | 5.30 | 4.82 | 5.46 | 4.819463866 | 5.011463222 | 5.454136687 | 4.673706356 |
| Al iv (1) | 2.64 | 2.86 | 2.86 | 2.55 | 2.77 | 2.547169317 | 2.692915145 | 2.896668187 | 2.443573501 |

| | | | | | | | | | |
|---|---|---|---|---|---|---|---|---|---|
| Al iv (2) | 2.64 | 2.86 | 2.86 | 2.55 | 2.77 | 2.547169317 | 2.692915145 | 2.896668187 | 2.443573501 |
| Al vi | 2.60 | 2.44 | 2.44 | 2.27 | 2.69 | 2.272294549 | 2.318548077 | 2.5574685 | 2.230132855 |
| Si | 5.36 | 5.14 | 5.14 | 5.45 | 5.23 | 5.452830683 | 5.307084855 | 5.103331813 | 5.556426499 |
| Fe/Fe+Mg | 0.50 | 0.47 | 0.47 | 0.59 | 0.46 | 0.592105153 | 0.56623223 | 0.5899089 | 0.600865063 |
| | | | | | | | | | |
| **Namer** | FALSE | FALSE | FALSE | FALSE | FALSE | FALSE | FALSE | FALSE | FALSE |
| | FALSE | FALSE | FALSE | FALSE | FALSE | FALSE | FALSE | FALSE | FALSE |
| | FALSE | FALSE | FALSE | FALSE | FALSE | FALSE | FALSE | FALSE | FALSE |
| | FALSE | FALSE | FALSE | FALSE | FALSE | FALSE | FALSE | FALSE | FALSE |
| | FALSE | FALSE | FALSE | FALSE | FALSE | FALSE | FALSE | FALSE | FALSE |
| | FALSE | FALSE | FALSE | FALSE | FALSE | FALSE | FALSE | FALSE | FALSE |
| | ripidolite | ripidolite | ripidolite | ripidolite | ripidolite | ripidolite | ripidolite | ripidolite | ripidolite |
| | FALSE | FALSE | FALSE | FALSE | FALSE | FALSE | FALSE | FALSE | FALSE |
| | FALSE | FALSE | FALSE | FALSE | FALSE | FALSE | FALSE | FALSE | FALSE |
| | FALSE | FALSE | FALSE | FALSE | FALSE | FALSE | FALSE | FALSE | FALSE |
| | FALSE | FALSE | FALSE | FALSE | FALSE | FALSE | FALSE | FALSE | FALSE |
| Variety inter | ripidolite | ripidolite | ripidolite | ripidolite | ripidolite | ripidolite | ripidolite | ripidolite | ripidolite |
| Variety final | ripidolite | ripidolite | ripidolite | ripidolite | ripidolite | ripidolite | ripidolite | ripidolite | ripidolite |
| Namer | FALSE | FALSE | FALSE | FALSE | FALSE | FALSE | FALSE | FALSE | FALSE |
| | | | | | | | | | |
| **Anion props. (E)** | | | | | | | | | |
| Si | 0.89 | 0.85 | 0.85 | 0.89 | 0.90 | 0.889284443 | 0.878604486 | 0.868636525 | 0.929156283 |
| Ti | 0.00 | 0.00 | 0.00 | 0.00 | 0.00 | 0 | 0 | 0 | 0 |
| Al | 0.65 | 0.65 | 0.65 | 0.59 | 0.70 | 0.58708107 | 0.618770105 | 0.692711186 | 0.58430133 |
| Cr | 0.00 | 0.00 | 0.00 | 0.00 | 0.00 | 0 | 0 | 0 | 0 |
| Fe3+ | 0.00 | 0.00 | 0.00 | 0.00 | 0.00 | 0 | 0 | 0 | 0 |
| Fe2+ | 0.39 | 0.37 | 0.37 | 0.47 | 0.37 | 0.468397493 | 0.451566697 | 0.472515667 | 0.489883617 |
| Mn | 0.00 | 0.00 | 0.00 | 0.00 | 0.00 | 0 | 0 | 0 | 0 |
| Mg | 0.39 | 0.43 | 0.43 | 0.33 | 0.43 | 0.329109553 | 0.355849704 | 0.336925905 | 0.330343714 |
| Ni | 0.00 | 0.00 | 0.00 | 0.00 | 0.00 | 0 | 0 | 0 | 0 |
| Zn | 0.00 | 0.00 | 0.00 | 0.00 | 0.00 | 0 | 0 | 0 | 0 |
| Ca | 0.00 | 0.00 | 0.00 | 0.00 | 0.00 | 0 | 0 | 0 | 0 |
| Na | 0.00 | 0.00 | 0.00 | 0.00 | 0.00 | 0 | 0 | 0 | 0 |
| K | 0.00 | 0.00 | 0.00 | 0.00 | 0.00 | 0 | 0 | 0 | 0 |
| Ba | 0.00 | 0.00 | 0.00 | 0.00 | 0.00 | 0 | 0 | 0 | 0 |
| Rb | 0.00 | 0.00 | 0.00 | 0.00 | 0.00 | 0 | 0 | 0 | 0 |
| F | 0.00 | 0.00 | 0.00 | 0.00 | 0.00 | 0 | 0 | 0 | 0 |
| Cl | 0.00 | 0.00 | 0.00 | 0.00 | 0.00 | 0 | 0 | 0 | 0 |
| Total | 2.32 | 2.30 | 2.30 | 2.27 | 2.40 | 2.273872559 | 2.304790991 | 2.370789284 | 2.333684944 |
| F,Cl corr | 2.32 | 2.30 | 2.30 | 2.27 | 2.40 | 2.273872559 | 2.304790991 | 2.370789284 | 2.333684944 |
| | | | | | | | | | |
| **Raw cations** | | | | | | | | | |
| Si | 0.44 | 0.43 | 0.43 | 0.44 | 0.45 | 0.444642221 | 0.439302243 | 0.434318263 | 0.464578142 |
| Ti | 0.00 | 0.00 | 0.00 | 0.00 | 0.00 | 0 | 0 | 0 | 0 |
| Al | 0.43 | 0.44 | 0.44 | 0.39 | 0.47 | 0.39138738 | 0.412513403 | 0.461807458 | 0.38953422 |
| Cr | 0.00 | 0.00 | 0.00 | 0.00 | 0.00 | 0 | 0 | 0 | 0 |
| Fe3+ | 0.00 | 0.00 | 0.00 | 0.00 | 0.00 | 0 | 0 | 0 | 0 |
| Fe2+ | 0.39 | 0.37 | 0.37 | 0.47 | 0.37 | 0.468397493 | 0.451566697 | 0.472515667 | 0.489883617 |

| | | | | | | | | | |
|---|---|---|---|---|---|---|---|---|---|
| Mn | 0.00 | 0.00 | 0.00 | 0.00 | 0.00 | 0 | 0 | 0 | 0 |
| Mg | 0.39 | 0.43 | 0.43 | 0.33 | 0.43 | 0.329109553 | 0.355849704 | 0.336925905 | 0.330343714 |
| Ni | 0.00 | 0.00 | 0.00 | 0.00 | 0.00 | 0 | 0 | 0 | 0 |
| Zn | 0.00 | 0.00 | 0.00 | 0.00 | 0.00 | 0 | 0 | 0 | 0 |
| Ca | 0.00 | 0.00 | 0.00 | 0.00 | 0.00 | 0 | 0 | 0 | 0 |
| Na | 0.00 | 0.00 | 0.00 | 0.00 | 0.00 | 0 | 0 | 0 | 0 |
| K | 0.00 | 0.00 | 0.00 | 0.00 | 0.00 | 0 | 0 | 0 | 0 |
| Ba | 0.00 | 0.00 | 0.00 | 0.00 | 0.00 | 0 | 0 | 0 | 0 |
| Rb | 0.00 | 0.00 | 0.00 | 0.00 | 0.00 | 0 | 0 | 0 | 0 |
| F | 0.00 | 0.00 | 0.00 | 0.00 | 0.00 | 0 | 0 | 0 | 0 |
| Cl | 0.00 | 0.00 | 0.00 | 0.00 | 0.00 | 0 | 0 | 0 | 0 |
| Total | 1.66 | 1.66 | 1.66 | 1.63 | 1.72 | 1.633536648 | 1.659232047 | 1.705567292 | 1.674339692 |
| **Formula based on 36 O** | | | | | | | | | |
| Si | 5.36 | 5.17 | 5.17 | 5.48 | 5.24 | 5.475233056 | 5.336910308 | 5.12947795 | 5.574097738 |
| Ti | 0.00 | 0.00 | 0.00 | 0.00 | 0.00 | 0 | 0 | 0 | 0 |
| Al | 5.24 | 5.30 | 5.30 | 4.82 | 5.46 | 4.819463866 | 5.011463222 | 5.454136687 | 4.673706356 |
| Cr | 0.00 | 0.00 | 0.00 | 0.00 | 0.00 | 0 | 0 | 0 | 0 |
| Fe3+ | 0.00 | 0.00 | 0.00 | 0.00 | 0.00 | 0 | 0 | 0 | 0 |
| Fe2+ | 4.73 | 4.51 | 4.51 | 5.77 | 4.30 | 5.767750598 | 5.485906336 | 5.580605061 | 5.877717687 |
| Mn | 0.00 | 0.00 | 0.00 | 0.00 | 0.00 | 0 | 0 | 0 | 0 |
| Mg | 4.68 | 5.19 | 5.19 | 4.05 | 5.03 | 4.052587491 | 4.323078215 | 3.979234007 | 3.963527303 |
| Ni | 0.00 | 0.00 | 0.00 | 0.00 | 0.00 | 0 | 0 | 0 | 0 |
| Zn | 0.00 | 0.00 | 0.00 | 0.00 | 0.00 | 0 | 0 | 0 | 0 |
| Ca | 0.00 | 0.00 | 0.00 | 0.00 | 0.00 | 0 | 0 | 0 | 0 |
| Na | 0.00 | 0.00 | 0.00 | 0.00 | 0.00 | 0 | 0 | 0 | 0 |
| K | 0.00 | 0.00 | 0.00 | 0.00 | 0.00 | 0 | 0 | 0 | 0 |
| Ba | 0.00 | 0.00 | 0.00 | 0.00 | 0.00 | 0 | 0 | 0 | 0 |
| Rb | 0.00 | 0.00 | 0.00 | 0.00 | 0.00 | 0 | 0 | 0 | 0 |
| F | 0.00 | 0.00 | 0.00 | 0.00 | 0.00 | 0 | 0 | 0 | 0 |
| Cl | 0.00 | 0.00 | 0.00 | 0.00 | 0.00 | 0 | 0 | 0 | 0 |
| Total | 20.02 | 20.18 | 20.18 | 20.12 | 20.03 | 20.11503501 | 20.15735808 | 20.14345371 | 20.08904908 |
| Fe3+ | -0.02 | -0.18 | -0.18 | -0.12 | -0.03 | -0.115035011 | -0.157358081 | -0.143453706 | -0.089049084 |
| Fe3+ = 0 if Fe3+ < 0 | 0.00 | 0.00 | 0.00 | 0.00 | 0.00 | 0 | 0 | 0 | 0 |
| Fe2+ = total Fe2+ - Fe3+ | 4.75 | 4.69 | 4.69 | 5.88 | 4.33 | 5.882785609 | 5.643264417 | 5.724058767 | 5.966766771 |
| Fe3+ = total Fe2+ if Fe3+ > total Fe2+ | 0.00 | 0.00 | 0.00 | 0.00 | 0.00 | 0 | 0 | 0 | 0 |
| **Intermediate 36 O** | | | | | | | | | |
| Si | 10.72 | 10.34 | 10.34 | 10.95 | 10.47 | 10.95046611 | 10.67382062 | 10.2589559 | 11.14819548 |
| Ti | 0.00 | 0.00 | 0.00 | 0.00 | 0.00 | 0 | 0 | 0 | 0 |
| Al | 7.86 | 7.95 | 7.95 | 7.23 | 8.20 | 7.229195798 | 7.517194833 | 8.181205031 | 7.010559533 |
| Cr | 0.00 | 0.00 | 0.00 | 0.00 | 0.00 | 0 | 0 | 0 | 0 |
| Fe3+ | 0.00 | 0.00 | 0.00 | 0.00 | 0.00 | 0 | 0 | 0 | 0 |
| Fe2+ | 4.75 | 4.69 | 4.69 | 5.88 | 4.33 | 5.882785609 | 5.643264417 | 5.724058767 | 5.966766771 |
| Mn | 0.00 | 0.00 | 0.00 | 0.00 | 0.00 | 0 | 0 | 0 | 0 |
| Mg | 4.68 | 5.19 | 5.19 | 4.05 | 5.03 | 4.052587491 | 4.323078215 | 3.979234007 | 3.963527303 |

| | | | | | | | | | |
|---|---|---|---|---|---|---|---|---|---|
| Ni | 0.00 | 0.00 | 0.00 | 0.00 | 0.00 | 0 | 0 | 0 | 0 |
| Zn | 0.00 | 0.00 | 0.00 | 0.00 | 0.00 | 0 | 0 | 0 | 0 |
| Ca | 0.00 | 0.00 | 0.00 | 0.00 | 0.00 | 0 | 0 | 0 | 0 |
| Na | 0.00 | 0.00 | 0.00 | 0.00 | 0.00 | 0 | 0 | 0 | 0 |
| K | 0.00 | 0.00 | 0.00 | 0.00 | 0.00 | 0 | 0 | 0 | 0 |
| Ba | 0.00 | 0.00 | 0.00 | 0.00 | 0.00 | 0 | 0 | 0 | 0 |
| Rb | 0.00 | 0.00 | 0.00 | 0.00 | 0.00 | 0 | 0 | 0 | 0 |
| F | 0.00 | 0.00 | 0.00 | 0.00 | 0.00 | 0 | 0 | 0 | 0 |
| Cl | 0.00 | 0.00 | 0.00 | 0.00 | 0.00 | 0 | 0 | 0 | 0 |
| Total | 28.02 | 28.18 | 28.18 | 28.12 | 28.03 | 28.11503501 | 28.15735808 | 28.14345371 | 28.08904908 |
| | | | | | | | | | |
| **Formula based on 36 oxygens inc. Fe2/Fe3** | | | | | | | | | |
| Si | 5.36 | 5.14 | 5.14 | 5.45 | 5.23 | 5.452830683 | 5.307084855 | 5.103331813 | 5.556426499 |
| Ti | 0.00 | 0.00 | 0.00 | 0.00 | 0.00 | 0 | 0 | 0 | 0 |
| Al | 5.24 | 5.27 | 5.27 | 4.80 | 5.46 | 4.799744627 | 4.983456538 | 5.426335689 | 4.658889575 |
| Cr | 0.00 | 0.00 | 0.00 | 0.00 | 0.00 | 0 | 0 | 0 | 0 |
| Fe3+ | 0.00 | 0.00 | 0.00 | 0.00 | 0.00 | 0 | 0 | 0 | 0 |
| Fe2+ | 4.75 | 4.66 | 4.66 | 5.86 | 4.33 | 5.858715701 | 5.611726897 | 5.694881912 | 5.947850677 |
| Mn | 0.00 | 0.00 | 0.00 | 0.00 | 0.00 | 0 | 0 | 0 | 0 |
| Mg | 4.68 | 5.16 | 5.16 | 4.04 | 5.02 | 4.036005992 | 4.298918587 | 3.958950929 | 3.950961962 |
| Ni | 0.00 | 0.00 | 0.00 | 0.00 | 0.00 | 0 | 0 | 0 | 0 |
| Zn | 0.00 | 0.00 | 0.00 | 0.00 | 0.00 | 0 | 0 | 0 | 0 |
| Ca | 0.00 | 0.00 | 0.00 | 0.00 | 0.00 | 0 | 0 | 0 | 0 |
| Na | 0.00 | 0.00 | 0.00 | 0.00 | 0.00 | 0 | 0 | 0 | 0 |
| K | 0.00 | 0.00 | 0.00 | 0.00 | 0.00 | 0 | 0 | 0 | 0 |
| Ba | 0.00 | 0.00 | 0.00 | 0.00 | 0.00 | 0 | 0 | 0 | 0 |
| Rb | 0.00 | 0.00 | 0.00 | 0.00 | 0.00 | 0 | 0 | 0 | 0 |
| F | 0.00 | 0.00 | 0.00 | 0.00 | 0.00 | 0 | 0 | 0 | 0 |
| Cl | 0.00 | 0.00 | 0.00 | 0.00 | 0.00 | 0 | 0 | 0 | 0 |
| OH* | 16.00 | 16.00 | 16.00 | 16.00 | 16.00 | 16 | 16 | 16 | 16 |
| Total | 36.02 | 36.23 | 36.23 | 36.15 | 36.04 | 36.147297 | 36.20118688 | 36.18350034 | 36.11412871 |
| | | | | | | | | | |
| FeO calc | 28.17 | 26.67 | 26.67 | 33.65 | 26.51 | 33.65435989 | 32.44506714 | 33.95025067 | 35.19813787 |
| Fe2O3 calc | 0.00 | 0.00 | 0.00 | 0.00 | 0.00 | 0 | 0 | 0 | 0 |
| | | | | | | | | | |
| **Temperatures** | **363.37** | **398.88** | **398.88** | **348.15** | **383.96** | **348.15** | **371.61** | **404.41** | **331.47** |

# Appendix B: LA-ICP-MS analysis of sulfides

20ALS3S1

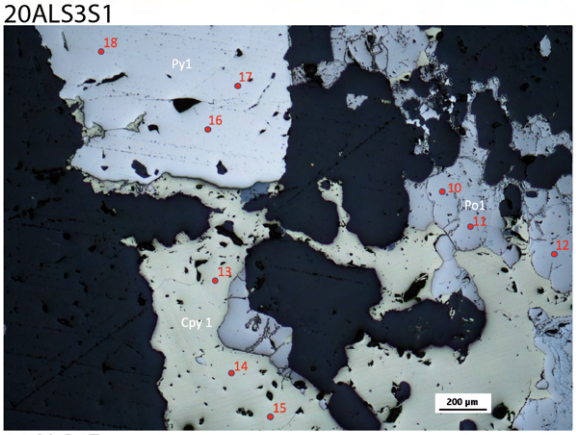


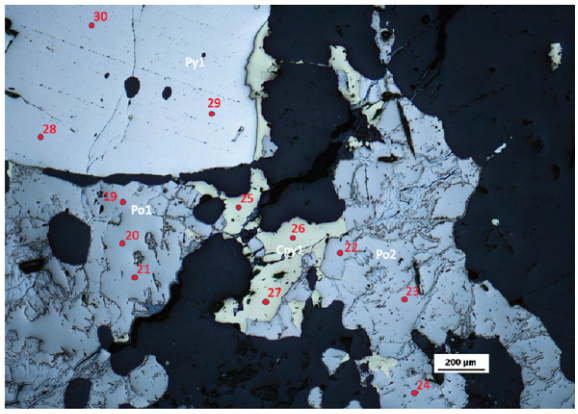


20ALS4F

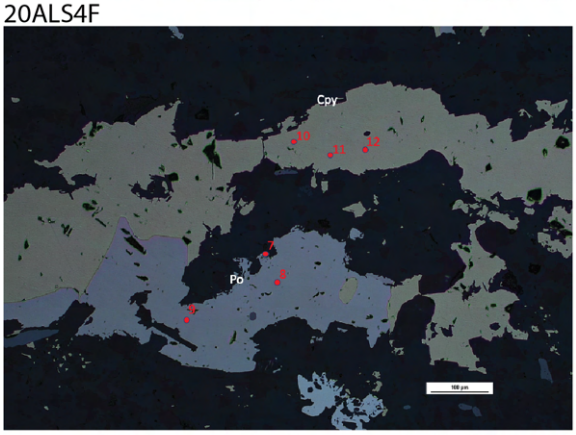


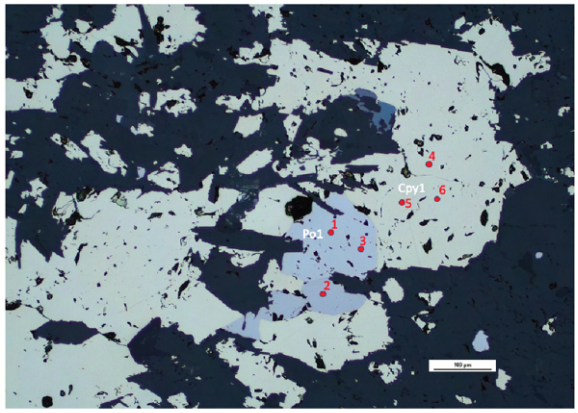


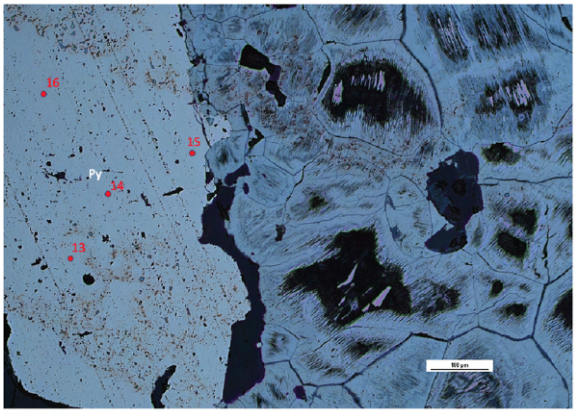


19LIT2

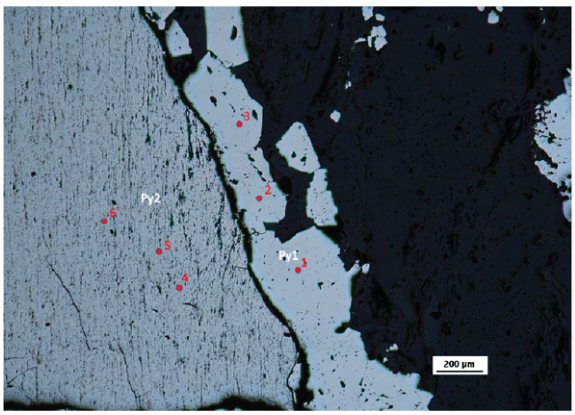


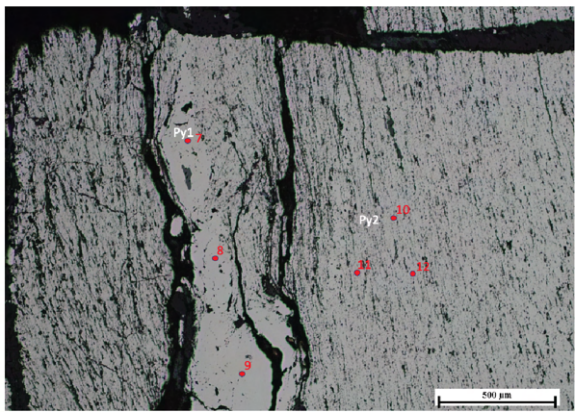


Figure B1: Location of analyzed spots from LA-ICP-MS of sulfide minerals. The number marked can be correlated to the numbers in the spreadsheet below.

Table 1B: Trace element compositions of sulfide minerals analyzed by LA-ICP-MS. All concentrations are given in ppm.

| Sample | 20ALS4F | 20ALS4F | 20ALS4F | 20ALS4F | 20ALS4F | 20ALS4F | 20ALS4F | 20ALS4F | 20ALS4F | 20ALS4F | 20ALS4F | 20ALS4F | 20ALS4F | 20ALS4F | 20ALS4F | 20ALS4F |
|---|---|---|---|---|---|---|---|---|---|---|---|---|---|---|---|---|
| mineral | Po-1 | Po-2 | Po-3 | Cpy-4 | Cpy-5 | Cpy-6 | Po-7 | Po-8 | Po-9 | CPY-10 | CPY-11 | CPY-12 | Py-13 | Py-14 | Py-15 | Py-16 |
| **Si** | 121.61 | 350.75 | 463.99 | 174.18 | 166.42 | 177.21 | 110.82 | 76.7 | 265.6 | 265.3 | 202.6 | 174.97 | 1320.7 | 378.86 | 740.43 | 135.65 |
| **S** | 425296.1 | 422776.9 | 417102.9 | 412433.7 | 373918 | 375727.9 | 468274.6 | 442520.1 | 458539.5 | 422621.9 | 423473.6 | 429318.1 | 598685.8 | 627569.4 | 546416.2 | 560037.6 |
| **Ti** | 3.69 | 3.17 | 3.82 | 3.59 | 2.4 | 3.42 | 3.63 | 4.6 | 3.99 | 2.4 | 3.25 | 3.86 | 4.92 | 6.31 | 5.19 | 5.55 |
| **V** | 0.0173 | 0.114 | n.d.71 | n.d.76 | 0.0119 | n.d.58 | n.d.76 | 0.0485 | n.d.74 | 0.0662 | n.d.74 | 0.0115 | 0.027 | 0.0407 | 0.0048 | n.d.30 |
| **Cr** | <0.195 | 2.43 | 1.58 | 1.52 | 2.44 | 1.51 | 0.64 | <0.225 | 3.28 | 2.23 | 1.49 | 2.51 | <0.10 | <0.11 | <0.10 | <0.09 |
| **Mn** | 0.88 | 2.17 | 2.64 | 0.76 | 0.656 | 0.65 | 0.8 | 0.85 | 0.79 | 0.187 | 0.52 | 0.361 | 0.522 | 0.586 | 0.47 | 0.428 |
| **Fe** | 623403.4 | 623403.3 | 623403.3 | 306260.5 | 306260.5 | 306260.5 | 623403.4 | 623403.4 | 623403.3 | 306260.5 | 306260.5 | 306260.5 | 460012.6 | 460012.7 | 460012.7 | 460012.6 |
| **Co** | 2097.25 | 2276.11 | 2032.58 | 7.2 | 6.97 | 7.18 | 1662.66 | 1484.45 | 1617.11 | 6.95 | 11.66 | 6.65 | 464.26 | 330.71 | 188.01 | 17.15 |
| **Ni** | 669.64 | 674.51 | 680.85 | 16.56 | 17.29 | 17.65 | 648.78 | 620.39 | 657.11 | 17.95 | 19.62 | 19.36 | 4.42 | 2.81 | 1.43 | 1.63 |
| **Cu** | 0.113 | 1.671 | 0.132 | 322072.5 | 8.11 | 305306.1 | <0.115 | <0.094 | <0.102 | 321485.4 | 335244.6 | 312942.5 | 3.77 | 49.51 | 1.515 | 0.357 |
| **Zn** | <0.17 | 0.93 | 1.78 | 674.34 | 439.64 | 512.15 | <0.229 | <0.25 | 0.81 | 539.14 | 575.54 | 538.85 | <0.092 | 56.13 | 0.66 | <0.10 |
| **Ga** | n.d.41 | 0.011 | n.d.40 | n.d.45 | 0.0038 | n.d.36 | n.d.53 | 0.0228 | n.d.56 | 0.0231 | 0.0505 | n.d.49 | 0.008 | 0.00303 | 0.0051 | n.d.189 |
| **Ge** | 1.16 | 0.154 | <0.110 | <0.13 | 0.71 | <0.096 | 0.29 | <0.143 | 1.31 | 0.352 | 1.59 | 0.94 | 0.84 | 0.51 | 0.71 | 0.81 |
| **As** | 2.63 | 3.15 | 3.53 | 1.66 | 2.57 | 2.23 | 2.02 | 2.41 | 3.58 | 2.73 | 1.7 | 1.78 | 51.42 | 151.43 | 239.18 | 1.66 |
| **Se** | 349.18 | 335.35 | 331.61 | 425.09 | 352.49 | 367.45 | 389.42 | 370.53 | 367.53 | 398.63 | 408.71 | 433.69 | 617.47 | 723.19 | 544.39 | 264.71 |
| **Nb** | n.d.194 | 0.0089 | 0.0138 | 0.0183 | n.d. | n.d.19 | n.d.33 | n.d.37 | 0.0109 | n.d.23 | 0.015 | 0.0178 | 0.012 | 0.0045 | n.d.16 | 0.0066 |
| **Mo** | 2.19 | 1.679 | 1.636 | 0.508 | 0.687 | 0.74 | 1.91 | 1.89 | 1.97 | 0.643 | 0.78 | 0.692 | 1.293 | 2.2 | 1.473 | 1.73 |
| **Ru** | 0.875 | 0.721 | 0.699 | 0.559 | 0.468 | 0.615 | 0.334 | 0.374 | 0.475 | 0.837 | 0.649 | 0.624 | 0.0446 | 0.1178 | 0.0861 | n.d. |
| **Rh** | n.d. | n.d. | n.d.23 | 29.42 | 28.39 | 27.91 | 0.0079 | 0.0096 | n.d.26 | 29.28 | 29.11 | 28.66 | n.d.083 | 0.0127 | 0.00217 | n.d.071 |
| **Ag** | 0.584 | 0.73 | 0.378 | 15.8 | 14.25 | 14.37 | 0.154 | 0.823 | 0.577 | 12.47 | 12.82 | 12.05 | 0.0436 | 0.509 | 0.0436 | 0.00223 |
| **Pd** | n.d.7 | 0.02 | 0.0125 | 0.229 | 0.171 | 0.17 | n.d.8 | n.d.70 | n.d.55 | 0.37 | 0.29 | 0.173 | 0.0164 | 0.045 | n.d.31 | n.d.4 |
| **Cd** | 0.082 | 0.101 | 0.073 | 8.57 | 5.26 | 6.03 | <0.025 | <0.020 | <0.022 | 7.22 | 7.54 | 7.25 | n.d.65 | 0.53 | n.d.8 | n.d.56 |
| **In** | 0.00629 | n.d. | n.d.098 | 3.2 | 3.01 | 3.03 | 0.00487 | n.d.16 | 0.00255 | 3.76 | 3.87 | 3.89 | 0.00065 | 0.0246 | n.d.048 | n.d. |
| **Sn** | <0.029 | <0.031 | <0.031 | 0.276 | <0.0258 | 0.178 | 0.112 | <0.035 | <0.039 | 0.252 | 0.426 | 0.51 | <0.017 | <0.016 | 0.049 | <0.0134 |
| **Sb** | 0.133 | 2.63 | 0.34 | 0.28 | 0.275 | 0.312 | 0.0126 | 0.78 | 0.349 | 0.45 | 0.51 | 0.5 | 2.22 | 1.7 | 1.02 | 0.073 |
| **Te** | 0.964 | 1.519 | 0.73 | 13.36 | 10.74 | 13.7 | 1.217 | 1.63 | 1.156 | 19.83 | 18.56 | 18.8 | 17.12 | 36.38 | 25.59 | 1.199 |
| **Ba** | n.d.29 | n.d.69 | 0.04 | n.d.82 | 0.009 | 0.008 | n.d.91 | 0.304 | n.d.98 | n.d.73 | n.d.95 | 0.015 | 0.0498 | 0.0045 | 0.0109 | n.d.30 |
| **W** | n.d. | n.d. | n.d. | n.d. | n.d. | n.d. | n.d. | n.d. | n.d. | n.d. | n.d. | n.d. | n.d. | n.d. | n.d. | n.d. |
| **Re** | n.d. | n.d. | n.d. | n.d. | n.d. | n.d. | n.d. | n.d. | n.d. | n.d. | n.d. | n.d. | 0.0174 | 0.0158 | 0.00696 | 0.118 |
| **Os** | n.d. | n.d. | n.d. | n.d. | n.d. | n.d. | n.d. | n.d. | n.d. | n.d. | n.d. | n.d. | n.d. | n.d. | n.d. | n.d. |
| **Ir** | n.d. | n.d. | n.d. | n.d. | n.d. | n.d. | n.d. | n.d. | n.d. | n.d. | n.d. | n.d. | n.d. | n.d. | n.d. | n.d. |
| **Pt** | n.d. | n.d. | n.d. | n.d. | n.d. | n.d. | n.d. | n.d. | n.d. | n.d. | n.d. | n.d. | n.d. | n.d. | n.d. | n.d. |
| **Au** | n.d. | n.d. | n.d. | n.d. | n.d. | n.d. | n.d. | n.d. | n.d. | n.d. | 0.0038 | n.d. | n.d. | 0.006 | 0.0037 | n.d. |
| **Hg** | 0.32 | 0.21 | 0.41 | 1.25 | 0.64 | 1.36 | 0.45 | 0.26 | 0.65 | 1.06 | 1.01 | 1.19 | 0.29 | 0.73 | 0.25 | <0.03 |
| **Tl** | 0.0092 | 0.0122 | n.d. | n.d.104 | 0.0046 | 0.0044 | n.d.18 | n.d.112 | n.d.18 | n.d. | 0.00312 | 0.00506 | n.d. | n.d.076 | n.d.12 | 0.00197 |
| **Pb** | 1.236 | 2.07 | 0.268 | 1.137 | 0.752 | 0.56 | 0.1333 | 0.981 | 0.404 | 0.948 | 1.327 | 0.769 | 1.68 | 1.234 | 0.658 | 0.1176 |
| **Bi** | 0.149 | 0.26 | 0.046 | 0.41 | 0.2 | 0.26 | 0.031 | 0.3 | 0.125 | 0.68 | 1.34 | 2.72 | 1.44 | 0.67 | 0.42 | 0.05 |

Table B1: Continued

| Sample | 20ALS3S1 | 20ALS31 | 20ALS3S1 | 20ALS3S1 | 20ALS3S1 | 20ALS3S1 | 20ALS31 | 20ALS3S1 | 20ALS3S1 | 20ALS3S1 | 20ALS3S1 | 20ALS3S1 | 20ALS3S1 | 20ALS3S1 | 20ALS3S1 | 20ALS3S1 |
|---|---|---|---|---|---|---|---|---|---|---|---|---|---|---|---|---|
| mineral | Po-10 | Po-11 | Po-12 | Cpy-13 | Cpy-14 | Cpy-15 | Po-16 | Po-17 | Po-18 | Po-19 | Po-20 | Po-21 | Po-22 | Po-23 | Po-24 | Cpy-25 |
| **Si** | 140 | 301.11 | 218.38 | 1265.23 | 158.75 | 198.52 | <6.57 | 54.69 | 64.16 | 209.1 | 165.45 | 176.96 | 178.73 | 126.15 | 238.94 | 245.96 |
| **S** | 398144.1 | 407352.9 | 416228.1 | 407357 | 383288.4 | 381876.9 | 786357.9 | 819631.6 | 874962.7 | 432864.4 | 410557 | 412966.9 | 417884.5 | 452905.4 | 445246.9 | 410396.4 |
| **Ti** | 4.47 | 2.92 | 5.22 | 36.37 | 3.15 | 3.47 | 6.71 | 9.38 | 8.43 | 2.92 | 2.08 | 2.06 | 3.05 | 4.11 | 3.36 | 4.19 |
| **V** | 0.0462 | n.d.77 | n.d.64 | 2.85 | n.d.63 | 0.0358 | 0.0283 | 0.158 | 0.0133 | n.d.94 | 0.0412 | 0.0327 | n.d.49 | <0.0104 | 0.029 | 0.0369 |
| **Cr** | 2.34 | 1.97 | 2.49 | 18.36 | 1.09 | 1.64 | <0.13 | <0.14 | <0.12 | 0.6 | 2.66 | 1.95 | 4.56 | 2.46 | 0.89 | 2.07 |
| **Mn** | 0.99 | 1.1 | 0.85 | 9.71 | 0.71 | 0.58 | 0.65 | 0.95 | 0.68 | 0.65 | 1.26 | 0.88 | 0.81 | 0.59 | 0.91 | 0.1 |
| **Fe** | 623403.4 | 623403.4 | 623403.4 | 306260.5 | 306260.5 | 306260.5 | 623403.3 | 623403.4 | 623403.4 | 623403.4 | 623403.4 | 623403.4 | 623403.4 | 623403.4 | 623403.4 | 306260.5 |
| **Co** | 8.45 | 10.15 | 10.37 | 0.13 | 0.0656 | 0.0503 | 3616.34 | 3765.96 | 4650.96 | 9.98 | 9.46 | 10.19 | 10.14 | 10.42 | 9.83 | 0.0507 |
| **Ni** | 376.4 | 431.49 | 308.5 | 16.07 | 16.53 | 12.17 | 0.87 | 4.64 | 5.64 | 405.21 | 537.51 | 266.44 | 361.24 | 441.11 | 402.16 | 14.17 |
| **Cu** | 0.487 | 0.322 | <0.087 | 315585.4 | 319104.1 | 325434.6 | 0.477 | 1.223 | 0.255 | 1.092 | 0.425 | 0.204 | 0.548 | 0.464 | 0.516 | 330386.1 |
| **Zn** | <0.20 | 1.59 | <0.21 | 1062.2 | 634.99 | 551.32 | <0.15 | <0.16 | 1.15 | <0.241 | 0.43 | 0.49 | 1.16 | <0.31 | <0.252 | 520.62 |
| **Ga** | 0.0194 | 0.0124 | 0.0483 | 0.208 | 0.065 | 0.059 | n.d.32 | 0.0326 | n.d.29 | n.d.64 | 0.0157 | 0.0279 | n.d.46 | n.d.70 | 0.0237 | 0.157 |
| **Ge** | 0.158 | 1.23 | 1 | 0.91 | 0.89 | <0.134 | 0.84 | 1.02 | 0.61 | 0.66 | 1.86 | 0.92 | 1.22 | 0.75 | 1.24 | 0.89 |
| **As** | 1.97 | 2.91 | 2.6 | 1.31 | 2.29 | 1.93 | 7.07 | 0.66 | 1.05 | 2.79 | 2.72 | 2.94 | 1.87 | 2.54 | 2.77 | 2.1 |
| **Se** | 255.79 | 243.67 | 261.34 | 278.47 | 255.81 | 264.56 | 128.44 | 138.48 | 169.81 | 287.39 | 260.94 | 246.45 | 243.42 | 244.58 | 247.57 | 280.24 |
| **Nb** | n.d.33 | 0.0041 | n.d.4 | n.d.166 | 0.0104 | n.d.154 | 0.0076 | 0.0107 | 0.0135 | n.d.26 | n.d. | n.d.170 | 0.0105 | n.d.34 | 0.015 | 0.0054 |
| **Mo** | 1.23 | 2.12 | 1.92 | 0.495 | 0.681 | 0.834 | 1.512 | 1.81 | 2.14 | 1.93 | 1.47 | 1.57 | 1.68 | 1.77 | 1.54 | 0.718 |
| **Ru** | 0.0236 | <0.0102 | <0.0203 | 0.792 | 0.705 | 0.468 | 1.3 | 1.4 | 1.78 | <0.0133 | 0.0623 | <0.0108 | <0.0102 | <0.0107 | 0.0804 | 0.818 |
| **Rh** | 0.0147 | 0.011 | 0.00291 | 27.47 | 27.25 | 27.94 | n.d.110 | n.d.149 | n.d.15 | 0.0206 | n.d.29 | 0.0308 | n.d. | n.d.36 | n.d.38 | 27.14 |
| **Ag** | 0.0775 | 0.0251 | 2.09 | 22.34 | 19.94 | 31 | 0.0111 | 0.0187 | n.d.39 | 0.675 | 0.033 | 0.455 | 1.43 | 0.425 | 0.893 | 21.02 |
| **Pd** | 0.067 | 0.033 | <0.0110 | 0.46 | 0.42 | 0.202 | n.d.8 | n.d.6 | n.d.45 | <0.0123 | <0.011 | <0.014 | 0.045 | 0.081 | <0.015 | 0.191 |
| **Cd** | <0.018 | 0.042 | <0.025 | 15.93 | 11.3 | 11.67 | 0.034 | 0.053 | 0.089 | <0.023 | <0.0139 | <0.0129 | <0.015 | 0.075 | 0.025 | 8.93 |
| **In** | 0.00722 | 0.0156 | 0.00226 | 20.08 | 18.69 | 18.75 | 0.0099 | n.d.050 | n.d. | n.d.18 | 0.00163 | 0.0021 | n.d. | n.d.23 | 0.00239 | 23.2 |
| **Sn** | 0.292 | 0.078 | <0.037 | 2.35 | 1.96 | 2.04 | <0.0185 | 0.113 | 0.102 | <0.042 | 0.252 | 0.126 | 0.132 | 0.16 | 0.039 | 2.26 |
| **Sb** | n.d. | n.d. | n.d.39 | 0.318 | 0.41 | 0.38 | n.d. | n.d.25 | n.d. | 0.042 | n.d. | n.d. | n.d. | n.d. | 0.0088 | 0.31 |
| **Te** | 0.917 | 1.055 | 1.84 | 13.75 | 19.21 | 15.24 | <0.0205 | 0.51 | <0.020 | 1.82 | 1.73 | 1.039 | 0.938 | 1.42 | 0.944 | 12.81 |
| **Ba** | n.d.86 | n.d.59 | n.d.96 | 0.528 | 0.0213 | 0.0367 | n.d.65 | 0.0457 | 0.0048 | <0.0108 | <0.0120 | n.d.82 | n.d.41 | <0.0137 | n.d.96 | 0.0193 |
| **W** | n.d. | n.d. | n.d. | n.d. | n.d. | n.d. | n.d. | n.d. | n.d. | n.d. | n.d. | n.d. | n.d. | n.d. | n.d. | n.d. |
| **Re** | n.d. | n.d. | n.d. | n.d. | n.d. | n.d. | n.d. | n.d. | n.d. | n.d. | n.d. | n.d. | n.d. | n.d. | n.d. | n.d. |
| **Os** | n.d. | n.d. | n.d. | n.d. | n.d. | n.d. | n.d. | n.d. | n.d. | n.d. | n.d. | n.d. | n.d. | n.d. | n.d. | n.d. |
| **Ir** | n.d. | n.d. | n.d. | n.d. | n.d. | n.d. | n.d. | n.d. | n.d. | n.d. | n.d. | n.d. | n.d. | n.d. | n.d. | n.d. |
| **Pt** | n.d. | n.d. | n.d. | n.d. | n.d. | n.d. | n.d. | n.d. | n.d. | n.d. | n.d. | n.d. | n.d. | n.d. | n.d. | n.d. |
| **Au** | n.d. | 0.0036 | n.d. | n.d. | n.d. | n.d. | n.d. | n.d. | n.d. | n.d. | n.d. | n.d. | n.d. | n.d. | n.d. | n.d. |
| **Hg** | 0.75 | 0.67 | 1.31 | 1 | 0.9 | 0.23 | <0.05 | 0.2 | 0.27 | 0.81 | 0.48 | 0.46 | 1.29 | 0.81 | 1.48 | 0.53 |
| **Tl** | 0.00354 | 0.00286 | n.d. | 0.0118 | n.d.15 | 0.0071 | n.d. | n.d. | 0.0053 | 0.00374 | 0.00307 | n.d.15 | 0.0382 | n.d. | 0.00346 | 0.00371 |
| **Pb** | 0.00706 | n.d.186 | 4.47 | 1.53 | 0.742 | 1.9 | n.d. | 0.00996 | n.d. | 1.135 | 0.0145 | 0.257 | 6.64 | 0.317 | 0.458 | 1.118 |
| **Bi** | n.d.18 | 0.026 | 0.55 | 0.3 | 0.21 | 0.29 | n.d. | 0.56 | n.d. | 0.53 | 0.0045 | 0.17 | 0.39 | 0.21 | 0.15 | 0.23 |
| **U** | n.d. | n.d. | n.d. | 0.00231 | n.d. | n.d. | n.d. | n.d. | n.d. | n.d. | n.d. | n.d. | n.d. | n.d. | n.d. | n.d. |

Table B1: Continued

| Sample mineral | 20ALS3S1 Cpy-26 | 20ALS3S1 Cpy-27 | 20ALS3S1 Py-28 | 20ALS3S1 Py-29 | 20ALS3S1 Py-30 | 20ALS3S1 Cpy-26 | 19LITE3 Py-1 | 19LITE3 Py-2 | 19LITE3 Py-3 | 19LITE3 Py-4 | 19LITE3 Py-5 | 19LITE3 Py-6 | 19LITE3 Py-7 | 19LITE3 Py-8 | 19LITE3 Py-9 | 19LITE3 Py-10 | 19LITE3 Py-11 | 19LITE3 Py-12 | 19LITE3 Po-13 |
|---|---|---|---|---|---|---|---|---|---|---|---|---|---|---|---|---|---|---|---|
| **Si** | 153.49 | 190.29 | 16.25 | 5.56 | 5765.23 | 153.49 | 15026.52 | 7492.65 | 578.62 | 459.76 | 1517.16 | 2256.15 | 2403.65 | 1737.61 | 310.9 | 33470.54 | 8124.38 | 34765.29 | 7433.76 |
| **S** | 393338.3 | 418722 | 655912.9 | 608410.5 | 568995.7 | 393338.3 | 564287.6 | 563554.3 | 530704.1 | 602686.8 | 537316.1 | 546070.4 | 555489.4 | 610324.5 | 607652.6 | 542973.4 | 460553.8 | 530127.7 | 546498.8 |
| **Ti** | 3.19 | 5.01 | 5.97 | 5.62 | 5.56 | 3.19 | 66.82 | 14.72 | 6.78 | 7.9 | 10.68 | 78.33 | 29.93 | 13.67 | 7.15 | 77.94 | 11.18 | 135.76 | 14.16 |
| **V** | 0.0311 | n.d.80 | n.d.36 | 0.0157 | 0.0394 | 0.0311 | 9.19 | 52.33 | 1.63 | 1.34 | 11.85 | 13.15 | 8.03 | 6.94 | 1.25 | 43.43 | 1.52 | 65.6 | 5.93 |
| **Cr** | 0.71 | 2.28 | <0.11 | <0.108 | <0.11 | 0.71 | 1.11 | 33.38 | 0.39 | <0.097 | 8.63 | 3.91 | 2.01 | 2.55 | <0.10 | 4.96 | 0.59 | 12.23 | 4.14 |
| **Mn** | 0.68 | 1.08 | 0.435 | 0.57 | 0.62 | 0.68 | 13.41 | 82.09 | 14.56 | 16.87 | 29.83 | 26.78 | 6.82 | 14.99 | 27.82 | 21.5 | 4.75 | 208.59 | 1246.73 |
| **Fe** | 306260.5 | 306260.6 | 460012.7 | 460012.7 | 460012.7 | 306260.5 | 460012.7 | 460012.7 | 460012.7 | 460012.7 | 460012.7 | 460012.7 | 460012.7 | 460012.7 | 460012.7 | 460012.7 | 460012.7 | 460012.7 | 623403.4 |
| **Co** | 0.0985 | 0.103 | 4866.86 | 123.61 | 3302.34 | 0.0985 | 8.21 | 6.12 | 8.69 | 1.85 | 1.13 | 2.16 | 3.23 | 2.5 | 2.08 | 9.13 | 7.04 | 7.35 | 0.165 |
| **Ni** | 14.78 | 13.07 | 4.91 | 20.47 | 2.41 | 14.78 | 23.36 | 8.95 | 21.37 | 13.88 | 7.41 | 13.34 | 21.04 | 16.94 | 10.07 | 88.87 | 64.95 | 85.8 | 126 |
| **Cu** | 311331.4 | 328668 | 0.446 | 0.324 | 0.625 | 311331.4 | 6 | 2.05 | 1.47 | 3.34 | 1.29 | 1.88 | 4.7 | 10.79 | 1.38 | 18.12 | 8.09 | 19.97 | 8003.59 |
| **Zn** | 649.03 | 503.12 | 0.62 | <0.10 | <0.10 | 649.03 | 29.39 | 8.58 | 0.31 | 15.43 | 2.12 | 3.87 | 13.38 | 11.2 | 1.09 | 46.57 | 36.6 | 27360.35 | 247414.1 |
| **Ga** | 0.151 | 0.17 | n.d.26 | n.d.28 | 0.0074 | 0.151 | 0.285 | 0.93 | 0.0086 | 0.0199 | 0.174 | 0.176 | 0.175 | 0.153 | 0.0123 | 0.8 | 0.0233 | 1.38 | 0.075 |
| **Ge** | <0.17 | 0.23 | 1.25 | 1.11 | 0.86 | <0.17 | 1.43 | 1.38 | 1.62 | 1.74 | 0.91 | 1.06 | 1.11 | 1.57 | 1.15 | 1.12 | 0.84 | 1.27 | <0.25 |
| **As** | 2.19 | 2.95 | 257.17 | 104.22 | 0.6 | 2.19 | 718.63 | 626.72 | 558.28 | 643.88 | 423.21 | 739.96 | 902.36 | 919.01 | 553.04 | 1104.23 | 938.06 | 992.43 | 37.33 |
| **Se** | 259.54 | 267.21 | 156.21 | 159.12 | 79.76 | 259.54 | <0.59 | 5.04 | 4.99 | 3.53 | 6.22 | 6.28 | 7.89 | 1.96 | 6.25 | <0.68 | 5.06 | 2.36 | 35.01 |
| **Nb** | 0.0043 | n.d.40 | 0.0055 | 0.0037 | n.d.12 | 0.0043 | 0.096 | 0.0025 | n.d.12 | n.d. | n.d.146 | 0.0113 | 0.0041 | n.d.11 | n.d.18 | 0.0123 | 0.027 | 0.035 | n.d.25 |
| **Mo** | 0.627 | 0.857 | 1.52 | 1.363 | 1.44 | 0.627 | 17.55 | 1.3 | 13.4 | 2.19 | 2.66 | 1.63 | 5.97 | 6.74 | 2.38 | 30.56 | 5.83 | 23.29 | 5.57 |
| **Ru** | 0.616 | 0.88 | 2.08 | 0.0417 | 1.31 | 0.616 | <0.0107 | 0.012 | 0.0574 | n.d.76 | 0.0299 | 0.0121 | n.d. | 0.0363 | 0.0271 | 0.0441 | <0.0106 | <0.015 | 0.0165 |
| **Rh** | 27.07 | 26.76 | 0.00288 | 0.00235 | 0.0089 | 27.07 | n.d.16 | 0.0046 | n.d.15 | 0.0151 | 0.0029 | 0.0148 | 0.0095 | n.d.17 | n.d.17 | n.d.23 | 0.00161 | n.d.25 | 0.56 |
| **Ag** | 21.22 | 19.35 | 0.0242 | n.d.31 | n.d.49 | 21.22 | 0.553 | 0.26 | 0.0803 | 0.802 | 0.0898 | 0.638 | 0.98 | 0.629 | 0.164 | 1.29 | 0.622 | 2.41 | 6.7 |
| **Pd** | 0.26 | 0.3 | n.d.62 | n.d.59 | 0.101 | 0.26 | 0.0176 | 0.065 | n.d.8 | 0.025 | 0.025 | n.d.48 | n.d.6 | n.d.66 | 0.0072 | 0.029 | 0.094 | 7.53 | 60.97 |
| **Cd** | 9.93 | 10.38 | 0.0135 | <0.014 | <0.011 | 9.93 | 0.043 | 0.08 | <0.011 | 0.16 | <0.014 | <0.011 | 0.096 | 0.15 | 0.23 | 0.57 | 0.34 | 164.84 | 1376.66 |
| **In** | 23.22 | 22.98 | n.d.068 | n.d. | 0.00369 | 23.22 | n.d.14 | n.d.12 | 0.00198 | n.d.063 | n.d.091 | 0.0106 | 0.00448 | 0.0141 | n.d.15 | 0.0304 | 0.00397 | 1.29 | 13.34 |
| **Sn** | 2.64 | 2.33 | 0.041 | 0.145 | 0.04 | 2.64 | 0.083 | <0.016 | <0.013 | <0.016 | 0.077 | 0.065 | <0.012 | 0.083 | 0.057 | 0.182 | 0.04 | 0.13 | 0.34 |
| **Sb** | 0.34 | 0.51 | n.d.20 | 0.0049 | 0.088 | 0.34 | 9.73 | 0.69 | 1.61 | 5.06 | 0.93 | 3.54 | 7.52 | 3.38 | 1.58 | 18.67 | 12.16 | 15.84 | 10.51 |
| **Te** | 15.26 | 18.92 | <0.0158 | 0.175 | 1.8 | 15.26 | 0.202 | 0.116 | <0.0145 | 0.11 | 0.0931 | 0.0567 | 0.098 | 0.0258 | 0.175 | 0.262 | 0.156 | 0.191 | <0.032 |
| **Ba** | <0.0121 | <0.0128 | n.d.62 | n.d.51 | 0.0187 | <0.0121 | 5.22 | 0.45 | 0.218 | 0.104 | 0.243 | 2.1 | 3.21 | 1.17 | 0.0578 | 15.83 | 0.32 | 25.35 | 0.72 |
| **W** | n.d. | n.d. | n.d. | n.d. | n.d. | n.d. | n.d. | n.d. | 0.0061 | n.d. | n.d. | n.d. | n.d. | n.d. | n.d. | 0.0126 | n.d. | 0.0124 | n.d. |
| **Re** | n.d. | n.d. | n.d. | n.d. | n.d. | n.d. | n.d. | n.d. | n.d. | n.d. | n.d. | n.d. | n.d. | n.d. | n.d.079 | n.d. | n.d. | n.d. | n.d. |
| **Os** | n.d. | n.d. | n.d. | n.d. | n.d. | n.d. | n.d. | n.d. | n.d. | n.d. | n.d. | n.d. | n.d. | n.d. | n.d. | n.d. | n.d. | n.d. | n.d. |
| **Ir** | n.d. | n.d. | n.d. | n.d. | n.d. | n.d. | n.d. | n.d. | n.d. | n.d. | n.d. | n.d. | n.d. | n.d. | n.d. | n.d. | n.d. | n.d. | n.d. |
| **Pt** | n.d. | n.d. | n.d. | n.d. | n.d. | n.d. | n.d. | n.d. | n.d. | n.d. | n.d. | n.d. | n.d. | n.d. | n.d. | n.d. | n.d. | n.d. | n.d. |
| **Au** | n.d. | n.d. | n.d. | n.d. | n.d. | n.d. | n.d. | 0.0043 | 0.00179 | 0.057 | n.d. | n.d. | 0.049 | 0.038 | 0.0115 | 0.022 | 0.038 | 0.0127 | 0.041 |
| **Hg** | 1.62 | 0.66 | 0.074 | 0.53 | 0.08 | 1.62 | 0.51 | 0.88 | 0.29 | 0.32 | 0.42 | 0.22 | 0.61 | 0.3 | <0.04 | 0.55 | 0.42 | 5.35 | 37.01 |
| **Tl** | n.d.143 | n.d. | 0.00284 | n.d. | n.d.060 | n.d.143 | 0.87 | 0.343 | 0.121 | 0.126 | 0.101 | 0.97 | 0.291 | 0.56 | 0.113 | 0.94 | 0.46 | 1.2 | 1.63 |
| **Pb** | 1.043 | 0.428 | n.d. | n.d. | 0.0763 | 1.043 | 29.34 | 5.73 | 4.83 | 18.53 | 3.53 | 12.44 | 23.07 | 18.11 | 4.76 | 64.28 | 37.74 | 60.61 | 50.42 |
| **Bi** | n.d. | n.d. | n.d. | n.d. | n.d. | n.d. | 0.14 | 0.017 | 0.026 | 0.13 | 0.0057 | 0.084 | 0.15 | 0.058 | 0.04 | 0.28 | 0.18 | 0.22 | 0.019 |
| **U** | n.d. | n.d. | n.d. | n.d. | n.d. | 0.95 | 0.133 | 0.278 | 0.0099 | 0.035 | n.d. | 0.041 | 0.128 | 0.0179 | 0.45 | 0.165 | 0.167 | 0.99 | n.d. |

Table B2: Detection limits for sulfides from LA-ICP-MS with 99% confidence. All concentrations are given in ppm

| Sample mineral | 20ALS4F Po-1 | 20ALS4F Po-2 | 20ALS4F Po-3 | 20ALS4F Cpy-4 | 20ALS4F Cpy-5 | 20ALS4F Cpy-6 | 20ALS4F Po-7 | 20ALS4F Po-8 | 20ALS4F Po-9 | 20ALS4F CPY-10 | 20ALS4F CPY-11 | 20ALS4F CPY-12 | 20ALS4F Py-13 | 20ALS4F Py-14 | 20ALS4F Py-15 | 20ALS4F Py-16 |
|---|---|---|---|---|---|---|---|---|---|---|---|---|---|---|---|---|
| **Si** | 9.72 | 9.52 | 10.23 | 10.69 | 8.31 | 8.23 | 12.64 | 11.16 | 12.43 | 10.19 | 10.78 | 11.13 | 5.18 | 5.27 | 4.74 | 4.22 |
| **S** | 31.29 | 30.26 | 31.41 | 32.4 | 25.2 | 25.17 | 38.48 | 34.17 | 37.79 | 30.8 | 32.76 | 33.81 | 15.96 | 16.53 | 14.99 | 13.4 |
| **Ti** | 0.0681 | 0.0758 | 0.0623 | 0.0807 | 0.083 | 0.0678 | 0.105 | 0.0779 | 0.123 | 0.0735 | 0.0639 | 0.0847 | 0.0623 | 0.053 | 0.0409 | 0.0515 |
| **V** | 0.00553 | 0.00397 | 0.00705 | 0.00764 | 0.00398 | 0.00579 | 0.00756 | 0.00631 | 0.00737 | 0.00419 | 0.00736 | 0.00709 | 0.00338 | 0.00246 | 0.00291 | 0.00296 |
| **Cr** | 0.195 | 0.193 | 0.204 | 0.21 | 0.165 | 0.164 | 0.253 | 0.225 | 0.252 | 0.203 | 0.215 | 0.222 | 0.104 | 0.107 | 0.0978 | 0.0868 |
| **Mn** | 0.0352 | 0.0343 | 0.0367 | 0.037 | 0.0287 | 0.0282 | 0.045 | 0.0396 | 0.0446 | 0.0374 | 0.0374 | 0.0397 | 0.0179 | 0.0189 | 0.0178 | 0.0155 |
| **Fe** | 1.62 | 1.58 | 1.62 | 1.74 | 1.3 | 1.31 | 2.05 | 1.81 | 2 | 1.62 | 1.72 | 1.78 | 0.852 | 0.86 | 0.811 | 0.734 |
| **Co** | 0.00826 | 0.00813 | 0.00732 | 0.00883 | 0.00686 | 0.00744 | 0.00914 | 0.00986 | 0.0112 | 0.00974 | 0.00851 | 0.00818 | 0.00428 | 0.00335 | 0.00361 | 0.00297 |
| **Ni** | 0.439 | 0.419 | 0.505 | 0.488 | 0.387 | 0.39 | 0.589 | 0.532 | 0.584 | 0.452 | 0.459 | 0.496 | 0.238 | 0.277 | 0.249 | 0.211 |
| **Cu** | 0.0558 | 0.0534 | 0.0536 | 0.0515 | 0.0544 | 0.0665 | 0.115 | 0.0937 | 0.102 | 0.077 | 0.0915 | 0.106 | 0.0543 | 0.0492 | 0.0432 | 0.039 |
| **Zn** | 0.175 | 0.176 | 0.122 | 0.2 | 0.148 | 0.144 | 0.229 | 0.253 | 0.223 | 0.177 | 0.217 | 0.211 | 0.0918 | 0.0896 | 0.0678 | 0.0969 |
| **Ga** | 0.0041 | 0.00389 | 0.00405 | 0.00451 | 0.00373 | 0.00361 | 0.00531 | 0.00428 | 0.00563 | 0.0044 | 0.00421 | 0.00486 | 0.00208 | 0.00232 | 0.00209 | 0.00189 |
| **Ge** | 0.0924 | 0.114 | 0.11 | 0.126 | 0.0886 | 0.0961 | 0.142 | 0.143 | 0.137 | 0.123 | 0.0989 | 0.123 | 0.0572 | 0.0694 | 0.0716 | 0.0582 |
| **As** | 0.0849 | 0.0804 | 0.0859 | 0.0928 | 0.0699 | 0.0703 | 0.111 | 0.0963 | 0.106 | 0.0858 | 0.0938 | 0.0969 | 0.0454 | 0.0453 | 0.043 | 0.0369 |
| **Se** | 0.938 | 0.935 | 0.989 | 1.02 | 0.803 | 0.797 | 1.23 | 1.11 | 1.24 | 0.998 | 1.06 | 1.1 | 0.512 | 0.53 | 0.479 | 0.431 |
| **Nb** | 0.00194 | 0.00111 | n.d. | 0.00171 | n.d. | 0.00189 | 0.00326 | 0.00368 | n.d. | 0.00233 | n.d. | n.d. | n.d. | 0.00109 | 0.00161 | n.d. |
| **Mo** | n.d. | 0.0147 | n.d. | n.d. | n.d. | 0.0126 | 0.0194 | n.d. | n.d. | n.d. | n.d. | n.d. | n.d. | n.d. | 0.00763 | n.d. |
| **Ru** | n.d. | n.d. | n.d. | 0.013 | n.d. | n.d. | n.d. | n.d. | n.d. | n.d. | n.d. | 0.0113 | n.d. | 0.00392 | n.d. | n.d. |
| **Rh** | n.d. | n.d. | 0.00229 | 0.00137 | 0.00185 | 0.00107 | n.d. | n.d. | 0.00259 | 0.00186 | 0.00171 | 0.00103 | 0.00083 | n.d. | 0.00046 | 0.00071 |
| **Ag** | 0.00381 | 0.00293 | n.d. | 0.00321 | 0.00205 | 0.00251 | 0.00315 | 0.00399 | 0.00314 | 0.004 | 0.00269 | 0.00278 | n.d. | 0.00273 | n.d. | 0.0021 |
| **Pd** | 0.00748 | 0.00605 | n.d. | n.d. | 0.00631 | 0.00363 | 0.00789 | 0.00704 | 0.00554 | n.d. | n.d. | 0.00689 | n.d. | n.d. | 0.00305 | 0.00435 |
| **Cd** | n.d. | 0.0121 | 0.00906 | 0.0162 | n.d. | 0.0126 | 0.0251 | 0.0201 | 0.0223 | 0.0201 | n.d. | 0.0139 | 0.00651 | n.d. | 0.00758 | 0.00558 |
| **In** | n.d. | n.d. | 0.00098 | 0.00144 | n.d. | n.d. | n.d. | 0.00155 | n.d. | n.d. | 0.00105 | n.d. | n.d. | n.d. | 0.00048 | n.d. |
| **Sn** | 0.0295 | 0.0314 | 0.0306 | 0.031 | 0.0258 | 0.0246 | 0.0357 | 0.0354 | 0.0386 | 0.0297 | 0.0293 | 0.029 | 0.0166 | 0.0158 | 0.0134 | 0.0134 |
| **Sb** | n.d. | n.d. | n.d. | n.d. | n.d. | 0.00188 | n.d. | n.d. | n.d. | n.d. | n.d. | 0.00367 | n.d. | n.d. | n.d. | n.d. |
| **Te** | 0.0284 | 0.0197 | 0.0323 | 0.0306 | 0.0247 | 0.0271 | 0.0312 | 0.0233 | 0.0394 | 0.0295 | 0.0289 | 0.0335 | 0.0148 | 0.0156 | 0.0143 | 0.00982 |
| **Ba** | 0.00285 | 0.00694 | n.d. | 0.00819 | 0.00595 | 0.00593 | 0.00913 | 0.00471 | 0.00983 | 0.00732 | 0.00952 | 0.00465 | 0.00376 | 0.00425 | 0.00207 | 0.00295 |
| **W** | n.d. | n.d. | n.d. | n.d. | n.d. | n.d. | n.d. | n.d. | n.d. | n.d. | n.d. | n.d. | n.d. | n.d. | n.d. | n.d. |
| **Re** | n.d. | n.d. | n.d. | n.d. | n.d. | n.d. | n.d. | n.d. | n.d. | n.d. | n.d. | n.d. | n.d. | n.d. | n.d. | n.d. |
| **Os** | n.d. | n.d. | n.d. | n.d. | n.d. | n.d. | n.d. | n.d. | n.d. | n.d. | n.d. | n.d. | n.d. | n.d. | n.d. | n.d. |
| **Ir** | n.d. | n.d. | n.d. | n.d. | n.d. | n.d. | n.d. | n.d. | n.d. | n.d. | n.d. | n.d. | n.d. | n.d. | n.d. | n.d. |
| **Pt** | n.d. | n.d. | n.d. | n.d. | n.d. | n.d. | n.d. | n.d. | n.d. | n.d. | n.d. | n.d. | n.d. | n.d. | n.d. | n.d. |
| **Au** | n.d. | n.d. | n.d. | n.d. | n.d. | n.d. | n.d. | n.d. | n.d. | n.d. | n.d. | n.d. | n.d. | n.d. | n.d. | n.d. |
| **Hg** | 0.0837 | 0.0836 | 0.0777 | 0.0862 | 0.0658 | 0.0624 | 0.0921 | 0.0883 | 0.0846 | 0.0756 | 0.0798 | 0.0818 | 0.0385 | 0.0337 | 0.0359 | 0.0344 |
| **Tl** | 0.00136 | 0.00165 | n.d. | 0.00104 | n.d. | n.d. | 0.00177 | 0.00112 | 0.00176 | n.d. | n.d. | n.d. | n.d. | 0.00076 | 0.0012 | n.d. |
| **Pb** | n.d. | n.d. | n.d. | n.d. | n.d. | n.d. | n.d. | n.d. | n.d. | n.d. | n.d. | n.d. | n.d. | n.d. | n.d. | n.d. |
| **Bi** | n.d. | n.d. | n.d. | n.d. | n.d. | n.d. | n.d. | n.d. | n.d. | 0.00074 | n.d. | n.d. | n.d. | n.d. | n.d. | n.d. |
| **U** | n.d. | n.d. | n.d. | n.d. | n.d. | n.d. | n.d. | n.d. | n.d. | n.d. | n.d. | n.d. | n.d. | n.d. | n.d. | n.d. |

Table B2: Continued

| Sample mineral | 20ALS3S1 Po-10 | 20ALS31 Po-11 | 20ALS3S1 Po-12 | 20ALS3S1 Cpy-13 | 20ALS3S1 Cpy-14 | 20ALS3S1 Cpy-15 | 20ALS31 Po-16 | 20ALS3S1 Po-17 | 20ALS3S1 Po-18 | 20ALS3S1 Po-19 | 20ALS3S1 Po-20 | 20ALS3S1 Po-21 | 20ALS3S1 Po-22 | 20ALS3S1 Po-23 | 20ALS3S1 Po-24 | 20ALS3S1 Cpy-25 |
|---|---|---|---|---|---|---|---|---|---|---|---|---|---|---|---|---|
| **Si** | 9.79 | 9.45 | 11.04 | 10.03 | 8.78 | 9.3 | 6.57 | 6.66 | 5.79 | 12.57 | 10.81 | 10.08 | 8.9 | 13.47 | 11.25 | 9.86 |
| **S** | 33.21 | 31.2 | 35.39 | 31.51 | 27.41 | 28.98 | 20.55 | 21.43 | 18.52 | 39.35 | 33.57 | 31.37 | 27.74 | 42.96 | 35.68 | 31.07 |
| **Ti** | 0.05 | 0.111 | 0.0561 | 0.0842 | 0.0971 | 0.0786 | 0.0652 | 0.0923 | 0.0789 | 0.164 | 0.163 | 0.118 | 0.0548 | 0.153 | 0.151 | 0.108 |
| **V** | 0.00498 | 0.0077 | 0.00641 | 0.0069 | 0.00627 | 0.00504 | 0.00474 | 0.00393 | 0.00407 | 0.00945 | 0.00723 | 0.00524 | 0.00495 | 0.0104 | 0.0077 | 0.00636 |
| **Cr** | 0.199 | 0.194 | 0.222 | 0.2 | 0.177 | 0.188 | 0.133 | 0.138 | 0.12 | 0.252 | 0.216 | 0.202 | 0.178 | 0.273 | 0.235 | 0.202 |
| **Mn** | 0.0385 | 0.0364 | 0.0423 | 0.0364 | 0.0328 | 0.0328 | 0.0233 | 0.0242 | 0.0217 | 0.0457 | 0.0388 | 0.0358 | 0.034 | 0.0502 | 0.0426 | 0.0364 |
| **Fe** | 1.71 | 1.66 | 1.92 | 1.68 | 1.51 | 1.59 | 1.11 | 1.2 | 0.986 | 2.11 | 1.86 | 1.7 | 1.53 | 2.3 | 1.94 | 1.68 |
| **Co** | 0.00723 | 0.00684 | 0.00848 | 0.00865 | 0.00844 | 0.00845 | 0.00513 | 0.00462 | 0.00355 | 0.0109 | 0.0078 | 0.00873 | 0.00526 | 0.0105 | 0.00958 | 0.00917 |
| **Ni** | 0.495 | 0.456 | 0.508 | 0.492 | 0.437 | 0.46 | 0.355 | 0.356 | 0.301 | 0.722 | 0.579 | 0.543 | 0.483 | 0.745 | 0.664 | 0.524 |
| **Cu** | 0.0779 | 0.0761 | 0.0869 | 0.0785 | 0.0776 | 0.0944 | 0.0738 | 0.0711 | 0.0601 | 0.112 | 0.0989 | 0.0925 | 0.078 | 0.13 | 0.105 | 0.0901 |
| **Zn** | 0.199 | 0.198 | 0.207 | 0.195 | 0.139 | 0.184 | 0.15 | 0.158 | 0.123 | 0.241 | 0.191 | 0.149 | 0.164 | 0.306 | 0.252 | 0.231 |
| **Ga** | 0.00429 | 0.00438 | 0.00445 | 0.00396 | 0.00418 | 0.00446 | 0.0032 | 0.00304 | 0.00294 | 0.00645 | 0.00468 | 0.00439 | 0.00465 | 0.00698 | 0.00501 | 0.00445 |
| **Ge** | 0.133 | 0.126 | 0.153 | 0.12 | 0.109 | 0.134 | 0.0972 | 0.0975 | 0.0959 | 0.191 | 0.151 | 0.143 | 0.14 | 0.208 | 0.166 | 0.143 |
| **As** | 0.0873 | 0.0829 | 0.0952 | 0.0917 | 0.0752 | 0.0814 | 0.0587 | 0.0607 | 0.0504 | 0.111 | 0.0942 | 0.0874 | 0.0761 | 0.117 | 0.0953 | 0.0874 |
| **Se** | 0.994 | 0.971 | 1.1 | 0.99 | 0.878 | 0.942 | 0.67 | 0.696 | 0.606 | 1.25 | 1.09 | 1.03 | 0.919 | 1.42 | 1.19 | 1.02 |
| **Nb** | 0.00334 | n.d. | 0.00416 | 0.00166 | n.d. | 0.00154 | n.d. | n.d. | n.d. | 0.00257 | n.d. | 0.0017 | n.d. | 0.00336 | n.d. | n.d. |
| **Mo** | n.d. | n.d. | n.d. | n.d. | 0.0139 | 0.0147 | 0.0107 | 0.00789 | n.d. | 0.02 | 0.0215 | n.d. | 0.0187 | n.d. | 0.027 | n.d. |
| **Ru** | n.d. | 0.0102 | 0.0203 | n.d. | 0.00921 | n.d. | n.d. | 0.0074 | 0.00632 | 0.0133 | n.d. | 0.0108 | 0.0102 | 0.0107 | 0.00897 | n.d. |
| **Rh** | 0.00134 | 0.0013 | n.d. | 0.00133 | 0.00144 | 0.00231 | 0.0011 | 0.00149 | 0.0015 | 0.00267 | 0.00295 | 0.00096 | n.d. | 0.00357 | 0.00376 | 0.00169 |
| **Ag** | n.d. | 0.00638 | 0.00406 | 0.00481 | 0.00505 | n.d. | 0.00275 | 0.00256 | 0.00394 | 0.00325 | 0.00493 | 0.00493 | 0.0043 | 0.00522 | 0.00789 | 0.00462 |
| **Pd** | n.d. | 0.00859 | 0.011 | 0.00621 | 0.00861 | 0.0122 | 0.00781 | 0.00614 | 0.00453 | 0.0123 | 0.0107 | 0.014 | n.d. | n.d. | 0.0146 | 0.0077 |
| **Cd** | 0.0181 | 0.0196 | 0.0246 | n.d. | 0.0111 | 0.0117 | n.d. | n.d. | 0.00759 | 0.0226 | 0.0139 | 0.0129 | 0.0149 | n.d. | 0.0151 | 0.0159 |
| **In** | n.d. | n.d. | n.d. | 0.00159 | n.d. | 0.00148 | n.d. | 0.0005 | n.d. | 0.00181 | 0.00112 | n.d. | n.d. | 0.00229 | n.d. | n.d. |
| **Sn** | 0.0277 | 0.0267 | 0.0368 | 0.0309 | 0.0273 | 0.0256 | 0.0185 | 0.0176 | 0.0163 | 0.0415 | 0.0295 | 0.0303 | 0.0271 | 0.0398 | 0.0359 | 0.0322 |
| **Sb** | n.d. | n.d. | 0.0039 | n.d. | 0.00307 | n.d. | n.d. | 0.00249 | n.d. | n.d. | n.d. | n.d. | n.d. | n.d. | n.d. | n.d. |
| **Te** | 0.0334 | 0.0301 | 0.0252 | 0.034 | 0.0285 | 0.0304 | 0.0205 | 0.0204 | 0.0195 | 0.028 | 0.0268 | 0.0256 | 0.0267 | 0.0375 | 0.0395 | 0.0304 |
| **Ba** | 0.00858 | 0.00589 | 0.00956 | 0.00907 | 0.00702 | 0.00741 | 0.00646 | n.d. | 0.00406 | 0.0108 | 0.012 | 0.00817 | 0.00412 | 0.0137 | 0.0096 | 0.00698 |
| **W** | n.d. | n.d. | n.d. | n.d. | n.d. | n.d. | n.d. | n.d. | n.d. | n.d. | n.d. | n.d. | n.d. | n.d. | n.d. | n.d. |
| **Re** | n.d. | n.d. | n.d. | n.d. | n.d. | n.d. | n.d. | n.d. | n.d. | n.d. | n.d. | n.d. | n.d. | n.d. | n.d. | n.d. |
| **Os** | n.d. | n.d. | n.d. | n.d. | n.d. | n.d. | n.d. | n.d. | n.d. | n.d. | n.d. | n.d. | n.d. | n.d. | n.d. | n.d. |
| **Ir** | n.d. | n.d. | n.d. | n.d. | n.d. | n.d. | n.d. | n.d. | n.d. | n.d. | n.d. | n.d. | n.d. | n.d. | n.d. | n.d. |
| **Pt** | n.d. | n.d. | n.d. | n.d. | n.d. | n.d. | n.d. | n.d. | n.d. | n.d. | n.d. | n.d. | n.d. | n.d. | n.d. | n.d. |
| **Au** | n.d. | n.d. | n.d. | n.d. | n.d. | n.d. | n.d. | n.d. | n.d. | n.d. | n.d. | n.d. | n.d. | n.d. | n.d. | n.d. |
| **Hg** | 0.0808 | 0.0681 | 0.0716 | 0.0742 | 0.062 | 0.0688 | 0.0525 | 0.0481 | 0.0409 | 0.0779 | 0.0763 | 0.0694 | 0.0625 | 0.0986 | 0.0675 | 0.0726 |
| **Tl** | n.d. | n.d. | n.d. | n.d. | 0.00154 | n.d. | n.d. | n.d. | n.d. | n.d. | n.d. | 0.00146 | n.d. | n.d. | n.d. | n.d. |
| **Pb** | n.d. | 0.00186 | n.d. | 0.00191 | n.d. | n.d. | n.d. | n.d. | n.d. | n.d. | n.d. | n.d. | n.d. | n.d. | n.d. | 0.00243 |
| **Bi** | 0.00185 | 0.00085 | 0.00182 | 0.00087 | 0.00054 | n.d. | n.d. | n.d. | n.d. | 0.00157 | n.d. | n.d. | n.d. | n.d. | n.d. | n.d. |
| | n.d. | n.d. | n.d. | n.d. | n.d. | n.d. | n.d. | n.d. | n.d. | n.d. | n.d. | n.d. | n.d. | n.d. | n.d. | n.d. |

Table B2: Continued

| Sample mineral | 20ALS3S1 Cpy-26 | 20ALS3S1 Cpy-27 | 20ALS3S1 Py-28 | 20ALS3S1 Py-29 | 20ALS3S1 Py-30 | 20ALS3S1 Cpy-26 | 19LITE3 Py-1 | 19LITE3 Py-2 | 19LITE3 Py-3 | 19LITE3 Py-4 | 19LITE3 Py-5 | 19LITE3 Py-6 | 19LITE3 Py-7 | 19LITE3 Py-8 | 19LITE3 Py-9 | 19LITE3 Py-10 | 19LITE3 Py-11 | 19LITE3 Py-12 | 19LITE3 Po-13 |
|---|---|---|---|---|---|---|---|---|---|---|---|---|---|---|---|---|---|---|---|
| **Si** | 10.05 | 12.17 | 5.31 | 5.41 | 5.57 | 5.41 | 5.07 | 4.11 | 4.61 | 4.35 | 4.14 | 3.47 | 4.71 | 4.65 | 6.17 | 3.24 | 6.32 | 10.46 | 10.05 |
| **S** | 30.88 | 37.8 | 16.41 | 16.99 | 17.69 | 18.15 | 17.55 | 14.3 | 15.9 | 14.76 | 14.3 | 12.09 | 16.47 | 15.84 | 20.75 | 11.43 | 22.86 | 37.96 | 30.88 |
| **Ti** | 0.131 | 0.122 | 0.0516 | 0.0753 | 0.0951 | 0.0568 | 0.0652 | 0.0247 | 0.0705 | 0.0739 | 0.0612 | 0.055 | 0.0758 | 0.074 | 0.08 | 0.0496 | 0.0797 | 0.143 | 0.131 |
| **V** | 0.00716 | 0.00799 | 0.00356 | 0.00359 | 0.00336 | 0.00296 | 0.00325 | 0.00236 | 0.00295 | 0.00285 | 0.00234 | 0.00256 | 0.00334 | 0.00358 | 0.00305 | 0.0025 | 0.00519 | 0.00732 | 0.00716 |
| **Cr** | 0.201 | 0.243 | 0.106 | 0.108 | 0.113 | 0.114 | 0.105 | 0.086 | 0.0967 | 0.0912 | 0.089 | 0.0738 | 0.0992 | 0.097 | 0.129 | 0.0677 | 0.133 | 0.222 | 0.201 |
| **Mn** | 0.0352 | 0.0431 | 0.0194 | 0.0192 | 0.0201 | 0.0221 | 0.02 | 0.0167 | 0.0183 | 0.0175 | 0.0167 | 0.0134 | 0.0193 | 0.0189 | 0.0239 | 0.0129 | 0.0245 | 0.043 | 0.0352 |
| **Fe** | 1.73 | 2.07 | 0.924 | 0.98 | 0.999 | 0.974 | 0.991 | 0.778 | 0.864 | 0.827 | 0.818 | 0.668 | 0.945 | 0.912 | 1.17 | 0.63 | 1.2 | 2.06 | 1.73 |
| **Co** | 0.00818 | 0.00901 | 0.0052 | 0.00458 | 0.00511 | 0.00428 | 0.00461 | 0.00327 | 0.00404 | 0.00305 | 0.00241 | 0.0024 | 0.003 | 0.00306 | 0.00292 | 0.00191 | 0.00337 | 0.00569 | 0.00818 |
| **Ni** | 0.511 | 0.578 | 0.28 | 0.308 | 0.315 | 0.325 | 0.298 | 0.252 | 0.308 | 0.309 | 0.292 | 0.247 | 0.321 | 0.306 | 0.429 | 0.22 | 0.439 | 0.653 | 0.511 |
| **Cu** | 0.104 | 0.136 | 0.0629 | 0.0619 | 0.0605 | 0.0561 | 0.0502 | 0.0417 | 0.0485 | 0.0437 | 0.0427 | 0.0348 | 0.0484 | 0.0438 | 0.0582 | 0.0281 | 0.0577 | 0.0996 | 0.104 |
| **Zn** | 0.192 | 0.261 | 0.0892 | 0.103 | 0.104 | 0.119 | 0.0699 | 0.0867 | 0.0951 | 0.0965 | 0.0705 | 0.0693 | 0.0939 | 0.0948 | 0.13 | 0.0621 | 0.161 | 0.268 | 0.192 |
| **Ga** | 0.00461 | 0.00548 | 0.00265 | 0.00275 | 0.00263 | 0.00264 | 0.0028 | 0.00258 | 0.00253 | 0.00241 | 0.00247 | 0.00186 | 0.00288 | 0.00278 | 0.0037 | 0.00179 | 0.00404 | 0.00629 | 0.00461 |
| **Ge** | 0.172 | 0.19 | 0.0743 | 0.0856 | 0.092 | 0.0899 | 0.0884 | 0.0753 | 0.0813 | 0.0949 | 0.0814 | 0.0762 | 0.101 | 0.096 | 0.117 | 0.067 | 0.131 | 0.248 | 0.172 |
| **As** | 0.0877 | 0.103 | 0.045 | 0.0465 | 0.0499 | 0.0514 | 0.0497 | 0.0427 | 0.0463 | 0.0438 | 0.0423 | 0.0348 | 0.0475 | 0.0456 | 0.0596 | 0.0323 | 0.0616 | 0.108 | 0.0877 |
| **Se** | 1.01 | 1.24 | 0.547 | 0.557 | 0.584 | 0.588 | 0.538 | 0.447 | 0.509 | 0.482 | 0.461 | 0.392 | 0.527 | 0.506 | 0.678 | 0.36 | 0.704 | 1.19 | 1.01 |
| **Nb** | 0.00166 | 0.00405 | n.d. | n.d. | 0.00122 | 0.00116 | 0.00089 | 0.00116 | n.d. | 0.00146 | 0.0011 | 0.00066 | 0.00107 | 0.00178 | 0.00226 | 0.00059 | n.d. | 0.0025 | 0.00166 |
| **Mo** | 0.0159 | n.d. | 0.0106 | n.d. | n.d. | 0.0092 | 0.0122 | 0.00711 | n.d. | n.d. | n.d. | 0.0111 | 0.0104 | 0.00997 | 0.0155 | 0.01 | 0.0162 | 0.0244 | 0.0159 |
| **Ru** | n.d. | 0.0129 | n.d. | 0.00594 | n.d. | 0.0107 | 0.00705 | n.d. | 0.00758 | 0.00507 | 0.00711 | n.d. | 0.0106 | n.d. | 0.00521 | 0.0106 | 0.0153 | 0.0134 | n.d. |
| **Rh** | 0.00328 | n.d. | 0.00073 | 0.00106 | 0.0008 | 0.00163 | 0.00125 | 0.00145 | 0.0015 | 0.00148 | n.d. | 0.00075 | 0.00174 | 0.00173 | 0.00234 | 0.00132 | 0.00252 | 0.00371 | 0.00328 |
| **Ag** | 0.00659 | 0.0059 | n.d. | 0.00307 | 0.0049 | 0.00105 | 0.00296 | 0.00336 | 0.00205 | 0.00274 | 0.00286 | 0.00146 | 0.00292 | 0.00336 | 0.00333 | 0.00187 | 0.00454 | 0.00604 | 0.00659 |
| **Pd** | 0.0143 | 0.0117 | 0.00617 | 0.00586 | 0.00513 | 0.00642 | 0.0032 | 0.00813 | 0.00514 | 0.00594 | 0.0048 | 0.00576 | 0.00662 | 0.00559 | 0.009 | 0.00335 | 0.0114 | n.d. | 0.0143 |
| **Cd** | 0.0199 | 0.0153 | 0.00836 | 0.014 | 0.0106 | 0.0203 | 0.0116 | 0.011 | 0.00982 | 0.0144 | 0.0109 | 0.00987 | 0.0123 | 0.00628 | 0.0134 | 0.00995 | 0.0232 | 0.0324 | 0.0199 |
| **In** | n.d. | 0.00176 | 0.00068 | n.d. | n.d. | 0.00144 | 0.00123 | 0.00056 | 0.00063 | 0.00091 | n.d. | 0.0005 | n.d. | 0.00148 | 0.00112 | 0.00074 | 0.0009 | n.d. | n.d. |
| **Sn** | 0.0314 | 0.039 | 0.015 | 0.0158 | 0.017 | 0.0163 | 0.0162 | 0.0134 | 0.0161 | 0.0136 | 0.013 | 0.0117 | 0.0138 | 0.0153 | 0.0197 | 0.0098 | 0.0214 | 0.0357 | 0.0314 |
| **Sb** | n.d. | n.d. | 0.00198 | n.d. | n.d. | n.d. | n.d. | n.d. | n.d. | 0.0018 | n.d. | n.d. | n.d. | n.d. | n.d. | n.d. | n.d. | n.d. | n.d. |
| **Te** | 0.0333 | 0.0297 | 0.0158 | 0.0127 | 0.0164 | 0.0186 | 0.015 | 0.0145 | 0.0139 | 0.0105 | 0.014 | 0.0111 | 0.0167 | 0.0122 | 0.0193 | 0.0109 | 0.0196 | 0.0318 | 0.0333 |
| **Ba** | 0.0121 | 0.0128 | 0.00615 | 0.00507 | 0.00257 | 0.00674 | 0.0023 | 0.00403 | 0.00303 | 0.00495 | 0.00512 | 0.0017 | 0.00424 | 0.0046 | 0.00622 | 0.00288 | 0.00746 | 0.00531 | 0.0121 |
| **W** | n.d. | n.d. | n.d. | n.d. | n.d. | n.d. | n.d. | n.d. | n.d. | n.d. | n.d. | n.d. | n.d. | n.d. | n.d. | n.d. | n.d. | n.d. | n.d. |
| **Re** | n.d. | n.d. | n.d. | n.d. | n.d. | n.d. | n.d. | n.d. | n.d. | n.d. | n.d. | n.d. | n.d. | 0.00079 | n.d. | n.d. | n.d. | n.d. | n.d. |
| **Os** | n.d. | n.d. | n.d. | n.d. | n.d. | n.d. | n.d. | n.d. | n.d. | n.d. | n.d. | n.d. | n.d. | n.d. | n.d. | n.d. | n.d. | n.d. | n.d. |
| **Ir** | n.d. | n.d. | n.d. | n.d. | n.d. | n.d. | n.d. | n.d. | n.d. | n.d. | n.d. | n.d. | n.d. | n.d. | n.d. | n.d. | n.d. | n.d. | n.d. |
| **Pt** | n.d. | n.d. | n.d. | n.d. | n.d. | n.d. | n.d. | n.d. | n.d. | n.d. | n.d. | n.d. | n.d. | n.d. | n.d. | n.d. | n.d. | n.d. | n.d. |
| **Au** | n.d. | n.d. | n.d. | n.d. | n.d. | n.d. | n.d. | n.d. | n.d. | n.d. | n.d. | n.d. | n.d. | n.d. | n.d. | n.d. | n.d. | n.d. | n.d. |
| **Hg** | 0.073 | 0.0893 | 0.0399 | 0.0355 | 0.04 | 0.055 | 0.0481 | 0.0372 | 0.0369 | 0.0353 | 0.0347 | 0.0216 | 0.0418 | 0.0423 | 0.0524 | 0.0293 | 0.0591 | 0.106 | 0.073 |
| **Tl** | 0.00143 | n.d. | n.d. | n.d. | 0.0006 | n.d. | n.d. | n.d. | n.d. | 0.00095 | 0.00047 | 0.00056 | n.d. | n.d. | n.d. | n.d. | n.d. | n.d. | 0.00143 |
| **Pb** | n.d. | n.d. | n.d. | n.d. | 0.00142 | n.d. | n.d. | n.d. | n.d. | n.d. | n.d. | n.d. | n.d. | n.d. | n.d. | n.d. | n.d. | n.d. | n.d. |
| **Bi** | n.d. | n.d. | n.d. | n.d. | n.d. | 0.00177 | 0.00109 | 0.00081 | 0.00065 | 0.00061 | n.d. | 0.00037 | 0.00069 | 0.00047 | n.d. | n.d. | 0.00047 | n.d. | n.d. |
| **U** | n.d. | n.d. | n.d. | n.d. | n.d. | n.d. | n.d. | n.d. | n.d. | n.d. | n.d. | n.d. | n.d. | n.d. | n.d. | n.d. | n.d. | n.d. | n.d. |